Development of a mobile positron trap for future space applications

Master Thesis

Paul Prantl

Supervisors: Prof. Dr. Paolo Crivelli

Lars Gerchow

August 20th 2020

Abstract

Antimatter particles are a possible future fuel for interplanetary space travel due to its outstanding energy to mass ratio of $9 \times 10^{10}\,\mathrm{MJ\,kg^{-1}}$ up to nine magnitudes higher than currently used fuels.
This thesis aims at designing, building, and testing a mobile miniaturized Penning-Malmberg trap to store positrons for 12 h. The magnetic field is generated by permanent magnets, while the electric potential is generated using foil electrodes. Additionally, the experiment is designed to fit inside a 4U CubeSat form factor and withstand forces during flight of a sounding rocket. Such rockets are developed by ARIS, a student association enabling hands-on experience within an interdisciplinary project team.
Positrons storing for 3 µs is achieved. The time is limited by the employed measurement hardware. Even though the mobility of the trap could not be tested the project was a success storing positrons for the first time using permanent magnets and foil electrodes.

Contents

List of Figures

List of Tables

Abbreviations

AGL	Above Ground Level
AL	Aluminum
ARIS	Akademische Raumfahrt Initiative Schweiz
BNC	Bayonet Neil Concelman
CAD	Computer Aided Design
CAE	Computer Aided Engineering
CF	ConFlat flange
COTS	Commercial off the shelf
CU	Copper
EuRoC	European Rocket Competition
FDM	Fused Depositon Modeling
FEM	Finite Element Method
FKM	Fluoroelastomer
FT	Feedthrough
GND	Ground (electrical reference potential)
HV	High Vacuum
KF	Klein flange
LV	Low Vacuum
MCP	Microchannel Plate
MRI	Magnetic Resonance Imaging
MV	Medium Vacuum
NEG	None-Evaporative Getter
NMR	Nuclear Magnetic Resonance Spectroscopy
OFHC	Oxygen Free High purity Copper
PCB	Printed Circuit Board
PEEK	Polyetheretherketon

PET Positron Emission Tomography
PMT Photomultiplier Tube
PTFE Polytetrafluorethylen

QCF Quick ConFlat flange

RF Radio Frequency
RGA Residual Gas Analyzer

SMD Surface-mounted Device
SPAC Spaceport America Cup
SRAD Student researched and developed
SS Stainless Steel
STL Stereolithographie

TTL Transistor–Transistor Logic

UHV Ultra-High Vacuum

VHV Very High Vacuum

XHV Extreme Ultra-High Vacuum

List of symbols

1 Introduction

Positrons are capable of releasing a tremendous amount of energy upon annihilation with an electron. Even though they have the same mass, the charge is exactly opposite. The energy released during annihilation is because the entire mass of the two particles is converted into energy according to Einstein's formula $E = 2 \cdot mc^2$. The energy produced is in the form of two photons at 511 keV. This energy poses a tremendous potential for future applications, from high energy lasers or future space propulsion systems.

Even though such applications are still in the far future, small steps advancing technology lead there. One of the first challenges to solve is enabling storage and transport of positrons in a trap. Without this, possible applications can and will not be developed.

1.1 Motivation

As mentioned previously, positron-electron annihilation yields the highest possible energy per mass ration available, as can be seen in Table 1.

Process	E/m [MJ kg^{-1}]	
e^+e^- annihilation	8.99×10^{10}	[**Hendee2005**]
Nuclear fusion	3.0×10^{8}	[**Mills2010**]
Nuclear fission	7.9×10^{7}	[**Edwards2008**]
Methane	50	[**fission**]

Table 1: Comparison of multiple energy densities

This shows the possibilities if the generated energy can be controlled. Especially if analyzing it with relation to space propulsion fuels like methane, the energy available can revolutionize space travel.

Positrons are up to this point of high interest in particle physics with countless experiments running to increase the understanding of the past, present, and future of our universe.

1.2 Thesis goals

The goal of this experiment is the development of a movable positron trap flying in a sounding rocket. First, the theory on trapping of positrons is analyzed, followed by component and structural analysis of the structure as well as the vacuum system. Subsequent calculations, simulations, and testing

assisted in selecting the best designs for trapping before performing actual trapping measurements. The focus is set on a functioning trap as the primary goal and secondary a movable trap. This is done in order to focus on one problem at a time and proceed in a step by step approach.

Since the trap is designed to be flying with a sounding rocket to an altitude of 30 000 ft with project EULER, the structural integrity during flight needs to be ensured. The sounding rocket is the third generation of launch vehicles developed by Akademische Raumfahrt Initiative Schweiz (ARIS), a student association competing at the world's largest student rocket competition Spaceport America Cup (SPAC).

1.3 Akademische Raumfahrt Initiative Schweiz - ARIS

The Akademische Raumfahrt Initiative Schweiz (ARIS) was founded in October 2017 enabling motivated students in Switzerland to apply their knowledge in a practical project. Thereby complex functioning systems are developed in an interdisciplinary team in order to have student-developed hardware flying in space by 2029.
Currently, the focus is on developing of sounding rockets, from structures over recovery systems to advances in rocket engines enabling knowledge base and procedures for future projects.
The mid-term goal is the annual Spaceport America Cup (SPAC), the worlds largest student-built sounding rocket competition with more than 150 participating teams and over 1500 students from all over the world. SPAC is an engineering competition, with the teams being graded on documentation and presentation of their work besides the flight of the rocket itself. The competition is divided into 2 groups, one of them flying to an altitude of 10 000 ft (3048 m) Above Ground Level (AGL) while the others to 30 000 ft (9144 m) AGL. In each of these two groups, there are three sub-categories:

- Commercial off the shelf (COTS) Solid propellant motors
- Student researched and developed (SRAD) Solid propellant motors
- Student researched and developed Hybrid & Liquid propellant motors

The teams get points in the following four different categories:

- Documentation - 260
- Engineering - 240

Figure 1: ARIS Vision

- Apogee accuracy - 350
- Recovery - 150

Additionally, there are 100 bonus points, 50 for the payload being within specified requirements as well as 50 for launching on the first day of the competition, 25 if it is the second day.

Sounding rocket projects

The first launch vehicle by ARIS designed was TELL competing in the 10 000 ft COTS category. The key feature of TELL was air brake system to control the apogee by an increase in drag using plates controlled by an algorithm.

SPAC, the exceptional engineering earned the team the ”Charles Hoult

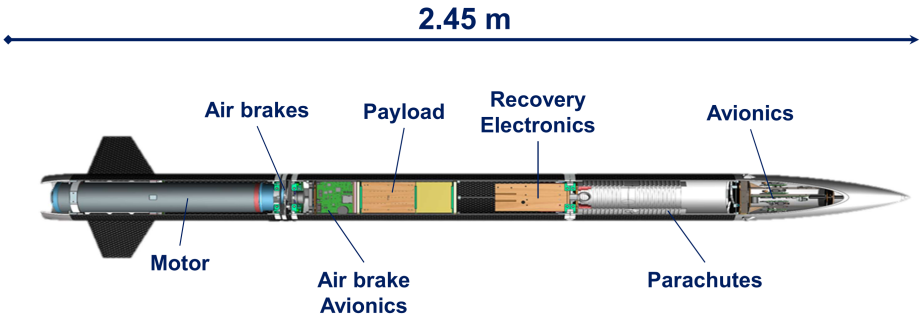

Figure 2: Overview of sounding rocket TELL

Award for modeling and simulation” for their innovative air brake design as

well as its control-algorithm "Chance-Constrained Optimal Altitude Control of a Rocket" [**TELL2018**].

The following project was an improved version called HEIDI. Due to a project cycle of experience and a focus on a solid preparation, the team was able to win second place in the 10 000 ft COTS category.

In parallel to sounding rocket project, ARIS was able to gather first experiences in designing hybrid rocket engines with project RHEA and the follow-up project IRIDE. First firing showed great possibilities of the technology and in 2021 the first rocket engine developed in-house will be lifting off.

1.4 Positron trap in a sounding rocket

Returning the focus to the task at hand, project EULER is briefly described as to understand the complexities involved to develop this payload.

Project EULER

Project EULER will be flying to 30 000 ft using a COTS engine. Sadly due to the pandemic in spring 2020, the SPAC was canceled in June. However, an alternative was established, allowing for a European rocketry competition in Portugal in the fall of 2020.

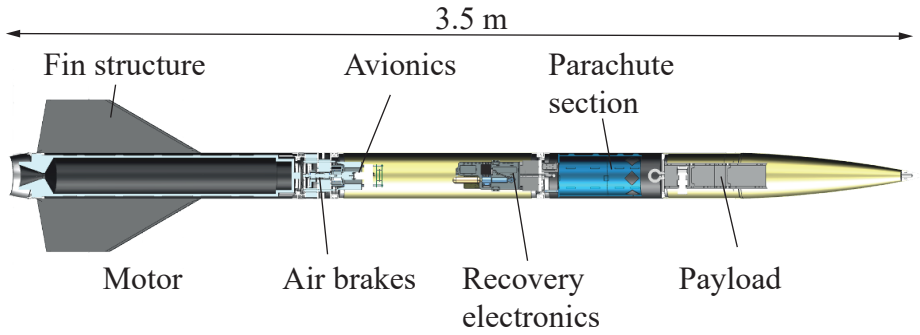

Figure 3: Overview of sounding rocket EULER subsystems

1.5 CubeSat standard

The CubeSat standard is commonly referred to as a cube with the size of 100 mm × 100 mm × 100 mm with a mass of 1.33 kg. This has been changed to 100 mm × 100 mm × 110 mm in size over the years and is now know as the 1U standard and there are lots of variations of this in the last years such as 1.5 U, 2U, 3U, and 6U systems. with slightly varying lengths as specified by the NASA's "CubeSat 101: Basic Concepts and Processes for First-Time CubeSat Developers "[**NASACubeSat**]. Further, there is not only the cube as a standard but also other geometries like e.g. CanSats.
During this thesis, certain concepts of this document are adopted to streamline the process and establish a workflow for future payload projects of ARIS. Further, this process allows for structured evaluation of the concept. Unfortunately, due to time constraints, a couple of steps suggested by the NASA process [**NASACubeSat**] need to be skipped to finish the project in time and fly the system with project EULER in 2020.

1.6 Requirements overview

To ensure the highest chances of mission success, a requirements document was created, with the most important requirement stated here and a complete overview in Appendix A:

REQ 1 The payload experiment shall fit inside a Volume of $100\,\text{mm} \times 100\,\text{mm} \times 400\,\text{mm}$

REQ 2 The payload mass shall be greater than 8.8 lb (3.992 kg)

REQ 3 The payload shall function independently of the launch vehicle

REQ 4 The payload shall not contain significant quantities of lead or any other hazardous materials

REQ 5 Radioactive material shall be concurred by competition officials and emit less than 1 µC

REQ 6 The payload components shall withstand accelerations during launch and main parachute deployment of 18 g

REQ 7 The payload shall withstand temperatures between $-50\,°\text{C}$ and $80\,°\text{C}$

REQ 8 The payload experiment shall use non magnetic materials

REQ 9 The battery life shall exceed 12 h under operating conditions

REQ 10 The electrodes shall contain the positrons axially with a voltage higher than 15 V

REQ 11 The magnetic field shall be higher than 6 mT (60 G)

REQ 12 The payload shall be fixed above the payload bulkhead using M5x15 screws at the corners of a square with 88 mm length

2 Trapping mechanisms for positron storage

In order to be able to investigate applications of e^+e^- annihilation, in a first step trapping of positrons needs to be resolved. This chapter will set the foundation of positron trapping and give a baseline of values that will be worked with. This will be followed by analysis of different traps and their storing abilities of particles, the mechanisms involved as well as their limitations before moving to practical traps and the challenges that come with the real world application. Concluding, different detection methods for positron annihilation will be analyzed.

2.1 Positron

Positrons e^+ are, as mentioned in Section 1, the antimatter particle to the electron e^-. They have the same mass and spin while having opposite charge [**Hughes1992**]. They are formed in the universe due to the high energy gamma rays interacting with atoms, yielding an electron and positron. This effect is called pair production [**Ferbel2003**]. This is one type of production, another is the use of naturally decaying radioactive materials. These need to be β^+ sources, whereby a proton decays into a neutron, a positron and a neutrino. This effect only occurs in certain materials such as ^{22}Na for the sources in a laboratory, or in potassium ^{40}K which is found e.g. in bananas.

Radioactive isotopes are used extensively in Positron Emission Tomography (PET), where a radioactive solution is injected into the body of a patient. The cells then process these materials and the emitted gamma rays can be detected by a PET scanner, allowing to image cancer cells [**Hendee2005**]. Furthermore, positrons are subject of current investigation in physics research.
The positron properties used in the following chapters in order to quantify and estimate characteristics of the trap are stated in Table 2.

2.2 Vacuum range estimation/Positron lifetime calculation

A vacuum estimation is conducted for to calculate the half-life of positrons at different vacuum levels. The results can be seen in Table 3. The expected time can be calculated using the formula for exponential decay

$$N_{e+}(t) = N_{e+}(0)e^{-\lambda_e t} \tag{2.2.1}$$

with the annihilation rate defined by Charlton [**Charlton2013**] as

Properties	Value
m_{e+}	$9.109 \times 10^{-31}\,\mathrm{kg}$
q_{e+}	$1.602 \times 10^{-19}\,\mathrm{C}$
$E_{e+,\parallel}$	$7.0\,\mathrm{eV}$
$E_{e+,\perp}$	$0.5\,\mathrm{eV}$
B_{trap}	$0.365\,\mathrm{T}$
U_{trap}	$10.8\,\mathrm{V}$
n_{e+}	10^3-10^5

Table 2: Positron values for boundary calculations

$$\lambda_e = \pi r_0^2 c n \cdot Z'_{\mathrm{eff}} \tag{2.2.2}$$

with r_0 the classical electron radius in m, c the speed of light in $\mathrm{m\,s^{-1}}$ and n the free number density in $[\mathrm{m^{-3}}]$. Z'_{eff} is the parameter indicating the available electrons to annihilate from Charlton [**Charlton2013**]. As a first estimate, the particle volume density n can be approximated using the ideal gas law $pV = Nk_{\mathrm{B}}T$ and reformulating it to Equation 2.2.3, with p being the pressure in Pa, $[k_{\mathrm{B}}]$ the Boltzmann constant in $[\mathrm{J\,K^{-1}}]$ and T the Temperature in [K]

$$n = \frac{N}{V} = \frac{p}{k_{\mathrm{B}}T} \tag{2.2.3}$$

and inserting it in 2.2.3 and using the average value of amount of molecules in 1 mol air gives the results in Table 3 and the plot of the annihilation rate in Figure 4.

Vacuum level [mbar]	**Half-life**
10^{-6}	2.5 min
10^{-7}	20.5 min
10^{-8}	3.4 h
10^{-9}	1.4 d
10^{-10}	2.0 w
10^{-11}	20.3 w

Table 3: Positron Half-life for different vacuum levels

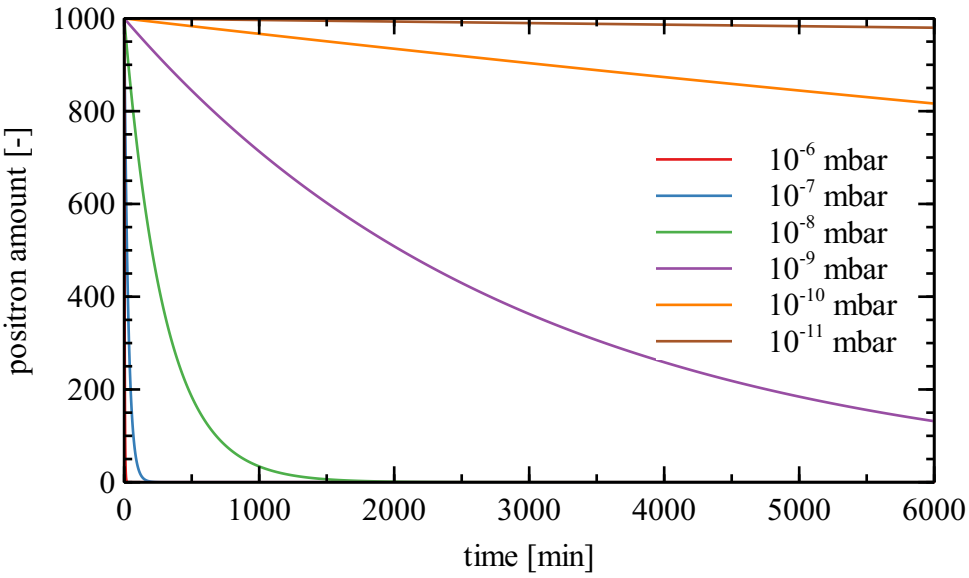

Figure 4: Annihilation rate for different vacuum levels

It can be concluded, that according to this estimation to store over a period of multiple days, a vacuum level of 10×10^{-10} mbar is necessary. For preliminary tests, a level of 10×10^{-6} mbar is sufficient in order to confirm the storage with the developed trap design.

2.3 Particle trapping

After the brief overview about the required vacuum level, the focus is now shifted to the theory and practical applications of trapping charged particles such as positrons. First, a general overview about the topic is given, before different traps are analyzed. This is followed by theory of motion of charged particles in traps before looking into disturbances due to imperfections. The section will be concluded by the analysis of relevant technologies and applications of similar traps.

In the following the term ”confinement” will be used, which is defined by Vogel as ”... (is) a stable configuration in which particles are localised in all three dimensions to a defined volume for long periods of time.” [**Vogel2018**]

This section will first introduce basic necessities, that any trap for charged particles needs to fulfil for confinement, before the two main types of traps, namely the ”Paul trap” named after Nobel Prize winner Wolfgang Paul and

the Penning trap named after Frans Michel Penning proposing this type of trap for charged particle confinement are explained.

2.3.1 Radial confinement

The first step is to radially confine a particle if it shall be trapped. This can be done in various ways, but always boils down to a correcting force acting on the particle and altering its trajectory in such a way that it begins to circle. Analogies can be drawn to a satellite orbiting the earth. Thereby the velocity and distance of the spacecraft is chosen such that it is orbiting the earth by balancing the forces acting due to gravity and impulse of the vehicle. For a particle in a trap, there is its own energy as well as the correction force keeping it contained radially. The correction force can be realized with an oscillating electric field like in Paul-Traps in Section 2.4 or with a static magnetic field as done for Penning-Traps in Section 2.5.

2.3.2 Axial confinement

Axial confinement is realized using a potential well. This can be shown by the analogy of a sphere on a valley hill, rolling down and up the other side as can be seen in Figure 5. As long as the hill is higher than the starting point, the sphere is confined inside and can not escape.

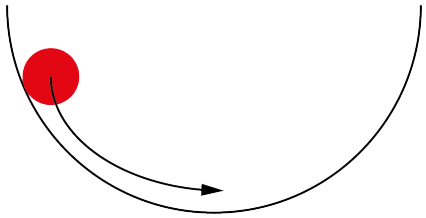

Figure 5: Sketch of a confined sphere

For subatomic and atomic particles this can be realized using an electric potential. The required voltage is depending on the energy of the particle and can be directly compared using the units Voltage (V) for the potential and electron volts (eV) for kinetic energy. Higher energies of the particle also require a slightly higher voltage on the confinement electrodes to trap the particle.

The schematic shows the electrodes in blue while the red line is the electric potential. U_0 denotes the ground potential while U_1 is the elevated potential satisfying the condition $U_0 \leq E_{\text{particle}} \leq U_1$. Positrons available in the laboratory have an energy between 5 and 10 eV.

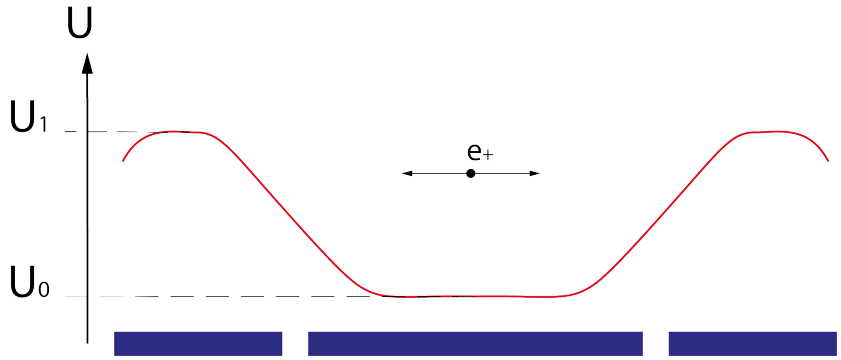

Figure 6: Schematic of an electric potential well - electrodes in blue, red line is the electric potential with U_0 denoting the ground potential while U_1 being the elevated potential

In order to allow for loading, one of the electrodes needs to be able to switch from ground U_0 to the desired trapping voltage U_1. This has to happen within the time the last positron of a pulse passes the entry electrode and the first of the bunch reaches the entry electrode after being reflected of the last electrode. The time needed can be calculated using the energy of the particle, using the Equation 2.3.1 for the kinetic energy since it is not travelling close to the speed of light. Thereby $E_{\parallel}$ is the energy of the particle, $m_{\mathrm{e+}}$ the mass of the positron and $v_{\parallel}$ is the speed of the particle in axial direction.

$$E_{\parallel} = \frac{m_{e+} \cdot v_{\parallel}^2}{2} \tag{2.3.1}$$

Rearranging this formula for $v_{\parallel}$ and using the known geometry one can calculate the maximum switching times, assuming that the positrons can travel both directions in order to capture as many as possible.

This time can be prolonged by raising the ground voltage U_0, slowing down the particle and increase the available switching time. In order to be as efficient as possible, the potential and kinetic energies of the positron need to be found in order to set the potential just below these values.

2.4 Paul Traps

Paul-Traps consist of two conical shaped electrodes and a ring shaped electrode as can be seen in Figure 7. Between the ring and the conic shaped electrode a potential is applied which creates a field shaped like a saddle point as shown in Figure 8. A constantly changing oscillating field is added to the static field, resulting in a rotating field when viewed from the particle perspective. This can be visualized by a ball on such a saddle-surface. When the surface is rotating at the correct speed, the ball remains confined in the centre, which can be nicely illustrated in some demonstration experiments [**rotatingsaddle**]. The oscillation frequency needs to be carefully chosen in order to successfully confine particles in its centre [**Major2006**]. Typical values for a Paul trap are stated in Table 4.

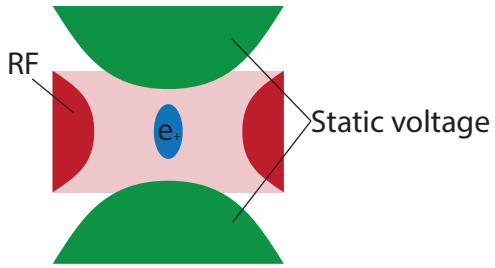

Figure 7: Schematic of a Paul Trap

Parameter	**Value**
size	1-5 cm
rf-amplitude	100-1000 V
rf-frequency	300-3000 kHz
dc-amplitude	±20 V
maximum ion density	10^6 cm^{-3}
storage time	multiple h
(uncooled) ion temperature	10 000 K
trap depth well	several tens of eV

Table 4: Typical values of a Paul-Trap [**Major2006**]

Looking at these values, the size would be suitable to fit inside the defined volume REQ 1, however the high voltage amplitude paired with the frequencies in the kHz make it unsuitable due to the necessary electronics and batteries required. If COTS electronics are used to generate the voltage and frequency, the size requirement can not be complied with.

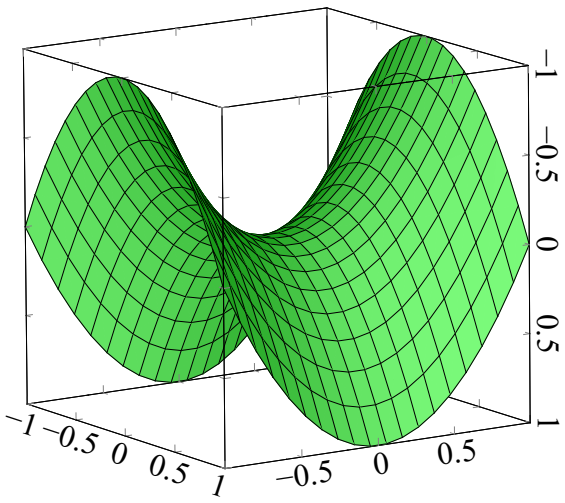

Figure 8: Example of a saddle potential [**Major2006**]

2.5 Penning Traps

Penning traps are also often used to trap charged particles. The difference to the previously described Paul-Trap is the use of static fields. By introducing a magnetic field in the experiment chamber, the particles are confined radially, while the electric fields confine it axially. This concept makes the application much more feasible for this specific case, combining magnetic and electric fields in order to confine fairly large amounts of particles. There are lots of variations of these traps, with the most important ones mentioned below [**Vogel2018**].
The principle for radial containment was briefly mentioned in Section 2.3.1, being the balance of Centripetal- and Lorentz-Forces acting on the particle 2.5.1 [**Stroth2011**].

$$|q| \cdot v_\perp \cdot B = \frac{m_{\mathrm{e}+} \cdot v_\perp^2}{r} \tag{2.5.1}$$

Thereby m_e denotes the mass of a positron, $v_\perp$ is the velocity perpendicular to the magnetic field lines, q_e is the charge of the particle and r is the radius of the orbiting particle. Rearranging 2.5.1, yields the larmor radius as can be seen in 2.5.2.

$$B \cdot r_\mathrm{L} = \frac{m_{\mathrm{e}+} \cdot v_\perp}{|q|} \tag{2.5.2}$$

For the set of parameters stated in Table 2 we obtain $r_L = 0.065\,\mathrm{mm}$.

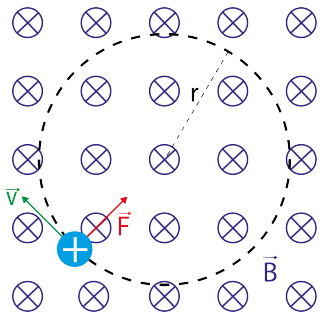

Figure 9: Larmor radius derivation [**Vogel2018**]

2.5.1 Variations of Penning traps

Hyperbolic Penning traps Hyperbolic penning traps consist of a ring and two endcaps with a hyperbolic shape, nested into each other as can be seen in Figure 10. Their main advantage is the creation of a homogeneous field between the electrodes, allowing for a precision measurements of charged particles. The magnets are not shown here, rather only the electrodes as well as the electric field. The disadvantages of this configuration are the difficult

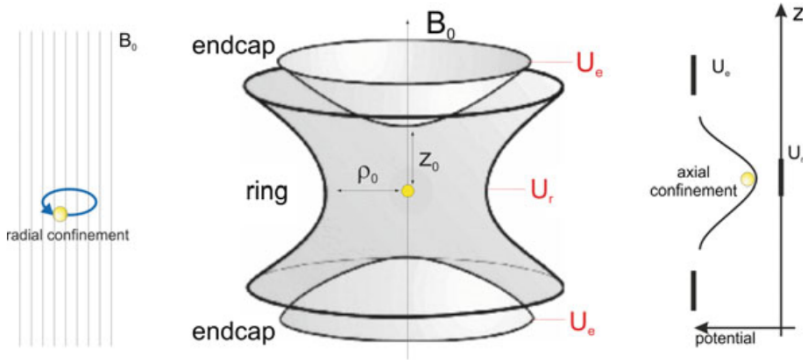

Figure 10: Hyperbolic penning trap [**Vogel2018**]

access in order to inject particles as well as monitor them. For this, holes need to be added, which disturb the electric fields as well as require precise injection of particles [**Vogel2018**].

Cylindrical Penning traps Cylindrical Penning traps are a widespread design with countless variations, ranging from closed- over open endcaps to multiple nested traps. One exemplary setup can be seen in Figure 11. These

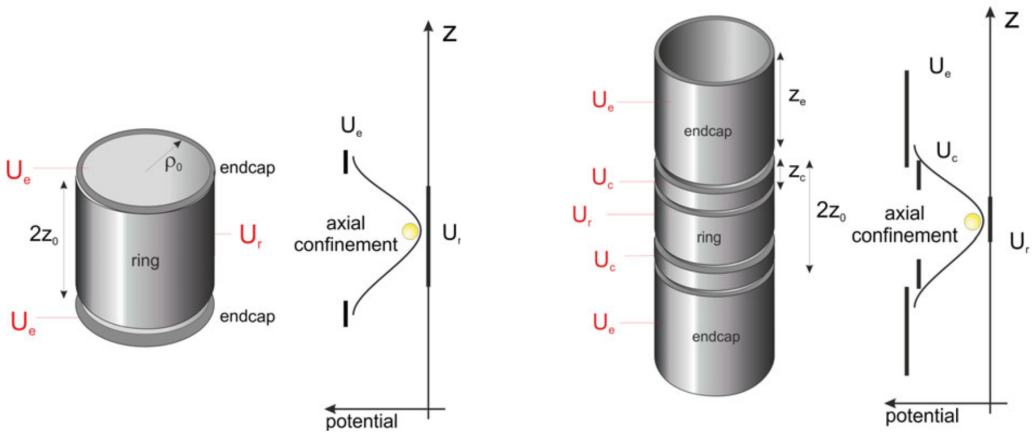

Figure 11: Selection of cylindrical trap designs [**Vogel2018**]

are only a few examples of designs. In practice, these principles are combined and advantages and disadvantages are exploited or altered in order to find the best concept for each experiment [**Vogel2018**].

Penning-Malmberg Trap The Penning-Malmberg trap is an evolution of the existing trap designs to store electrons over a longer time period by Malmberg and Dirscoll [**Malmberg1980**]. It is based on a cylindrical Penning trap, but has a much longer ground electrode, allowing for longer switching time as well as an increased amount of storage space of ion plasma [**Vogel2018**].

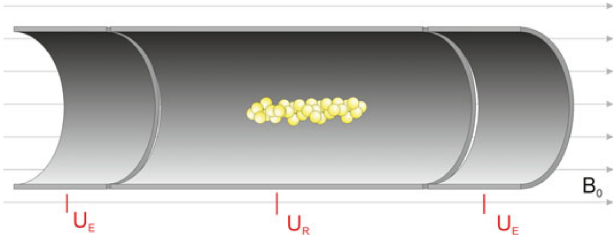

Figure 12: Penning-Malmberg trap design [**Vogel2018**]

Unitary Penning Trap The goal is the integration of the magnet into the electrode structure using permanent magnets in a compact trap. This is often used where a compact design is necessary and favorable to confine highly charged ions [**Vogel2018**]. Magnetic fields in the region of 1 T can be achieved with this design [**Vogel2018**].

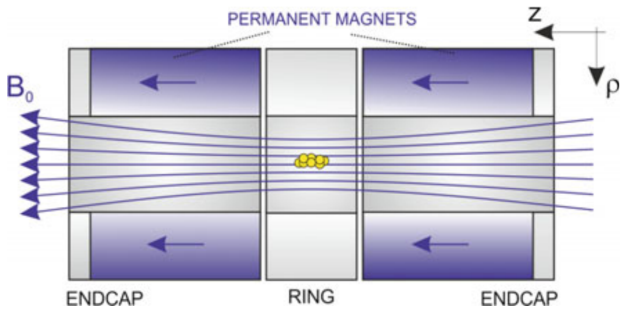

Figure 13: Unitary trap design [**Vogel2018**]

2.6 Motion of a single particle in a penning trap

After the previous analysis of different traps, the focus is now shifted to the positrons themselves. This analysis of particle motions starts with the derivation of motion which is the basis for the following investigation, before shifting the focus to trap imperfections and their influence on the stored positrons.

The equation of motion of a single particle in an electromagnetic field can be done following the calculations of Brown [**Brown1986**] and Kretzschmar [**Kretzschmar1991**] yielding the following:

$$\begin{aligned} \ddot{x} - \omega_c \dot{y} - \frac{1}{2}\omega_z^2 x = 0 \\ \ddot{y} + \omega_c \dot{x} - \frac{1}{2}\omega_z^2 y = 0 \\ \ddot{z} + \omega_z^2 z = 0 \end{aligned} \tag{2.6.1}$$

ω_i are the different oscillation frequencies of a confined charged particle and are also called eigenfrequencies or eigenvalues of the Hamiltonian of the confined motion [**Brown1986**] (citation toposi [4] on P.48 in Vogel)

- ω_c - cyclotron frequency
- ω_z - axial frequency
- ω_+ - modified cyclotron frequency/reduced cyclotron frequency
- ω_- - magnetron frequency

which can be calculated using the following formulas 2.6.2

$$\omega_c = \frac{q_{e+}B}{m_{e+}} \qquad \omega_z^2 = \frac{q_{e+}U}{m_{e+}d^2} \qquad \omega_\pm = \frac{\omega_c}{2} \pm \sqrt{\frac{\omega_c^2}{4} - \frac{\omega_z^2}{2}} \tag{2.6.2}$$

with d being the characteristic trap dimension consisting of r_0 as the radius of the trap and z_0 the length of the trap defined as

$$d^2 = \frac{1}{2}\left(z_0^2 + \frac{1}{2}r_0^2\right)$$

These oscillation frequencies are all connected by the invariance theorem:

$$\omega_+^2 + \omega_-^2 + \omega_z^2 = \omega_c^2 \tag{2.6.3}$$

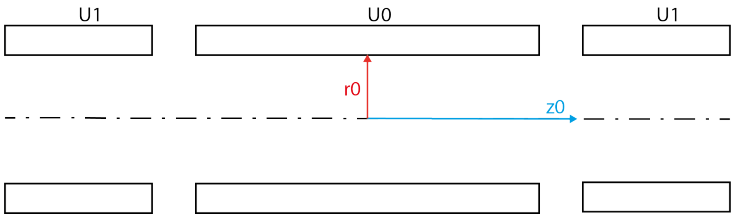

Figure 14: Definition of r_0 and z_0 with respect to the trap geometry

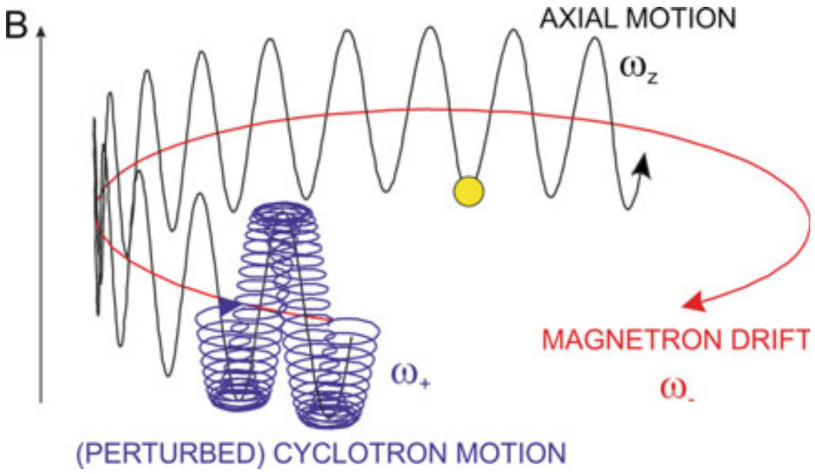

Figure 15: Visualization of the single particle motion [**Vogel2018**]

With this condition, the equations of motion 2.6.1 can be solved yielding the trajectories. These can be looked up in the book by Vogel [**Vogel2018**] as well as in papers by Kretzschmar [**Kretzschmar1991**] and Brown [**Brown1986**] and are displayed graphically in Figure 15.
For the previously mentioned parameters from Table 2, we obtain the values displayed in Table 5 In order to understand the influence of potential changes

Frequency	**Value**
ω_c	6.4 GHz
ω_z	70.7 MHz
ω_+	6.4 GHz
ω_-	388.8 kHz

Table 5: Oscillation frequency values

in the magnetic field strength, the change in the oscillation frequencies in dependence of the magnetic field is displayed in Figure 16.

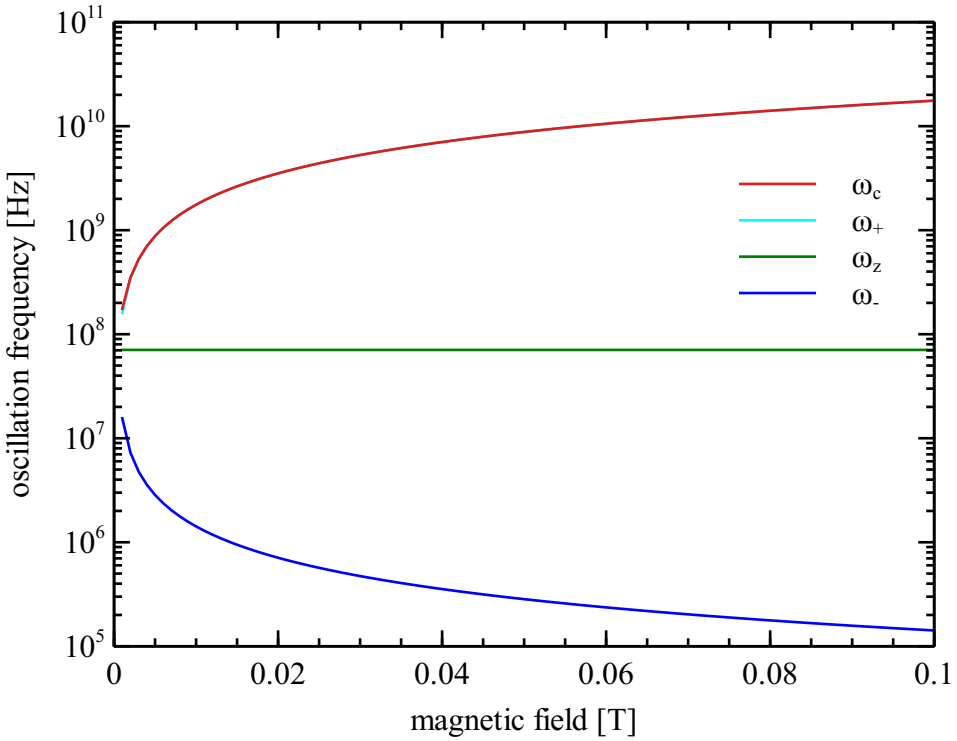

Figure 16: Sensitivity analysis on oscillation frequencies on the magnetic field

2.6.1 Stability criterion

The trapping stability can be described by the stability criterion 2.6.4, also defining a maximum limit for the maximum voltage as well as the sometimes called stability parameter $\gamma > 1$ with gamma being [**Vogel2018**][**Horvath1998**]

$$2\omega_z^2 = \omega_c^2 \qquad \text{or} \qquad \gamma = \frac{\omega_c}{\sqrt{2}\omega_z} \tag{2.6.4}$$

Combining this all together, a critical maximum voltage U_{MAX} can be defined above which the particles are lost.

$$U_{MAX} = \frac{1}{2} q_{e+} d^2 \frac{B_0^2}{m_{e+}} \tag{2.6.5}$$

Experiments showed that in practice, losses have to be expected if the trapping voltage is within $U_0/U_{\mathrm{MAX}} = 8/9$.
Practical experiments showed, that the effective maximum value is reached

at half of the stability criterion, as shown by Major et al. [**Major2006**]. Further, a critical mass to charge ration can be found by combining the previously found equations. Another conclusion can be made for a critical mass to charge ratio in 2.6.6 found on [**Vogel2018**]

$$\left(\frac{m_{e+}}{q_{e+}}\right)_{MAX} = \frac{d^2}{2}\frac{B_0^2}{U} \tag{2.6.6}$$

For the defined parameters in Table 2 we receive values for stability criterion displayed in Table 6

Frequency	**Value**
γ	64.2
U_{MAX}	$4.5 \times 10^4\,\mathrm{V}$
$m_{\mathrm{e}+}/q_{\mathrm{e}+}$	$235 \times 10^{-6}\,\mathrm{kg\,A^{-1}\,s^{-1}}$

Table 6: Stability criterion values

The values found in Table 6 show the chosen trap parameters being far from critical for positron storage.

Magnetron frequency and drift

One mayor problem that occurs at the crossed electric and magnetic fields is a drift motion. This happens due to a shift of energy at the transition between potential and kinetic energy. This means that if the energy of a certain oscillation decreases, another oscillation increases their energy and thereby their frequency.

$$\begin{aligned} E_k &= \frac{1}{2}m_{e+}v_-^2 = \frac{1}{2}m_{e+}\rho_-^2\omega_-^2 \\ E_p &= -\frac{1}{4}m_{e+}\rho_-^2\omega_z^2 \end{aligned} \tag{2.6.7}$$

Since for typical field choices, the confining fields dominate the kinetic energy by quite some margin ($\omega_z >> \omega_-$) in a way that the magnetron energy is always negative. For a visual representation we can view the particle orbiting the potential hill at the fixed magnetron frequency on a radius depending on its velocity. As long as there is no energy dissipation, this situation will not change. There are, however, several possible sources of energy dissipation:

- Energy dissipation through synchrotron radiation from the magnetron motion, reducing the motional energy and thereby increase the radius.

- Present residual gases causing collisions and reducing the magnetron energy resulting in an increase in orbit
- Resonant dipole excitation at magnetron frequency, increasing orbit velocity and through $v_- = \omega_- \rho_-$ will increase the radius

2.7 Analysis of imperfections on particle motion in real Penning traps

The following chapter will summarize the results found in the book "Particle confinement in Penning traps" by Vogel [**Vogel2018**] as well as papers by Brown et al. [**Brown1986**], Kretzschmar [**Kretzschmar1991**] and Horvath et al. [**Horvath1998**]

2.7.1 Imperfections of the Electrostatic Field

The goal is to analyze, how harmonic the potential is at the centre of the trap in order to correctly choose the electrode geometry as well as the required voltage. The effect of electrostatic imperfections is mainly important for the potential contributions of even order due to the trap symmetry. The imperfections have an influence on the particle motions, especially on the oscillation frequencies and can be seen as quadrupoles and octupoles with corresponding frequencies. The theoretical basis can be read in "particle confinement" and the referenced literature and is especially relevant if sensitive experiments such as mass-measurement of particles are to be performed [**Vogel2018**].

The electrostatic potential of a cylindrical trap such as a penning trap is given in Equation 2.7.1. There is the possibility to expand a Legendre polynomial, commonly used for spherical expansion and hyperbolic traps, or the cylindrical expansion of the electrostatic potential which will be shown here by expanding the Bessel function as a taylor series due to the cylindrical nature of the trap developed in this thesis [**Brown1986**, **Kretzschmar1991**].

$$U = U_0 \sum_{k=0}^{\infty} C_k \left(\frac{r}{d}\right)^k P_k \cos(\theta) \tag{2.7.1}$$

It uses the expansion 2.7.1 with $\cos(\theta) = z/(\rho^2 + z^2)^{1/2}$

$$\rho^n [\cos(\theta)]^{n-2j} = z^{n-2j} \rho^{2j} \tag{2.7.2}$$

Using these the electric potential U can be expressed using constants C_{2*i} defined as follows. C_0 is the overall potential offset without any influence on the particle motion. C_2 is the desired quadrupole term and a parameter for the "efficiency" of the trap. For hyperbolic traps it is of value $C_2 = 1$, for cylindrical trap it is $C_2 = 0.5$. The dominant electric imperfection is characterized by the term C_4 representing the octupole component of the electrostatic potential [**Kretzschmar1991**].

Effect of the electrostatic imperfections

For this we first analyze the parameters C_j. If the trap would be ideal, only C_2 would contribute to the total potential energy. With $U = U_0 C_2$ and close to the trap center is described with $\eta = \omega_z/\omega_+$ as:

$$\begin{pmatrix} \Delta\omega_+/\omega_+ \\ \Delta\omega_z/\omega_z \\ \Delta\omega_-/\omega_- \\ \Delta\omega_L/\omega_L \end{pmatrix} = \frac{6C_4}{C_2}\frac{1}{q_{e+}U} \begin{pmatrix} \eta^4/4 & -\eta^2/2 & -\eta^2 \\ -\eta^2/2 & 1/4 & 1 \\ -\eta^2 & 1 & 1 \\ 0 & 0 & 0 \end{pmatrix} \begin{pmatrix} E_+ \\ E_z \\ E_- \end{pmatrix} \tag{2.7.3}$$

From these equations we can then find empirical formulas that can be used for calibration of experiments in case of absolute mass measurements using the cyclotron frequency as well as other measurements that calibrate with an exact measurement of the magnetic field in the trap. This can be looked up in [**Vogel2018**, **Brown1986**] in more detail.

2.7.2 Imperfections of the magnetic field

We will look at the axial and radial components since we are working with a field rather than a potential. The expansion was done similarly as before for the electric potential and will therefore not be done again. The result can be seen in Equation 2.7.4 for a symmetric field in xy-plane for $z = 0$ [**Vogel2018**].

$$\begin{aligned} \vec{B}(\rho, z) = B_0\vec{e}_z + B_2\left[\left(z^2 - \frac{1}{2}\rho^2\right)\vec{e}_z + (-z\rho)\vec{e}_\rho\right] \\ + B_4\left[\left(z^4 - 3z^2\rho^2 + \frac{3}{8}\rho^4\right)\vec{e}_z + \left(-2z^3\rho + \frac{3}{2}z\rho^3\right)\vec{e}_\rho\right] + ... \end{aligned} \tag{2.7.4}$$

Effect of magnetostatic imperfections

Similar to before, the influencing parameter on the oscillation frequencies are B_2 and B_4. Therefore the frequencies shift with the energies and amplitudes of the motions. Close to the trap center this can be expressed as in 2.7.5 [**Vogel2018**].

$$\begin{pmatrix} \Delta\omega_+/\omega_+ \\ \Delta\omega_z/\omega_z \\ \Delta\omega_-/\omega_- \\ \Delta\omega_L/\omega_L \end{pmatrix} = \frac{1}{m_{e+}\omega_z^2}\frac{B_2}{B_0} \begin{pmatrix} \eta^2 & 1 & 2 \\ 1 & 0 & -1 \\ 2 & -1 & -2 \\ -\eta^2 & 1 & 2 \end{pmatrix} \begin{pmatrix} E_+ \\ E_z \\ E_- \end{pmatrix} \tag{2.7.5}$$

Similar conclusions to the electric fields can be drawn from this "The presence of shifts of the cyclotron frequency ω_C is of particular importance for all

measurements that rely on a calibration of the magnetic field strength by that quantity, or that want to perform absolute mass measurements via the cyclotron frequency in a known magnetic field." [**Vogel2018**]

Temporary field imperfections

Temporary field imperfections are important to keep in mind when designing an experiment. They become more and more relevant over the runtime of a measurement or experiment. The longer the greater the influence of these temporary imperfections become. Additionally their importance scales inversely proportional with the size of the experiment. Influences from the outside on the electric field can mostly be neglected due to the shielding nature of commonly used metals. For electric fields created by electrodes, small imperfections of them can result in voltage differences of up to hundreds of mV in small spaces as investigated for gold surfaces by Labaziewicz et al. [**Labaziewicz2008**]

These so called "patch potentials" and result in static field deviations, leading to changes in the cyclotron frequencies. They can be inherent to material imperfection as well as residuals due to the vacuum pumping, especially under cryogenic environments due to molecules freezing on the surfaces.

For magnetostatic fields the imperfections have different sources. External influences can not be neglected, because they can easily impact the the magnetic field. Superconducting coil magnets can be used to shield the system, but their cryostatic nature comes with great technical challenges. Another measure is the avoidance of magnetic materials, preventing the use of conventional steels and an increase in price. Inhomogenities of permanent magnets can be compensated by mapping the magnets as by Hugon et al. [**Hugon2010**] or tuned using iron plates as in Nuclear Magnetic Resonance Spectroscopy (NMR) and Magnetic Resonance Imaging (MRI) shown for example by Lee et al. [**Lee2010**] and Lorenzen et al. [**Lorenzen2001**].

Another cause for field disturbances are vibrations. This is an important topic in aerospace engineering, as well as sounding rockets, leading to the requirement of excessive testing and design decisions taking this into considerations. This can be through the use of rubbery materials to decrease vibration amplitudes, change the frequency or completely decouple vibrations from the structure [**Hibbeler2013**]. This problem can also arise in laboratories, where multiple experiments run in close proximity to required pumping and cooling causing vibrations.

2.7.3 Field misalignment

One major concern is the misalignment of the magnetic- to the electric field. This can be separated into two contributions, first only ellipticity and subsequently ellipticity in general and tilt of the electrodes themselves. The misalignment of the fields is described by the polar angle θ being the offset between the main axis of the magnetic field and the trap main axis and the azimuthal angle ϕ describing the angle in the plane normal to z.

Ellipticity

Ellipticity of the electric field is due to geometric imperfections. This is mainly due to manufacturing and assembly errors, mostly common when electrodes are split into multiple segments. In that case, the electric field has an elliptic shape and therefore influences the cyclotron frequencies and shifts them.
The ellipticity can mathematically be described by the term ε being proportional to $-\varepsilon(x^2 - y^2)/2$ being added to the total electrostatic potential [**Kretzschmar1991**, **Horvath1998**, **Breitenfeldt2008**].

$$U_\varepsilon = \frac{U_0}{2d^2}\left(z^2 - \frac{1}{2}(x^2 + y^2) - \frac{1}{2}\varepsilon(x^2 - y^2)\right) \tag{2.7.6}$$

and the corresponding potential energies

$$\begin{aligned} E_z(z) &= \frac{1}{2}m_{e+}\omega_z^2 z^2 \\ E_\rho(x,y) &= -\frac{1}{4}m_{e+}\omega_z^2(((1-\varepsilon)x^2 + (1+\varepsilon)y^2) \end{aligned} \tag{2.7.7}$$

The parameter ε can be separated into four distinct cases:

- $\varepsilon = 0$ equipotential lines are circles - confinement possible
- $0 < |\varepsilon| < 1$ equipotential lines are stretched - confinement possible
- $|\varepsilon| = 1$ equipotential lines distort to straight lines - no confinement
- $|\varepsilon| > 1$ equipotential lines create hyperbolic saddle - no confinement

The misalignment will lead to a shift in the oscillation frequencies which will be denoted by a tilde in the following .

$$\tilde{\omega}_\pm = \sqrt{\frac{1}{2}(\omega_c^2 - \omega_z^2) \pm \frac{1}{2}\sqrt{\omega_c^2\omega_1^2 + \varepsilon^2\omega_z^4}} \tag{2.7.8}$$

with ω_1 being

$$\omega_1 = \sqrt{\frac{\omega_c^2 - 2\omega_z^2}{4}} \tag{2.7.9}$$

squaring 2.7.8, we derive the invariance theorem that was mentioned in the Invariance-Theorem 2.6.3

$$\tilde{\omega}_+^2 + \tilde{\omega}_-^2 + \tilde{\omega}_z^2 = \omega_+^2 + \omega_-^2 + \omega_z^2 = \omega_c^2 \tag{2.7.10}$$

The axial oscillation frequency ω_z will remain unaffected, however is depending on the radial frequencies

$$\omega_z^2 = 2\omega_+\omega_- = \frac{2\tilde{\omega_+}\tilde{\omega_-}}{\sqrt{1-\varepsilon^2}} \tag{2.7.11}$$

All this can be summarized to another critical value of mass to charge similar to 2.6.6

$$\left(\frac{m_{e+}}{q_{e+}}\right)'_{MAX} = \frac{2}{1+\sqrt{1-\varepsilon^2}} \left(\frac{m_{e+}}{q_{e+}}\right)_{MAX} \tag{2.7.12}$$

Ellipticity and Tilt

Adding to the ellipticity tilt, both possibilities of electric field misalignment are discussed here, moving closer to real traps. Taking the trap geometry as our reference, the magnetic field B is perceived as

$$\vec{B} = B_0 \begin{pmatrix} \sin(\theta)\cos(\phi) \\ \sin(\theta)\sin(\phi) \\ \cos(\theta) \end{pmatrix} \tag{2.7.13}$$

Using the equation of motion, the oscillation frequencies can be found in "Charged Particle Traps: Physics and Techniques of Charged Particle Field Confinement" by Major et al. [**Major2006**], here only the conclusion formulas for the oscillation frequencies for ellipticity and tilt are stated by Gabrielse et al. [**Gabrielse2009**] to being

$$\begin{aligned} \omega'_\pm &\approx \omega_\pm + \frac{1}{2}\omega_- \sin^2(\theta)(3 + \varepsilon\cos(2\phi)) \\ \omega'_z &\approx \omega_z \left(1 - \frac{1}{4}\omega_- \sin^2(\theta)(3 + \varepsilon\cos(2\phi))\right) \end{aligned} \tag{2.7.14}$$

with ω'_j referring to both ellipticity and tilt to distinguish the two parameters. Again the invariance theorem 2.6.3 is holding true

$$(\omega'_+)^2 + (\omega'_-)^2 + (\omega'_z)^2 \approx (\omega_c)^2 \tag{2.7.15}$$

This can then be used in order to define limits on tilt by using the small difference $\Delta\omega_c = \omega_c' - \omega_c$ resulting in

$$\Delta\omega_c = \omega_-' \left(\frac{9}{4}\theta^2 - \frac{1}{2}\varepsilon^2\right) \tag{2.7.16}$$

Now we can assume that either the ellipticity $\varepsilon = 0$ or tilt $\theta = 0$ leading to maximum values for the corresponding other

$$\theta_{MAX} = \sqrt{\frac{4}{9}\frac{\omega_+' + \omega_-' - \omega_c}{\omega_-'}} = \qquad \varepsilon_{MAX} = \sqrt{-2\frac{\omega_+' + \omega_-' - \omega_c}{\omega_-'}} = \tag{2.7.17}$$

2.7.4 Presence of multiple particles

Within the past chapters, one single particle was analyzed. However, in most experiments multiple particles are present, the equations of motions 2.6.1 need to be adapted. This adaption is done in the following for two particles at a distance r, defined as:

$$r^2 = (x_1 - x_2)^2 + (y_1 - y_2)^2 + (z_1 - z_2)^2 \tag{2.7.18}$$

The equations of motion for this system are:

$$\begin{aligned} \ddot{x} + \omega_c\dot{y} - \frac{\omega_z^2}{2}x + \frac{1}{4\pi\varepsilon_0}\frac{xq_{e+}^2}{m_{e+}r^3} = 0 \\ \ddot{y} + \omega_c\dot{x} - \frac{\omega_z^2}{2}y + \frac{1}{4\pi\varepsilon_0}\frac{yq_{e+}^2}{m_{e+}r^3} = 0 \\ \ddot{z} + \omega_z^2 z + \frac{1}{4\pi\varepsilon_0}\frac{zq_{e+}^2}{m_{e+}r^3} = 0 \end{aligned} \tag{2.7.19}$$

Since "The centre of mass of an ensemble of identical particles has the same equations of motion like a single particle, irrespective of the particle number, since the mutual Coulomb-interactions do not contribute to its motion" [**Vogel2018**] [**Thompson1997**], this can be expanded to an ensemble of particles according to calculations performed by Thompson and Wilson [**Thompson1997**].

2.7.5 Particle ensembles in penning traps

Further analyzing particle ensembles in Penning Traps, we encounter some limitations parametrized in terms of the plasma frequency ω_p being calculated as

$$\omega_p^2 = \frac{q_{e+}^2 n}{\varepsilon_0 m_{e+}} \tag{2.7.20}$$

resulting in the modified oscillation frequencies

$$\omega_z' = \omega_z \sqrt{1 - \frac{\omega_p^2}{3\omega_z^2}} \qquad \omega_\pm' = \frac{\omega_c}{2}\left(1 \pm \sqrt{1 - \left(1 + \frac{2\omega_p^2}{3\omega_z^2}\right)\frac{2\omega_z^2}{\omega_c^2}}\right) \tag{2.7.21}$$

leading to the Brillouin limit defined as

$$n_{MAX} = \frac{\varepsilon_0 B_0^2}{2m_{e+}} = 6.47 \times 10^{15} \tag{2.7.22}$$

Properties	**Positron amount**		**Units**
	n =10^3	n =10^5	
ω_p	1.78	17.8	kHz
ω_z'	70.7	70.7	MHz
ω_+'	6.42	6.42	GHz
ω_-'	388.8	388.8	kHz

Table 7: Positron ensembles in penning trap calculations

2.8 Positron accumulation

In order to perform experiments with positrons, one needs a source emitting them. In most cases, it is a radioactive $\beta+$ source, where through the decay of a proton, a neutron, a neutrino and a positron are formed. Some of these positrons can then be extracted and used for experiments. The technical aspects of a trap were previously described in section 2.3, while the following will focus on the application of these trapping principles and how they are used in reality. The information in the following chapter can be found in greater detail in "Plasma and trap-based techniques for science with positrons" by Danielson et al. [**Danielson2015**].

2.8.1 Buffer-gas trap

The Buffer-gas trap was first developed, built and tested by Murphy and Surko [**Murphy1992**] and consists of a penning trap variation combined with, as the name suggests, gases that ensure energy loss of positrons. The setup consists of a minimum of three electrodes in a ladder like field strength decrease. At the end, there is an outlet electrode trapping the particles and releasing them at a certain time. The gases used to capture and slow the positrons are nitrogen N_2 and CF_4 or SF_6 respectively. They have been proven to be best by Marler and Surko [**Marler2005a**], Greaves et al. [**Greaves2000**] and Marler et al. [**Marler2005b**] in combination with differential pumping to maintain a constant pressure between 1×10^{-3} and 1×10^{-6} mbar at the beginning and end of the trap. This setup allows to cool positrons down to energies of 0.025 eV and accumulate up to 1×10^{8} positrons and stored for multiple minutes as shown by Surko et al. [**SurkoGilbertGreaves1999**].

Advancements of these traps allowed to increase the amount of particles as well as their lifetime, see [**Danielson2015**] for a review.

2.8.2 UHV trapping

There are experiments that can not work with buffer gases and therefore require other trapping techniques. These are by far not as efficient as the previously mentioned buffer gas trap, but have their benefits due to possible use in niche experiments.

Electronic damping Positrons from a radioactive source are trapped coupling the axial motion to an external resistor attached to a network tuned to resonate with this axial bounce frequency first by Schwinberg et al. [**Schwinberg1981**].

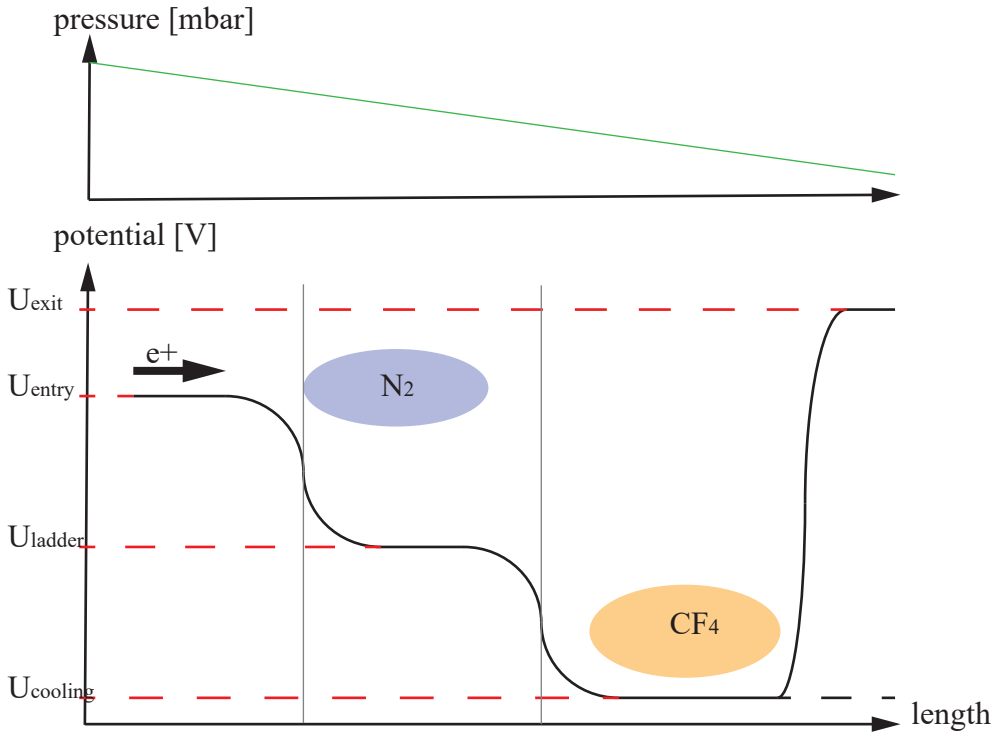

Figure 17: Working principle of a buffer gas trap [**Danielson2015**]

Moderator ramping Positrons from a moderator are trapped using a steady increase of the slew rate in order to avoid reflection by Conti et al. [**Conti1990**].

Collisions with trapped ions Using laser cooled ions in a penning trap can dissipate energy of the positrons through collisions in order to trap the positrons by Jelenkovic [**Jelenkovic2003**].

Other trapping techniques

Magnetic mirror Positrons can be trapped using a sudden increasing magnetic field, known as magnetic mirror. Trapping was able to be performed up to 10 s back in 1960 by Gibson et al. [**Gibson1960**].

2.9 Mobile traps

Applications for mobile traps

In the past there have only been a handful of examples of portable ion traps, and even less actual experiments performed, even though the application would have its need. The flexibility of experiments and medical applications as Positron Emission Tomography (PET) scanners or radiotherapy for detection and ultimate treatment.
Thereby the paper by Lewis et al. [**Lewis1997**] aimed at the possibility to transporting anti-protons from central production sites such as CERN or Fermilab worldwide, reducing experiment costs by keeping experiments stationary at their facilities by moving the particles to the experiment.
This would be especially beneficiary for radioactive isotopes required for PET scanning processes with decay times ranging from minutes to just below two hours resulting in a particle accelerator in close proximity. Even though this processes were simplified in the past years due to the miniaturization of ion sources, portable traps would enable more hospitals to use such evaluation and diagnostic methods as suggested by Braccini [**Braccini2016**].

A completely different application for mobile traps can be found in high-performance measurements of particle properties, allowing for measurement at a setup with extra sensitive apertures that would not perform to their full extend if situated in close proximity to particle generators. Challenging will be the stabilization of the particles during transport to prevent annihilation.

Practical realization of transportable particle trap

The only transportable trap that was found during research was a Penning trap storing electrons for a travelling distance of over 5000 km by
Tseng and Gabrielse [**Tseng1993**]. The magnetic field of 4.7 T was generated by a superconducting solenoid and an electrode voltage of 9 V, resulting in an axial oscillation frequency of 63.4 MHz of the positrons. The vacuum was maintained using a cryogenic setup to reach a temperature of 4 K. This configuration allows for the removal of external power supplys due to the self sustaining magnetic fields as well batteries for the electrode potential.

The experiment showed the possibility of antiproton storage in a mobile trap. Demonstrating the trap as well as the required procedures, the experiment was performed using up to 6×10^4 electrons and stored for 51 h. After this time, the trap was loaded into the transport truck with all the required supply materials, mainly liquid chemicals to maintain the cryogenic environment. The route of transport was from California to Massachusetts with one issue along the way, resulting in the loss of electrons due to an issue with a

frozen valve, requiring a heating step in order to continue the experiment. The experiment showed the possibility of transport as well as the required attention to detail required during handling in order to be successful.

Not functioning as traps itself, but rather take an in-depth look into autonomous pumping and transport are investigations by Schwindt et al. [**Schwindt2016**]. The team designed a miniaturized portable quadrupole Radio Frequency (RF) Paul trap to be used as an atomic clock of $1\,\mathrm{cm}^3$. Thereby they used NEG material strip for Yb in a metal-ceramic hybrid system and reduce the size of the atomic clock to $12\,\mathrm{mm} \times 11\,\mathrm{mm} \times 6\,\mathrm{mm}$. All the electrical elements are fitted inside in such a way, that multiple surfaces are used as confinement potential as well as being the location of the getter material itself. Using a copper pinch-off system ensured the small footprint of the clock as well as seal it permanently.

Further the capabilities of NEG was confirmed by Sertore et al. [**Sertore2011**], where they showed that a NEG pump is able to sustain UHV vacuum levels of $10^{-11}\,\mathrm{mbar}$ for more than a month. This enables them to improve their research in photocathode transport as well as show the possible applications of getter pumps for mobile applications.

2.10 Permanent magnet traps

There have been a couple of permanent magnet traps been developed over the years, trapping a variety of particles.

Heavy ions were store in a permanent magnet Penning trap in 2002 by Suess [**Suess2002**]. Thereby a special arrangement of NdFeB magnets was chosen in order to make the field as homogeneous as possible inside the trap and copper electrodes provided the electric field to trap the ions. The stored molecules were SF_6^- and $C_7F_{14}^-$ ions produced in Rydberg atom collision and was able to prove that stable trapping in such a simple trap is possible.

Another penning trap using permanent magnets is described by Tan [**Tan2012**] and Hoogerheide [**Hoogerheide2015**] arguing that superconductive coils produce homogeneous fields but are expensive, big and need lots of supplies around them. The use of NdFeB magnets is investigated in the trap, using the magnet itself for the ground potential between the electrodes. A first iteration investigates the use of a single NdFeB ring, before investigating the use of two rings and iron elements. These homogenize the field due to their magnetization in the center. Comparing this to a Helmholtz coil pair it can be show that the mayor disadvantage is the less homogeneous field. Nevertheless, the smaller size, weight and energy required at identical field strengths surpass the disadvantages.

Another permanent magnet trap was realized by Gomer [**Gomer1995**],

using an assembly of radially magnetized rings, segmented into 8 parts and assembled in order to counteract their field imperfections. Three of these rings with identical magnetization are stacked on top of each other to form a group. The whole assembly is then 2 groups, with opposite magnetization directions. This results in a homogeneous field between the groups for experiments due to adjustable distance between them. Correctly assembled, the magnetic field is only 1% inhomogeneous at 0.7 T and is able to store H^+ and H_2^+.

During the investigation of design for nuclear fusion,
Knapp and Barnes [**Knapp2017**] developed a penning trap using 16 NIB permanent bar magnets arranged in a circle to create a homogeneous magnetic field of 345 G along a length of 70 mm inside a steel structure. Due to the initial use of magnetic materials inside the trap, the magnetic field was distorted and component like the electron source had to be changed.

Also there has been investigations into miniaturized traps for atomic clocks, as by Schwindt et al. [**Schwindt2016**]. Thereby they designed a trap using NEG for Yb in a metal-ceramic hybrid system and reduce the size of the atomic clock to 12 mm × 11 mm × 6 mm. All electrical elements are arranged inside, using a couple of surfaces for multiple purposes such as walls used as electrodes.

2.11 Particle measurement

There are a variety of possible ways to detect subatomic particles and ions. They are mainly classified in two groups, one is the non destructive measurement of particles in a trap. The other solution can be using annihilation and measuring the emitted photons using detectors. Further, the application of Microchannel Plate (MCP) could be used inside the vacuum system while other detectors are used outside the experiment. These possibilities and their variations are analyzed in the following chapter.

2.11.1 Non-destructive measurement methods

Non-destructive measurements are of great interest if a particle shall be monitored over a longer period of time or the measurement is just on step of many in a experiment. The detection methods mostly base on the resonance of image currents and are known as "bolometric" detection published by Dehmelt and Walls [**DehmeltWalls**].
The trap is required to have a resonant detection circuit, attached to electrodes with the ability to produce optimum difference of induced image charges connected to the particle motion. Axial frequencies can be detected using RCL circuit attached to the endcaps while radial frequencies are determined using segmented radial electrodes.
Precision during manufacturing and assembling is key for the success, due to very low induced currents (pA) leading to easily obstructed signals with electrical noise.

There are lots of variations of traps having been used to detect such induced currents allowing for the measurement of mass, charge and spin as for example described by Smorra et al. [**Smorra2015**] in the BASE experiment at CERN, where antiprotons were stored in a penning trap for extended periods of time for measurements.

2.11.2 Destructive measurement methods

The principle has been used a lot, in nuclear as well as medical applications such as PET scanners. Previously, photons were detected using photographic emulsion discovered by Röntgen in 1895, detecting the first ionising radiation. This process aided Henri Becquerel with the discovery of radiating uranium salts, exciting some of the silver-halide-grains suspended in the film on the photographic paper. The development process then turns these grains into metallic silver, making them visible as darker areas on paper. These methods have been replaced with the development of new materials, technologies and processes leading to three main groups for photon detection

nowadays: Gas ionization, detection using semiconductor or detection using scintillation. They all base on the excitation of electrons either directly or indirectly via coulomb interaction. The following chapter is mainly based on the book "Experimental Techniques in Nuclear and Particle Physics" by Tavernier [**Tavernier2010**].

Gas amplification counters

Gas amplification counters are designed to localize trajectories of highly energized particles as well as with the use of proportional tubes for neutrons and low energy x-rays and beta-electrons. Due to their relative simplicity, these detectors are fairly inexpensive and wide spread. Most commonly used are Micromega Counters, where an inert gas is used to increase signal strength. It consists of anode strips for detection, quartz fiber on top to define the distance to the micromesh on top. Additionally a drift electrode is used to create the electric field for electron drift. Using inert gas such as Ar+10% isobutane allows for signal amplification to determine location, time and momentum of the radiation and subsequently, the location of annihilation can be determined [**Tavernier2010**].

Within the laboratory, such detectors are often used for precision experiments, however, they require a lot of design effort and time in addition to their delicacy in handling due to the materials used.

Semiconductors as ionisation counter

A semiconductor based detectors rely on the effect of ionizing radiation creating holes in the material by exciting an electron. Compared to gas amplification processes, they require less energy and yield a higher signal due to the significantly higher density of the solid material compared to the gas, but are also much more expensive.
The semiconductor atoms are connected with the valence electrons holding them together. The radiation ejects an electron which leads to a current if an electric field is present by closing the band gap between the conduction- and valence bands.

Such semiconductors can be used for gamma rays if they are made out of germanium. These are excellent detectors, however they need a lot of support supplies because they work efficiently in a cryostatic chamber cooled by liquid nitrogen. Silicon semiconductors are often used, but mainly for the tracking of charged particles like alpha radiation.

Scintillation counter

The most commonly used detector in nuclear and particle physics is the scintillator counter. It consists out of two parts, first there is a scintillator crystal that is fluorescent (radioluminescence) upon excitation of the molecules by ionizing radiation. This light is then guided to the Photomultiplier Tube (PMT) where a photocathode converts the optical into an electrical signal followed by an amplification stage.

Scintillator crystals The scintillator is a transparent crystal made out of organic or inorganic materials. Ionizing radiation excites the molecules, when returning to a ground level, the effect of radiolumniescence can be seen. This is a sometimes visual glow of the crystal like Lead-Tungstate ($PbWO_4$), sometimes the light is in the non-visual range such as with Barium Fluoride (BaF_2). Inorganic scintillators are mainly used to visualize x-ray and gamma-ray radiation, while organic scintillators can be used for particle tracking. There are also a couple gases and liquids that have scintillation properties, for example nitrogen glowing green as can be seen close to the poles as norther lights. The light created can be guided by wrapping the crystal in a reflective material, to a certain point for the next processes. Often times this is done by a Polytetrafluorethylen (PTFE) foil for an improved signal.

Name	**Density** [$\mathrm{g\,cm^{-3}}$]	**Light yield** [photons/MeV]	**Decay time** τ [ns]
NaI:TI	3.67	40000	230
BaF_2	4.88	1500	<1
$PbWO_4$	8.28	200	10
CsF	4.11	2000	3

Table 8: Typical scintillator crystal properties [**Tavernier2010**]

For pulsed positron beams, $PbWO_4$ scintillator proved to be most efficient for signal detection because it can be placed close to the annihilation region without saturating the crystal as shown by Cassidy et al [**Cassidy2006**]. This is enabled by the low light yield of the crystal in combination with a fast decay time as shown by Cassidy and Mills Jr. [**Cassidy2007**].

Photomultiplier Tube (PMT) A PMT consist of a photocathode on top of a glass vacuum tube and a multitude of dynodes at high voltages. The photocathode is able to convert the optical signal generated by the crystal into an electric one using the photoelectric effect discovered by Hertz [**Hertz**] and later explained by Einstein [**Einstein**]. Briefly summarized, it describes the effect of a photon hitting a often metallic part and thereby ejecting an electron on the other side. If the generated electrons hit these dynodes, more electrons are released, creating an avalanche effect in the process which serves the purpose of signal amplification. This signal is detected on the last dynode, also called anode and can be displayed on an oscilloscope.

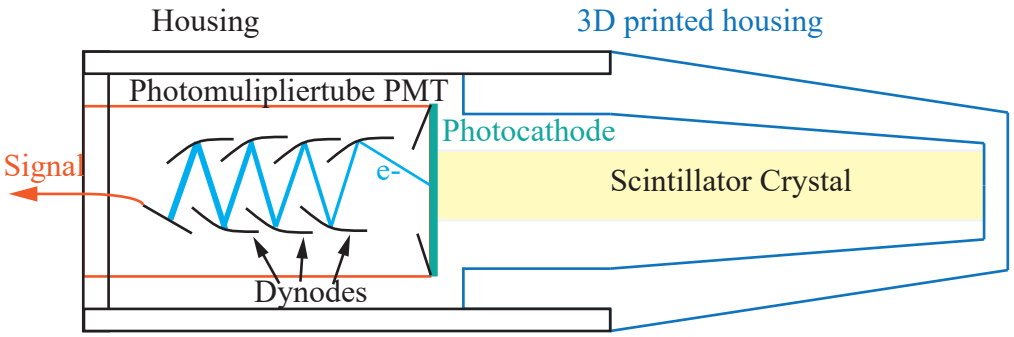

Figure 18: Sketch of scintillator functional principle

3 Vacuum component analysis

This chapter focuses on the ideas and developed concepts, evaluate them utilizing hand calculations, simulations as well as tests in order to converge towards the best solution under the defined requirements in Section 1.6 as well as validate the chosen parameters in Section 2.1, especially Table 2. First, the possible different vacuum components are analyzed, before moving on the physical design of the trap and the necessary structural verification using FEM simulations. Concluding is the description of a detector system and the developed parts for that.

3.1 Vacuum component analysis

This part will give the reader a broad overview over vacuum components and show the reasoning behind for selecting certain components for the experiment. The information in this chapter is mostly based on the book "Handbook of Vacuum Technology" by Karl Jousten [**HandbookVacuumtech16**] as well as the German translation "Handbuch Vakuumtechnik" [**HandbuchVakuumtechnik18**]. The chapter starts with a classification of vacuum ranges, the implications on component selection what this will mean for the component selection of seals, pumps etc. with respect to the previously defined requirements.

Vacuum ranges	**Pressure** [mbar]	
	min	**max**
Low Vacuum (LV)	3.3×10^{1}	1.0×10^{3}
Medium Vacuum (MV)	1.0×10^{-3}	3.3×10^{1}
High Vacuum (HV)	3.3×10^{-6}	1×10^{-3}
Very High Vacuum (VHV)	1×10^{-9}	1×10^{-6}
Ultra-High Vacuum (UHV)	1×10^{-12}	1×10^{-9}
Extreme Ultra-High Vacuum (XHV)	$\leq 1 \times 10^{-12}$	

Table 9: Classification of vacuum ranges [**Berman1992**]

3.2 Standard vacuum connections

In order to be able to assemble, disassemble, exchange and maintain components, removable connections are necessary. They need to seal the system for the required vacuum levels while still being able to open and close rather fast and simple. A couple of process-related requirements:

Pressure range	**Leak tightness**
Outgassing behavior	**Magnetizability**

The common ground of all the following components is a sealing medium ensuring a minimum leak rate [**HandbookVacuumtech16**].

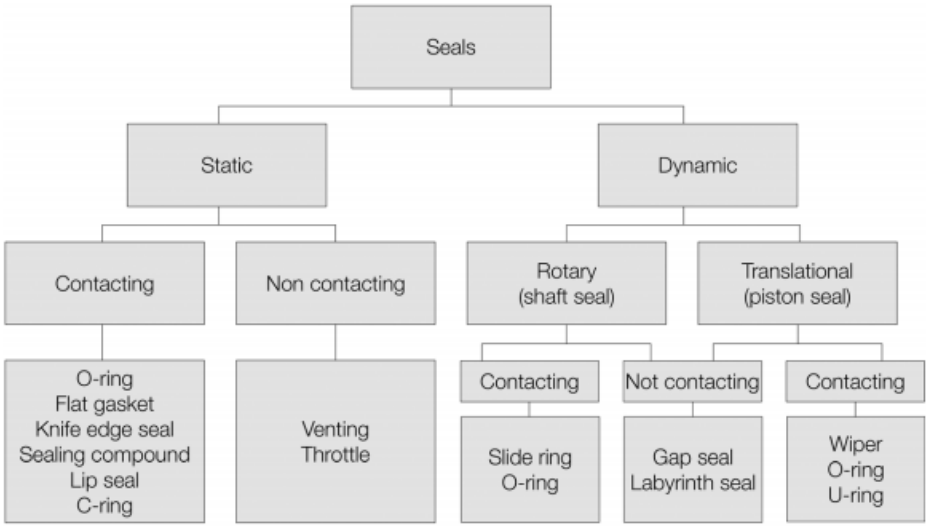

Figure 19: Seal type classification[**HandbookVacuumtech16**]

3.2.1 Materials for vacuum applications

In order to reach and sustain the previously mentioned vacuum levels, only a selection of materials can be used due to outgassing properties. Outgassing is the release of atoms and molecules under vacuum. This can be entrapped foreign substances as well as water that is evaporating and have many more reasons. This effect narrows down the available materials for vacuum application. A selection of usable materials is given in Table 10

3.2.2 Seal medium

Depending on what levels of vacuum shall be reached, a different sealing medium shall be chosen. There are different materials for selection, but in general it can be divided into polymer or metals.
These two materials are available as standardized components in various shapes for different connection types. They all have different advantages and disadvantages which will be evaluated in the following.

Material	Properties
Stainless Steel (SS) 304	slightly magnetic
Stainless Steel (SS) 316	non magnetic
Aluminum (AL)	non magnetic
Oxygen Free High purity Copper (OFHC)	low outgassing
Polyetheretherketon (PEEK)	low outgassing
Macor	machinable ceramic
Kapton	low outgassing
Fluoroelastomer (FKM)	rubber seal

Table 10: Selection of HV materials [**HandbookVacuumtech16**]

Polymer seals

Polymer seals are commonly used to seal vacuum systems from their surrounding. They take advantage of the pressure difference in the system in order to properly seal as can be seen in figure 20 Polymer O-rings often use a

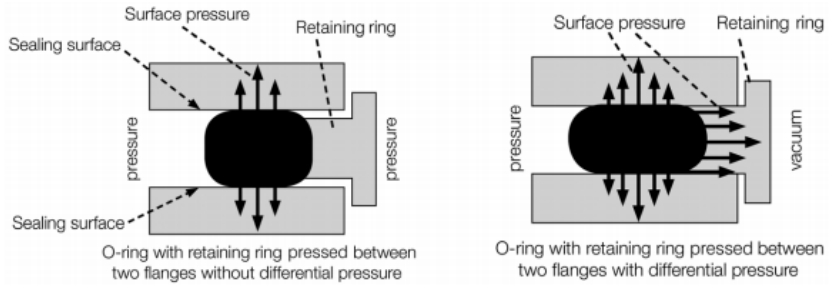

Figure 20: Rubber seal function principle for KF flange system [**HandbookVacuumtech16**]

lubricant which needs to be carefully chosen for the application. This choice is mainly dependent on the vacuum levels that shall be achieved, maybe even to not use grease for HV applications.

Metallic seals

Metallic seals are available in different shapes, sizes and out of lots of different materials as can be seen in Table 11. The most commonly used types for UHV are called gaskets, a flat ring commonly out of copper which seals due to plastic deformation during the assembly process. More about these types of seals can be found in Section 3.2.4.

Metal	**Temperature** ($°C$)	**properties**
Copper (CU)	400	low out gassing
Aluminum (AL)	200	use with aluminum gaskets
Nickel		corrosive environment
Gold plated CU	450	high temperature bake-out
Silver plated CU	300	high temperature bake-out
Stainless Steel (SS)		
SS silver plated	450	

Table 11: Metallic seal materials and their properties

3.2.3 ISO and Klein Flange (KF) couplings

These flange systems are based on the standard DIN 28404:1986-10 "Vacuum technology; flanges; dimensions" [**DIN28404**] as well as standard ISO 1609:2020-01 "Vacuum technology - Flange dimensions"[**ISO1609**]. This is for the ISO types, there is another similar standard called Klein flange (KF) couplings which are described in standard DIN 28403:1986-09 "Vacuum technology; quick release couplings; clamped type couplings"[**DIN28403**] or standard ISO 2861:2020-02 "Vacuum technology - Dimensions of clamped-type quick-release couplings"[**ISO2861**] available in a great variety of sizes classified as DN 10, DN 16 (DN 20), DN 25 (DN 32), DN 40, and DN 50. [**HandbookVacuumtech16**] The difference between KF and ISO systems can be seen in Figure 21. These types of couplings are suitable for HV and

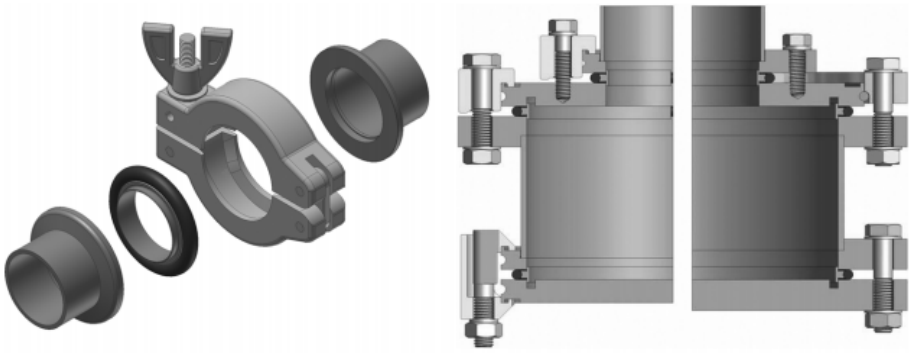

Figure 21: Different KF seals, left with clamps (KF), right with screws (ISO-F) [**HandbookVacuumtech16**]

UHV environments rated down to 10^{-9} mbar.

3.2.4 Conflat Flange (CF) and Quick Conflat Flange (QCF)

The other type of seal, even better suited for UHV applications are CF seals. They consist of a metal disc clamped between to standardized components. The knife edge of these penetrate the disc and seal the system from the surrounding due to plastic deformation as can be seen in Figure 22. Eventhough there are rubber gaskets available, metallic ones are most commonly used. The type of metal is chosen depending on the task at hand as well as the material of the flange itself and operating temperatures of the components [**HandbookVacuumtech16**].

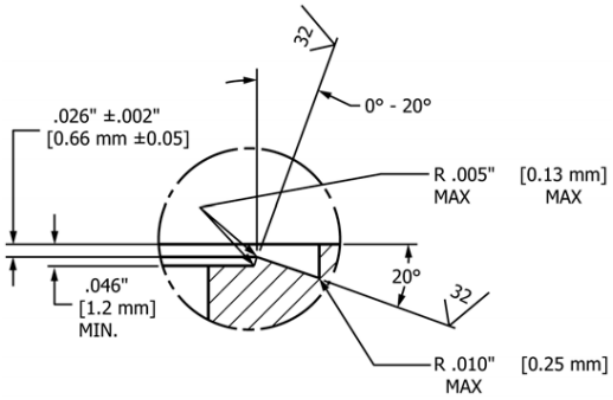

Figure 22: Dimension of CF knife edge according to ASTM E 2734 [**ASTM2734**]

The CF flanges are standardized under ISO 3669 "Vacuum technology - Bakeable flanges - Dimensions of knife-edge flanges" [**ISO3669**] as well as ASTM E 2734/E 2734 M:2010 "Standard Specification for Dimensions of Knife-Edge Flanges" [**ASTM2734**].
Another variation is the QCF flange, using an assembly of ring-segments with angled sides to clamp the special flanges onto each other to achieve the same effect as with CF components. This flange system makes most sense at ports that need to be opened regularly in order to maintain, insert or extract components of a vacuum systems. Both CF and QCF can be seen in Figure 23.

The CF flanges have certain dimensions, separated in multiple classes. An overview is given in Table 12 with the accompanying figure. These standard flanges are commercially available in a multitude of configurations, ranging from blank flanges over crosses to custom welded chambers with this connection type attached. This allows for standardized components that are exchangeable and can be replaced or upgraded depending on the requirement [**HandbookVacuumtech16**].

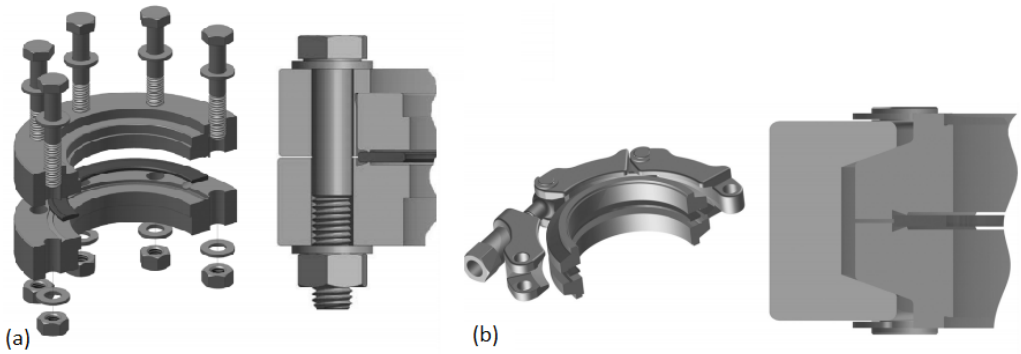

Figure 23: CF (a) and QCF (b) flanges [**HandbookVacuumtech16**]

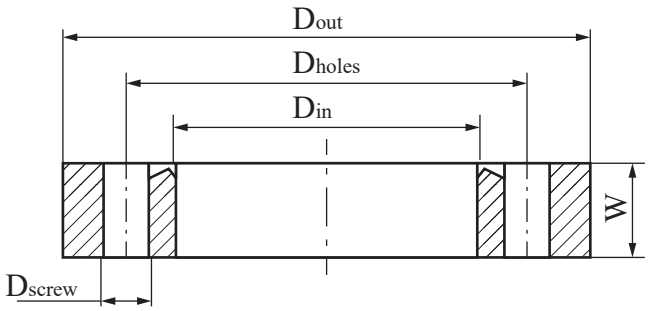

Figure 24: CF flange geometry [**HandbookVacuumtech16**]

DN	D_{out}	D_{holes}	D_{in}	W	D_{screw}
CF16	34	27	16	7	6xM4
CF40	70	58.7	40	12.5	6xM6
CF63	114	92.2	63	17	8xM8
CF100	152	130.3	100	19.5	16xM8

Table 12: Selection of CF flange dimensions [**HandbookVacuumtech16**]

3.3 Pumps for UHV applications

As previously shown in Section 2.2, a high vacuum is required in order to guarantee enough lifetime of the particles to perform measurements on them. This is realized by continuous pumping of particles using pumps. There are a lot of different pumps commercially available for a variety of applications. A selection is presented in the following section, while the interested reader can find out more in the "Handbook of vacuum technology" [**HandbookVacuumtech16**]:

Roughing pumps for HV-applications

- Piston pumps
- Membrane pumps
- Liquid ring pumps
- Rotary vane pump
- External vane pump
- Scroll-pumps
- Roots pumps

Special pumps for UHV-applications

- Ion getter pumps
- Titanium sublimation pumps
- Turbo-molecular pumps
- NEG pumps
- Cryopumps

3.3.1 Scroll pump

Scroll pumps are dry running pump running against ambient air. The principle was used for refrigerators due to their efficiency. They generate vacuum using two archimedean screws, entrapping air between them and forcing it out of the chamber and decreasing the pressure. The screws are turned by an electric motor and the pumps can mostly be run with a gas ballast like N_2 in order to improve pumping efficiency. Efficiency can also be improved by

staging multiple spirals after each other. They are able to reach a vacuum of 10^{-2} mbar and are ideal as a backing pump [**HandbookVacuumtech16**].

Figure 25: Functioning principle of a scroll pump [**HandbookVacuumtech16**]

3.3.2 Turbo-molecular pumps

Turbo-molecular pumps are based on the principle of transferring impulse onto the gas molecules and thereby direct particle movement. This can be compared to an aircraft or gas turbine, with rotors and stators compressing the molecules, creating pressure differences and moving the particles in the desired direction. These pumps work continuously and can be switched on and off fairly easily. The pressures that are achievable are as low as 10^{-9} mbar and such a pump can be seen in Figure 26. There are lots of

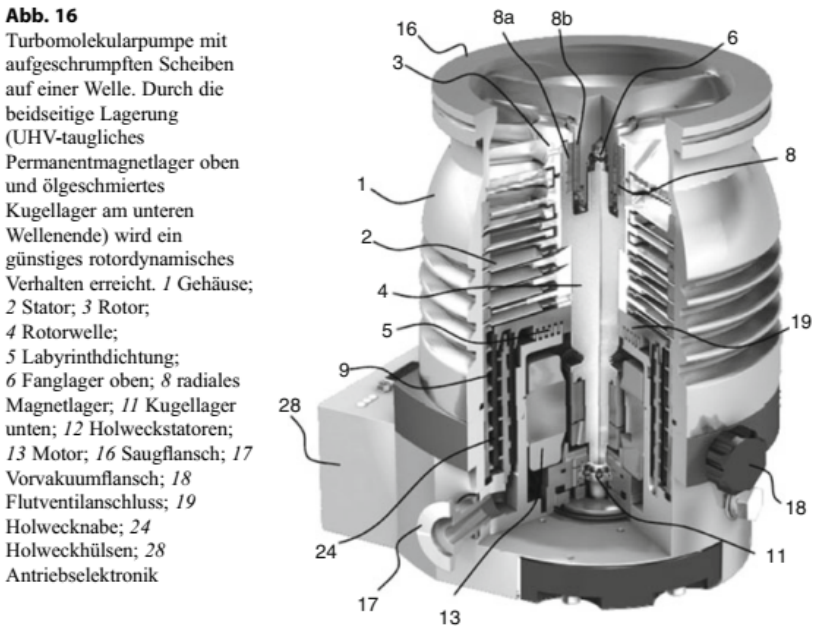

Figure 26: Description of a turbomolecular pumps [**HandbookVacuumtech16**]

different variations of the principle of these pumps, however they are not analyzed within this work but can be found in "Handbook of Vacuum Technology" [**HandbookVacuumtech16**].

3.4 Passive sorption pumps

The principle of sorption pumps is the binding of certain molecules and atoms to a surface. The word passive is due to the fact that once the surface is activated, no external power is required for work. The materials used for such pumps are porous with a high surface per volume like activated charcoal or zeolites.

3.4.1 Adsorption pumps

These pumps consist of a vacuum tight cavity filled with adsorbing material. Mostly artificial zeolites are used because activated charcoal is prone to explosion if subjected to sudden exposure to ambient air due to the oxygen. Once such a pump was vented at air or a venting gas, it can be regenerated by reheating the adsorbing materials to a certain temperature, usually between 250-350 °C [**HandbookVacuumtech16**].

3.4.2 Getter pumps

Getter pumps are based on three separate principles. First they adsorb molecules on their surface, secondly they solve the molecules into them and lastly they chemically bind them or parts of them in the getter material. More simplified, this means that the molecules are caught on the surface, from where they diffuse further into the material and get trapped close to grain-boundaries and voids. However, there are no distinct boundaries yet that separate these processes clearly from each other. [**HandbookVacuumtech16**]. Additionally, companies are reluctant to publish data in order to protect their financial interest and market position.
The temperature has an influence on the material characteristics, especially on absorption and chemical binding. An increase in temperature, contrary to the previously mentioned "adsorption pumps", increases the amount of particles that can be trapped. However, at a certain temperature, the particles held on the surface are being released again into the volume, requiring additional pumping for the activation and regeneration periods [**HandbookVacuumtech16**].

NEG Pumps One realization of such a getter pump is a None-Evaporative Getter (NEG)-Pump. They are able to chemically bind molecules in vacuum like CO, CO_2, N_2, O_2, H_2O, H_2 and some others. Most of the getter material is consisting of Titanium, Zirconium, Vanadium and alloys of these in a sintered or pressed form. To handle the pump with air, the surface is passivized using oxides, carbides and nitrites during manufacturing. Once the pump is installed, the passive layer is by heating to the regeneration

temperature. For this step an additional pump is running, removing these molecules from the volume [**HandbookVacuumtech16**].
A NEG pump is usually consisting of three mayor parts. The structure holding all the parts, the heating element in the center around which the third part, the getter material in disc or stripe form is mounted. Heating for small pumps can be done with a standard power supply, for bigger pumps a special monitoring system can be used that makes use of temperature sensor in the setup to constantly allow for monitoring of the pump [**HandbookVacuumtech16**].

Figure 27: Dimensions of a NEG Pump [**HandbookVacuumtech16**]

The advantage of these is the huge amount of pumping volume per component, which enables them to be used in places with size restrictions, weight requirements as well as required low vibrations. Additionally they can be used if magnetic fields are in close proximity due to the relative permeability being below 1.001.

The NEG pumps can be vented, as long as it can be ensured, that the temperature of the getter material is below 50 °C. Advantageous is the use of flushing with N_2 or Ar to keep increase the lifetime of the pump and slow the reduction of the pump down speed. Experiments by Lafferty [**Lafferty1998**] have found that 30 venting cycles with nitrogen leads to a reduction of 20 % of pumping speed, compared to 60 % reduction if ambient air is used. This was confirmed in communication with a NEG pump supplier upon request.

3.5 Valves for HV and UHV applications

"Valves are a feedthrough for gases that, according to demand, can admit, regulate, throttle, or interrupt the gas flow between two volumes." [**HandbookVacuumtech16**] They are consisting of a casing with ports, seals and some actuation mechanism. There are lots of different variations, with a selection being presented here.

Valve model	**Housing material**	**Seals**			**Pressure range**	**Max. T** ($^{\circ}C$)	**Qualities** & **applications**
		Case	**Valve seating**	**Movable**			
Angle valve 90°	SS/AL	Elastomer		- Hydroformed bellow - Edge welded bellow	HV	150	-Open, closed intermediate positions - Separation/connection of two systems
	SS	Metal	Elastomer	- O-ring sealed/	UHV	200	
		Metal		slide FT	UHV	200	
In-line valve 180°	SS/AL	Elastomer		- Hydroformed bellow - Edge welded bellow	HV	150	- Open, closed intermediate positions - Separation/connection of two systems
	SS	Metal	Elastomer	- O-ring sealed/	UHV	200	
		Metal		slide FT	UHV	200	
Butterfly valve 180°	SS/AL	Elastomer		O-ring sealed/ slide FT	HV	150	- Open, closed intermediate positions -Throttling of pumps -Downstream regulation -Low Space req
Gate valve 180°	SS/AL	Elastomer		-Hydroformed bellow -Edge welded bellow	HV	150	-Open, closed intermediate positions -Throttling of pumps Downstream regulation
	SS	Metal	Elastomer	-O-ring sealed	UHV	200	-Low space req.
		Metal		/linear FT	UHV	200	- Transfer valve

Table 13: Valve models with pressure ranges and typical application possibilities [**HandbookVacuumtech16**]

3.5.1 Gate Valve

Gate Valves are able to completely open and close the feedthrough. This is advantageous if particles need to be transferred from one part to another. Additionally they can be used as a safety system in order to close sections of and save experiments from exposure to air if needed. Example is a electric outage turning off all the electronics and automatic closing if pneumatically actuated. There are lots of different variations available, from materials, over seals to the actuation method of the mechanism. The combination of variations is depending on the setup. A very vital seal is the one between the valve and the actuation mechanism. If possible, a copper variation shall be used instead of rubber in order to avoid higher leak rates and improve the vacuum. If the disc shall be a full metal design, the design, weight and cost penalty are huge due to machining precision, high sealing forces and specialized materials and coatings [**HandbookVacuumtech16**].

There have been investigations made into customized gate valves in order to comply with REQ 1 from engineering companies. There are possibilities to adjust gate valves for REQ 1, however the mass can not be decreased easily. Additionally the high costs of up to 10 000 CHF due to customization rule out this option.

3.5.2 In-line valve

In-line valves are also very popular in theUHV regime. There are lots of variations, some have a straight channel, while others have a kink resembling a Y turned on its head. This kink saves space for the overall construction at the same vacuum leak rates as well as weight. So choosing the right design variation is vital for an experiment success [**HandbookVacuumtech16**].

There are customized solutions evaluated for such a valve, yielding a component of 130 mm × 130 mm × 75 mm as well as 5.5 kg. Commercial solutions are not found that have an unobstructed feedthrough for the positron loading step within the given size restrictions.

3.5.3 Angle Valve

Angle valves are commonly used in UHV applications and beyond. They have a 90° kink as can be seen in Figure 28. The housing can be made out of AL or SS. There are models suitable for HV as well as UHV applications, with the main difference is the material choice as well as the precision of manufacturing [**HandbookVacuumtech16**].

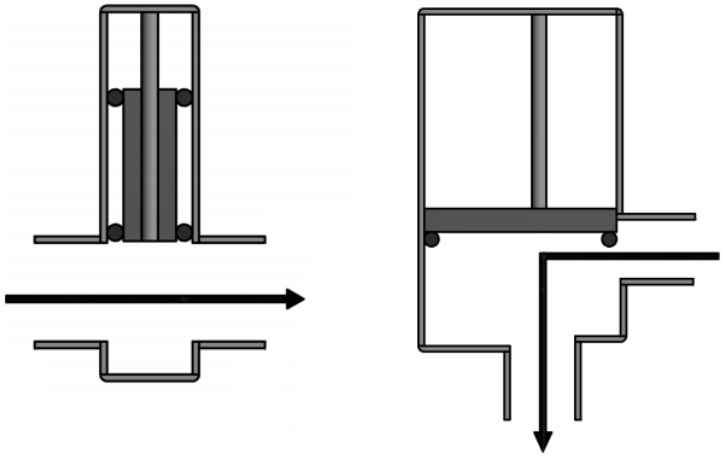

Figure 28: Functional sketch of gate valve (left) and angle valve (right) principle [**HandbookVacuumtech16**]

3.5.4 Cold-welded crimp tube

Another possibility to separate vacuum systems permanently is a permanent seal. This is often done by cold welding copper or other soft metal by clamping and compressing it into each other. In order for this process to being successful, forces exceeding $5000\,\mathrm{N^2\,mm^{-1}}$ are required to break the oxide layer open and get the pure atoms in contact with each other. If this is performed correctly, the seal is permanent and the leak rate is only dependent on the material itself. [**Schweisstechnik2014**]

3.6 Feedthroughs

Feedthrough (FT) are a way to get a medium or signal from outside to the experiment chamber inside the vacuum system. The two main things that need to get inside are electrical or optical signals in order to alter the experiment in a controlled way.

Electrical feedthrough

Electrical FT are made out of a bunch of components such as conductors, dielectric as well as a metal housing. They are joined together in such a way that they seal the system for the required application. Often these FT are adapted flanges as previously described in section 3.2.4. There are lots of variations possible, not only regarding flanges but also plugs and wires. For now we will evaluate the suitable insulation materials in Table 14, then take a look at various types of FT [**HandbookVacuumtech16**].

	Al_2O_3	Glass	Glass ceramics	Resin casting
Specific el. R at 20 °C [Ωcm]	$>10^{14}$	$>10^{14}$	$>10^{14}$	$>10^{14}$
Specific el. R at 250 °C [Ωcm]	$>10^{12}$	10^{9} - 10^{11}	10^{9} - 10^{11}	-
Max. baking out T [°C]	350 - 450	200 - 250	350 - 450	80 - 150
Leak rate [Pa L s^{-1}]	$<10^{-7}$	$<10^{-7}$	$<10^{-7}$	10^{-5} - 10^{-7}
Out gassing	Very good	Very good	Very good	Moderate

Table 14: Vacuum suitable insulation materials [**HandbookVacuumtech16**]

In order to feed electrical signals through the flange, often plugs are used on both ends and the connection is fixed on the flange to simplify the setup and allow flexibility. Thereby it is worth mentioning that the selection of the feedthrough and corresponding plug depends on what kind of signal needs to be transmitted. There are systems for high voltage switching since some experiments require this, others are simpler and use a more conventional plugs such as M12 screwable, BNC or SubD plugs. There are lots of different feedthroughs available and the right one has to be determined for every system individually, a selection can be seen in Figure 29 [**HandbookVacuumtech16**].

Figure 29: Selection of electrical feedthroughs, multipin KF feedthrough to the left, 4 pin UHV feedthrough from Allectra to the right

3.7 Bonding in vacuum environments

If UHV environment needs to be achieved, bonding becomes a delicate task. Therefore it is vital to select suitable adhesives for UHV application. This comes down mainly to the outgassing properties of the material. Since most adhesives are some form of polymer, outgassing is always critical due to long molecule chains and the reactions of those. Currently two-component adhesives are mostly used which are especially developed for vacuum applications. Most of them are developed for aerospace applications and are certified by NASA, ensuring high quality under extreme conditions [**HandbookVacuumtech16**, **ESA2011**].

Bonding procedure A critical step is the preparation of the component that needs to be bonded. The first step is to clean the parts and put them on a clean area on a table. Cleaning is often done using isopropanol, ethanol or even aceton and a ultrasonic bath can be used additionally. After drying, the adhesive is prepared before placing it in a vacuum chamber to remove entrapped air. After this, the adhesive is applied to the components with great care before placing them in vacuum again for curing. Once cured, it can safely be processed further.

3.8 Baking of vacuum system

Baking is an important step for good vacuum because the heat accelerates the evaporation of water on the components surfaces. Additionally it helps to remove diffused molecules from the very outer layers of the materials lattice structure. The heat can be produced in two ways, either through an integrated heater inside the setup or by heating the outside components and rely on conduction and radiation for transmission to all the components. Most commonly used is outside heating with heating tapes, heating tents or heating boxes as well as heating collars while pumping the system to remove the molecules. The maximum temperature is thereby defined by the "weakest" material in the camber and must not be greater than that in order to not damage these [**HandbookVacuumtech16**].

4 Structural component analysis

This section focuses on the structural aspects of connecting the experiment to the sounding rocket. Multiple design variations are investigated for their advantages and disadvantages to ensure selection of the system best suited to the task at hand.

4.1 Payload Structure

A major part of this thesis is the interface between the experiment setup and the launch vehicle itself. This interface is based on heritage as is previously described in Section 1.5. The size is restricted by REQ 1 and heavily influenced by the cubesat structure developed within ARIS. Furthermore, the interface shall be kept identical to exchange and combine different payloads.

After a preliminary study on standard components for vacuum systems with an estimated margin added, it was decided to choose the size of the payload as a 4U cubesat. The system is separated into two 2U sections connected with a clamp system and screws. This resembles the flight-proven system of project HEIDI with increased flexibility while decreasing assembly effort.

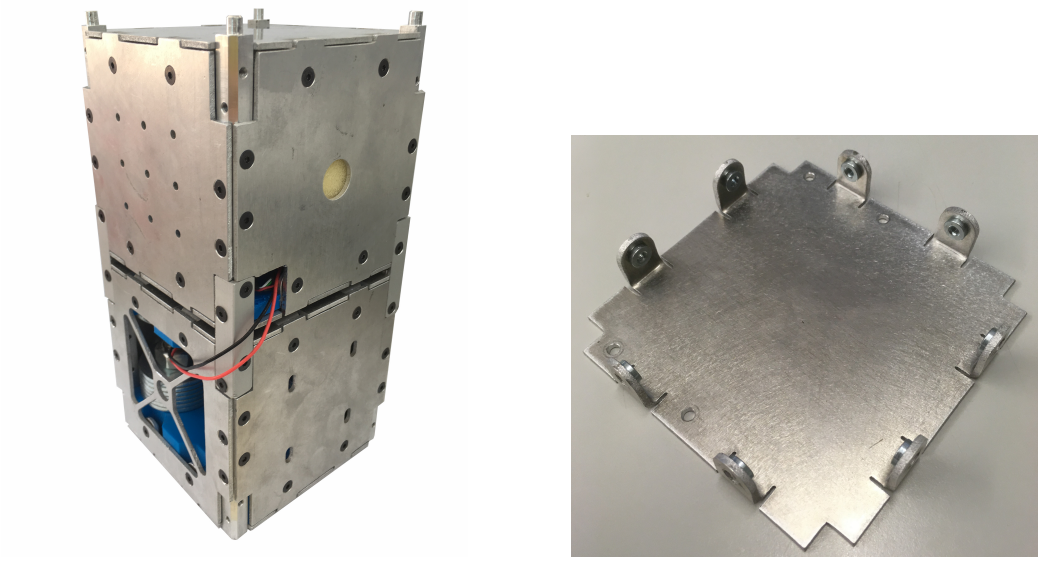

(a) (b)

Figure 30: 2U CubeSat developed by ARIS (a) and bent metal closing plate detail (b)

The first step after fixing the boundary systems is the generation of concepts on how to transmit the loads arising during flight to the structure. The screws connecting the CF components can be used to further connect to the structure, allowing for a reduction of parts and lower the system complexity. Additionally there needs to be a design, that transmits the loads to the load carrying structure and subsequently into the launch vehicle itself.

4.2 Structural design analysis

In order to integrate standard components, an interface structure needs to be designed, connecting the experiment to the launch vehicle. Thereby inspiration is taken from commercially available CubeSat structures as well as heritage from within ARIS.
The main concept is based on load carrying rods that attach to a rocket bulkhead. The mounting elements which hold subsystems of the payload in place are bolted to the load carrying rods. The different design options will be evaluated for their structural, modal and vibration characteristics and summarize advantages and disadvantages of each solution.

4.2.1 Bent metal plates

The first possibility is to use a similar setup as in project HEIDI, where a 2 mm AL sheet with bent parts is used as can be seen in Figure 30. They are attached to the facesheets, which in turn are attached to the load carrying rods. Eventhough this has been used in the past, it has a couple of disadvantages to it:

- Low load carrying capabilities (rip-through in the facesheets)
- Low material strength
- Press in nuts are not available in Stainless Steel - magnetic field disturbances if close to the magnetic field.

These points resulted in consideration of other design ideas to solve the task.

4.2.2 Bridge system

The bridge concept can be split in two variants, one having a bridge integrated into the rod, the other has the ability to fully demount the bridges from the rods.

Integrated bridges The first concept was developed due to the assumed high flight loads as defined by REQ 6. Therefore, two load carrying rods are integrated with a bridge made from a single 8 mm thick aluminum plate as can be seen on the left of Figure 31. These two frames are then connected using the mountable bridge with two M3 Screws per side. The load on the screws is effectively minimized and they can withstand the design loads. This is one of the most efficient ways of introducing the load into the structure. It keeps a certain degree of modularity and simplifies the work on the experiment, providing a wide range of access to all components with low effort. However, the main disadvantages are that the production is either costly if traditional milling processes are used or of low precision due to process induces imperfections using water- or plasma-cutting.

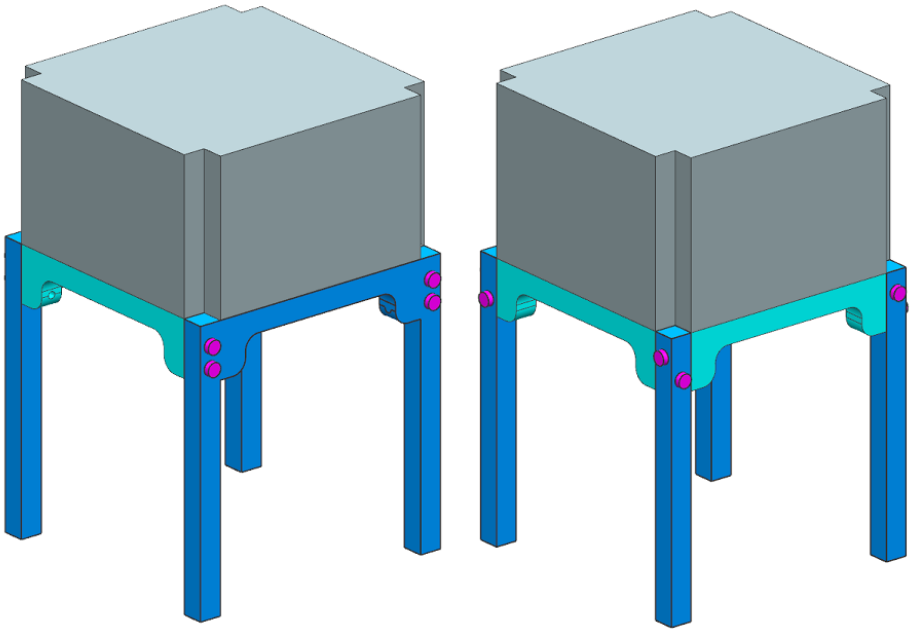

Figure 31: Frame (left) and bridge (right) concepts

Mountable bridges This is a variation of the integrated bridge concept previously described with all of the bridges being removable as can be seen

on the right in Figure 31. This is the favourable design due to its modularity and simplicity. Thereby one bridge has two holes each, of which only one is used. On one side it will be the upper one, on the other the lower one to ensure mountability.

In the following sectoin these two designs are analyzed in depth, using Computer Aided Engineering (CAE) in order to compare the designs and select the best to proceed further.

4.3 Structural Simulation

As a first step, the components are designed using Computer Aided Design (CAD). This is done using the programm Siemens NX12 and the model is directly loaded into the Finite Element Method (FEM) software (ANSYS 19.2, a finite element software for structural analysis). The geometry of the components is slightly simplified to achieve reasonable computation times and accuracy of the results. For example the screws are modeled as a cylinder with the screw core diameter of and a non-tapered head, constrained by the adequate contacts. The load is applied by modeling a mass of 4 kg as defined by REQ 2.

4.3.1 FE model preparation

This first section will be describing the model setup before analyzing the simulation results

Material definition The materials Aluminum EN-AW-6082 for the rods, bridges and frames and Austenitic Steel for the screws are assigned to the components as defined in Table 15. In order to use the acceleration tool, a mass is added to the system. The density of steel is taken and the volume is selected in order to achieve 4 kg.

	Steel INOX A4	**EN AW-6082**
E	200 000 MPa	70 000 MPa
$\sigma_{0.02}$	450 MPa	260 MPa
σ_{m}	700 MPa	310 MPa

Table 15: Material data used for CubeSat structural components

Contacts The subsequent step after material assigment is the definition of the right contact properties. There are 5 different types of contacts possible in Ansys which are:

- Bonded
- No separation
- Frictionless
- Frictional
- Rough

With the first two the calculation will be remaining the the linear region while the other three will move the calculations into the nonlinear regime. This results in drastically increased calculation time. Therefore, the simulation fist needs to run reliably in the linear regime before changes to the contacts shall be made.

For this model the contacts are selected such that the bolt is bonded to the bridge while kept frictionless inside the rod to allow for separation and resemble the torque applied on the screw. The contact between bridge and rod/frame is chosen to be frictional, since they are under pressure due to the screw, but can slide on one another. Lastly the mass is bonded to the bridges in order to introduce the loads we are interested in.

In the first time step of the simulation solely the bolt pretension is applied. Subsequently, the load cases are calculated one after the other. The simulation setup can be seen in Figure 32.

Meshing The next step is the meshing of the setup, where an automatic mesh is chosen for the overall geometry before manually refining critical areas. Those critical areas are the screws themselves with a mesh size of 0.5 mm and a surface mesh of the holes in the parts with a surface mesh of 1 mm. Adding to this, all the edges of the holes in frames, bridges and rods are refined by a factor of 2, allowing for the defeaturing of the mesh by said factor.

Boundary conditions The next step is the setup of the boundary conditions for the model. Since the rods are of 100 mm length the bottom plate is fixed in space. Additionally, the edges of the bridges are constrained such that only movement in the direction of acceleration is possible. This closely resembles reality where the bridges can hardly move due to the face sheets bolted to the outside, thus restraining the rods. Furthermore, the mass is

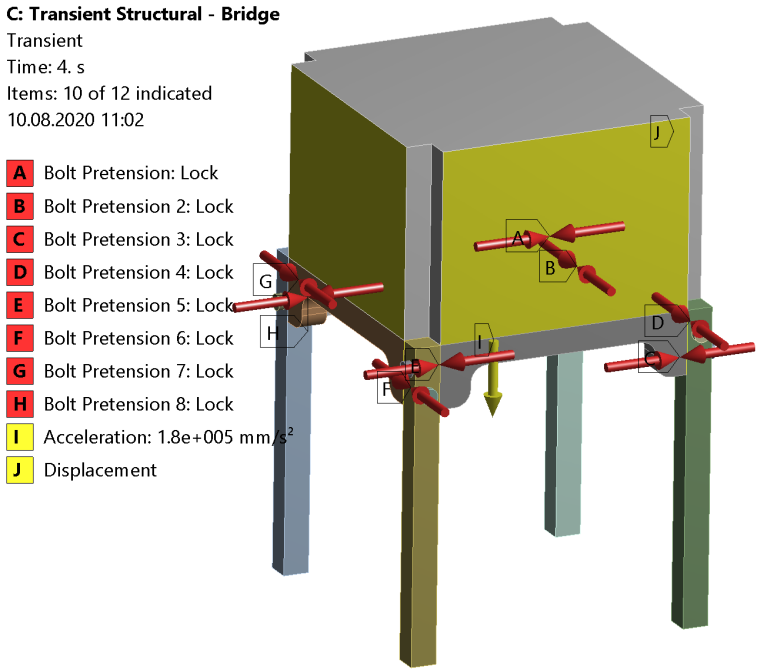

Figure 32: Simulation boundary conditions including bolt pretension

confined that it could only move in the direction of acceleration. These assumptions can be seen in Figure 32. The load is applied using the value of 18 g as defined in REQ 6. With this basic setup in place the model could now be further refined in order to converge closely towards the real system.

Comparison of Simulation approaches

With the model prepared the simulation results are compared using static structural as well as transient structural simulation approaches. The difference of those approaches is that the transient simulation is able to handle vibrations as input value to add another layer of possible evaluation criteria to the structure. The resulting values of the two methods in an identical setup are deviating by 1.6 %. This difference is most likely due to numerical errors and slight differences in the mesh. This in turn leads to the conclusion, that the chosen simulation approach will be the transient structural since it offers more possibilities to add further analysis at a later stage.

4.3.2 Analysis of integrated bridges concept

The first step is the analysis of bridges integrated into the rods to create a frame. This is done in order to have the highest strength and have the eight screws only carry about half of the load compared to the mountable bridges concept, since the other half will be carried by the frame itself. Simulating this design concept with the setup described above yields the expected maximum stress on the structure shown in Table 16. Notice, that the highest

Load case	**Full system**		**Frames**		**Bridges**		**Bolts**	
MPa	σ_{max}	σ_{avg}	σ_{max}	σ_{avg}	σ_{max}	σ_{avg}	σ_{max}	σ_{avg}
Bolt Pretension	188.0	32.3	35.3	12.0	65.7	19.3	188.0	63.8
Acceleration z+	187.6	32.6	36.5	11.8	77.9	19.5	187.6	64.6
Acceleration z-	188.0	32.5	43.3	13.0	77.2	19.4	188.0	63.4

Table 16: Frame design - Component maximum stress

stress arises due to the preloading of screws during assembly. The accelerations add just an insignificant amount of load on the part. Adding to this, the manufacturing is complex and tolerances can be difficult to maintain. Therefore alternative designs are investigated.

4.3.3 Analysis of mountable bridges concept

The analysis of the mountable, modular bridge design lead to the results seen in Figure 33 and the the stresses on the components can be seen in Table 17.

Load case	**Full system**		**Rods**		**Bridges**		**Bolts**	
MPa	σ_{max}	σ_{avg}	σ_{max}	σ_{avg}	σ_{max}	σ_{avg}	σ_{max}	σ_{avg}
Bolt Pretension	160.7	33.6	95.8	13.4	93.4	21.3	160.9	64.0
Acceleration z+	168.6	34.2	96.7	13.9	114.5	21.7	168.6	65.0
Acceleration z-	171.8	34.4	94.6	15.7	105.8	22.0	171.8	63.6

Table 17: Mountable bridge design - Component maximum stress

The analysis shows that the maximum stresses can be drastically reduced by reducing the pretension on the screws. Comparing these values to the maximum yield stresses of the respective materials in Table 15, the safety factors in Table 18 are obtained.

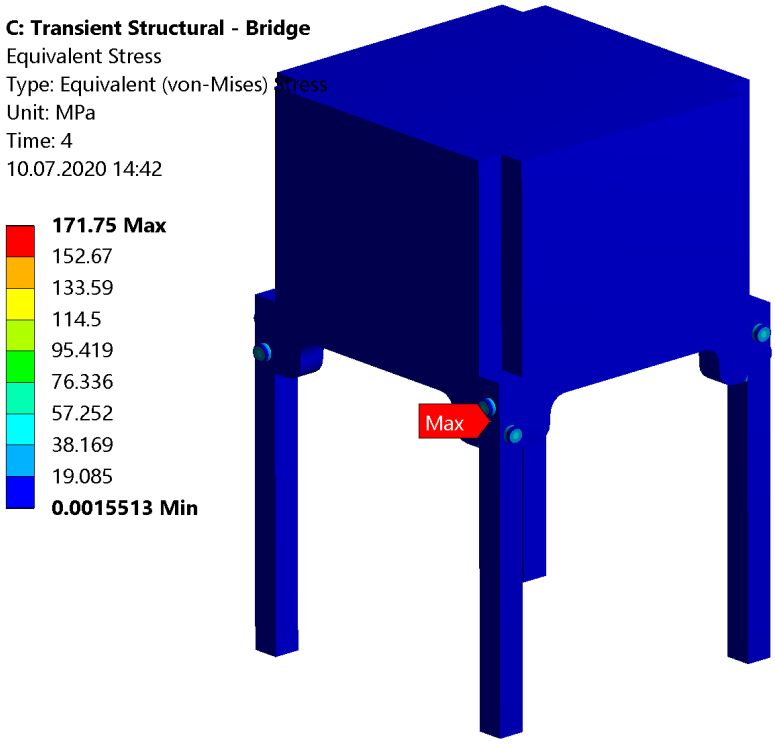

Figure 33: FEM simulation result for the bridge system

Load case	Rods	Bridges	Bolts
S_{fail}	2.7	2.4	2.6

Table 18: Mountable bridge design - Safety factors

These values suggest little risk of failure due to the parachute load in addition to the conservative assumption of a mass of 4 kg.

4.3.4 Experiment load introduction analysis

After the evaluation of the load introduction into the rods, the connection between bridges and the experiment chamber is investigated. For this, a split aluminum plate is proposed to mount directly to the CF interface available while fixing them with bolts to the bridges. This is done in a similar way with the representative mass as Structural steel with the size of 70 mm × 70 mm × 104 mm volume acting on the plates with an ”adapter” of CF Standard dimensions as referenced in Table 12. The plate is fixed onto the bridges where the end-plates are fixed in place to simplify the geometry

as can be seen in Figure 34. Thereby the assumption is made, that the screws including ishers distribute the load equally over the whole surface in order to simplify the simulations. The holes mounting the bridges will be fixed, while

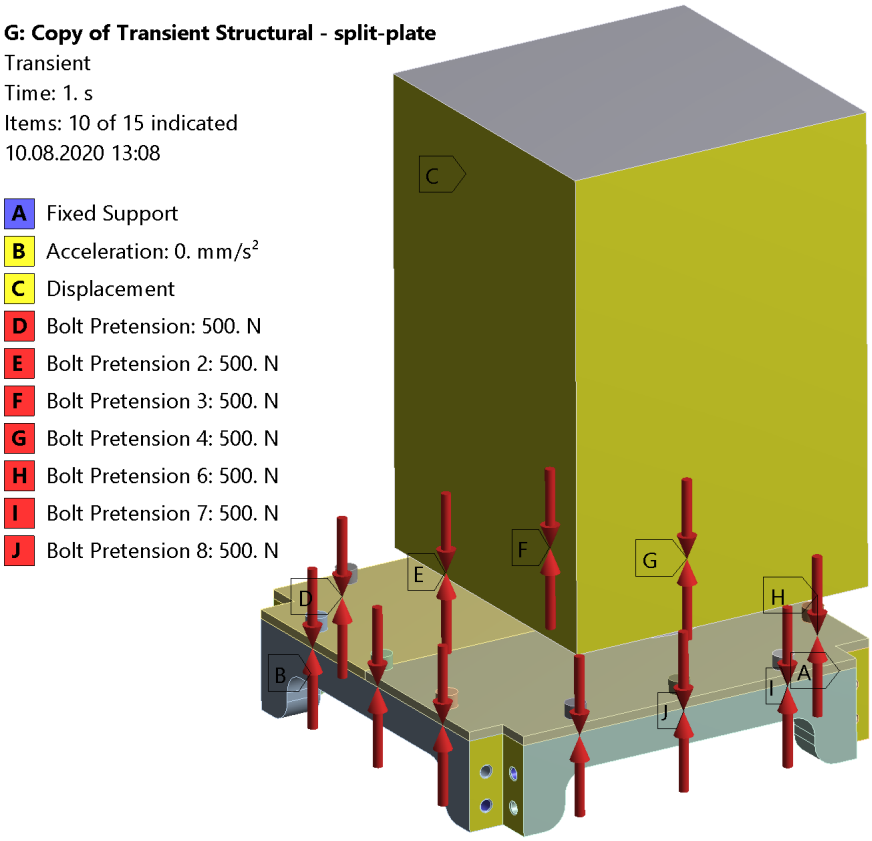

Figure 34: Model setup to simulate load introduction

the mass is free to move only in z direction. This is due to the assembly of the experiment which is guided in such a way using a second, similar plate around the pump assembly, only allowing for movement in said direction. The plate is held in place using M3x8 screws with a cylindrical head in the first step, with the diameter being the core diameter of the screw at 2.4 mm

The boundary conditions are selected to represent the load case as accurately as possible, the mass of 4 kg is bonded to the two plates. These are in a frictionless condition to save calculation time and simulate the possibility of the plates not touching in practice. The screws are in frictional contact with the plate and bonded to the bridge in order to apply the pretension. The plate itself is in frictional contact with the bridge, with the coefficient of friction being 0.2 as suggested in literature [**Roloff2011**]. The Bolt pre-

tension is selected to be 500 N on the 12 screws around the outside. These

Load case	**Full system**		**Plates**		**Bridges**		**Bolts**	
MPa	σ_{max}	σ_{avg}	σ_{max}	σ_{avg}	σ_{max}	σ_{avg}	σ_{max}	σ_{avg}
Bolt Pretension	248.6	3.1	51.2	0.5	63.1	2.5	248.6	30.1
Acceleration z+	250.8	16.9	133.3	18.4	99.0	5.8	250.8	39.0
Acceleration z-	388.0	20.1	155.8	21.8	61.4	5.7	388.0	50.6

Table 19: Split plate design - Component maximum stress

simulations lead to the critical part being the screw right next to the experiment chamber. This seems sensible since the plates undergo the highest deformation due to bending leading to the highest loads in the whole system. The simulation results can be seen in Figure 35 and 36.

The resulting value of 388 MPa should be acceptable for an A4-70 screw. With values from Table 15 this results in a safety factor for plastic deformation of $S_{\text{bolt0}} = 1.18$ and for failure of $S_{\text{bolt0}} = 1.80$. However, the screw is under a bending load which is unfavorable. In a further iteration of the simulation the failure of this specified screw was assumed to assess the impact on the system, yielding the following results. A maximum stress of 324 MPa is reached in the screw right next to the removed one. This means a safety factor of $S_{\text{bolt1}} = 1.38$. This is considered to be sufficient structural strength, to avoid loss of large components. The influence on the experiment in case of the failure of the screw however can not be estimated due to time constraint of the project.

Load case	**Full system**		**Plates**		**Bridges**		**Bolts**	
MPa	σ_{max}	σ_{avg}	σ_{max}	σ_{avg}	σ_{max}	σ_{avg}	σ_{max}	σ_{avg}
Bolt Pretension	248.7	3.1	51.2	0.5	63.1	2.5	248.7	39.1
Acceleration z+	251.0	18.9	154.5	21.4	85.9	5.5	251.0	43.6
Acceleration z-	323.8	24.4	179.1	27.8	60.7	5.0	323.8	61.7

Table 20: Split plate design - Component maximum stress - failed screw

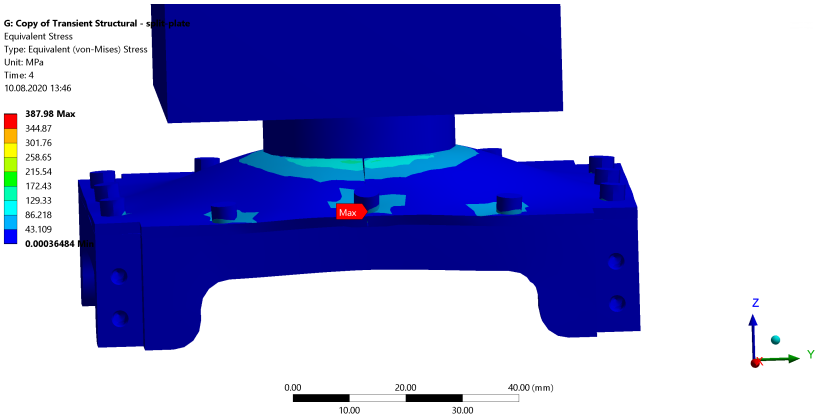

Figure 35: Full analysis of the split plate setup

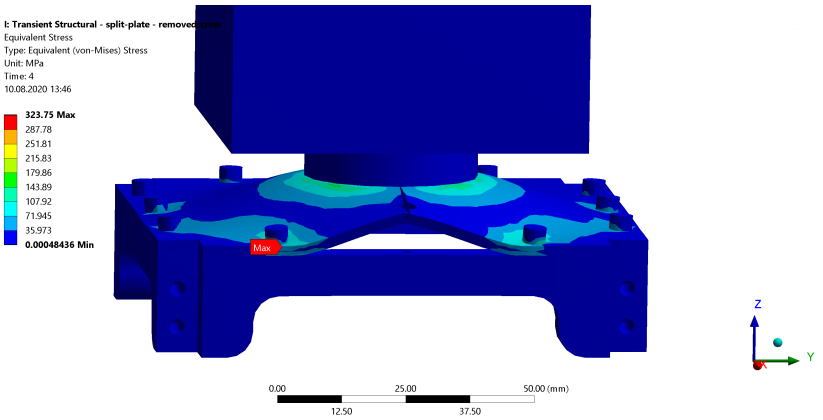

Figure 36: Full analysis of the split plate setup - removed screw

4.4 Eigenfrequency analysis

Another important analysis performed on the structure is an eigenfrequency test. Therefore, the structure is adapted and simplified in order to save calculation time and allow to solve the system due to student license limitations. This prevents the use of small components like screws etc., leading to a multitude of assumptions regarding the model. Since the clamping due to the screws can not be simulated, These surfaces had to be considered bonded to each other.

The Simulation is performed both for a preloaded and a non loaded model just for comparison. The results for the first 8 eigenfrequencies can be seen in Table 21 and the comparison is shown in Figure 37. The participation factor is a value expressing the percental amount of mass that is in movement for each of the modes. This means, that the highest modes need to be considered

more closely due to the fact that the amplitude and severity is greater.

Mode	**Frequency** [Hz]	
	Pre-stressed	**Non-stressed**
1	379.2	423.2
2	393.7	446.0
3	447.5	502.9
4	450.7	528.7
5	620.1	791.6
6	691.2	888.3
7	915.4	997.8
8	1065.0	1246.2

Table 21: CubeSat structure eigenfrequencies

Mode	**Frequency** [Hz]	**Effective Mass ratio**[%]		
	Pre-stressed	**x-dir**	**y-dir**	**z-dir**
1	379.2	0.19	74.98	2.91
2	393.7	74.83	0.09	0.09
3	447.5	0.06	9.43	24.91
4	450.7	8.98	0.05	0.11
5	620.1	0.12	0.02	0.17
6	691.2	0.00	0.00	32.80
7	915.4	0.27	0.00	0.00
8	1065.0	0.33	0.02	0.14

Table 22: Effective mass ratio for vibrations

As an example, the deformation of the eigenfrequency, the deformation of the third mode of the non-stressed structure is displayed in Figure 38.

These results need to be taken with a lot of care. The resulting frequencies are most likely an overestimation of the real frequencies due to bonded connections instead of screwed ones. Further the characteristic frequencies encountered during flight are unknown until now, due to a first test flight not being performed until this date. This can be updated and further analysis can be performed once these values are known. Nonetheless, a basic understanding of the system can be gained from this analysis. First and foremost the tendency that the eigenfrequencies for each mode decrease if the system is loaded with the forces it is subjected to during launch. The difference

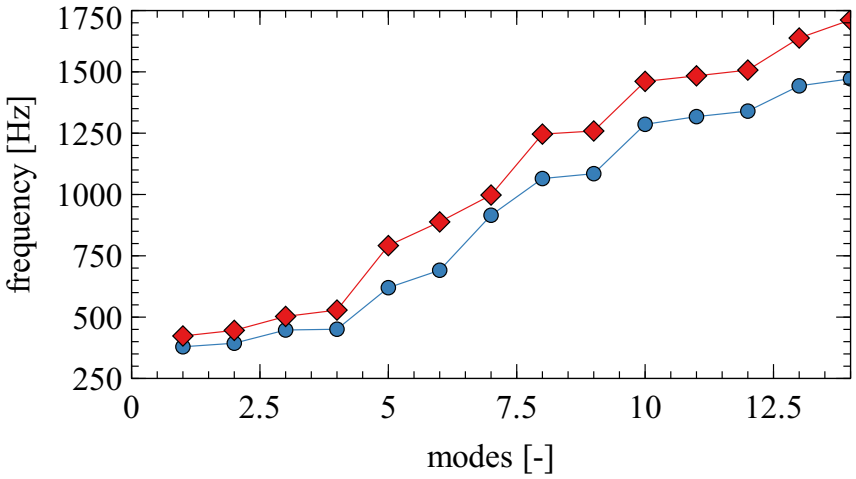

Figure 37: Eigenfrequency comparison of the CubeSat structure, pre-stressed in blue, non-stressed in red

increases with the mode increase, starting at around 50 Hz for mode 1 to a difference of 240 Hz at mode 14. It can be observed that most of the modes occur in pairs at a similar value. This is due to the fact that the movement can occur at a similar value in two possible directions. The non-compliance between modes 5 to 7 is most likely due to the fact, that the experiment setup inside the cubesat is off-center. This deviation from the central axis leads to a different mass and stiffness of the structure and thereby influencing the eigenfrequencies of the cubesat.

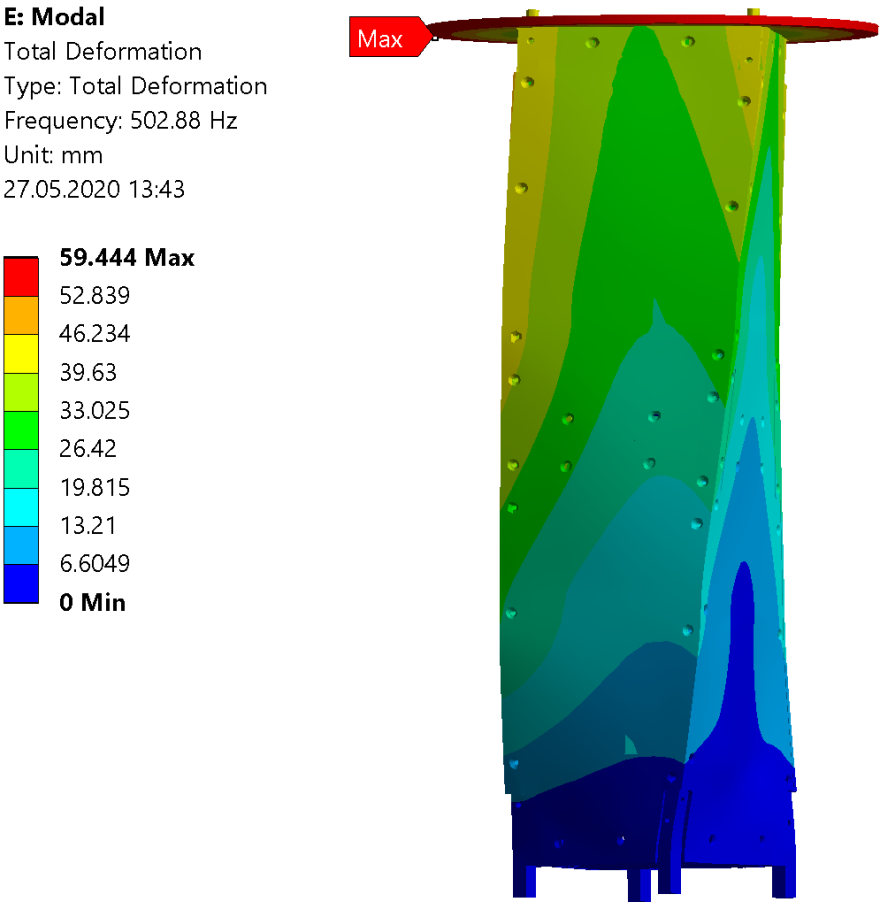

Figure 38: Deformation for the third mode of the CubeSat structure, non-stressed

5 Electric- and electromagnetic component analysis

This chapter will evaluate the proposed concepts for the electrical system, starting with coil calculations before moving on to electrodes. This section is concluded with the electronics required in order to switch the electrodes to voltage within nanoseconds as well as the annihilation signal detector.

5.1 Coil analysis

In order to generate the magnetic field, different possibilities are analyzed. Firstly, coils are evaluated for a runtime of 12 h to comply with REQ 9. In compliance with REQ 11 and REQ 2, the minimum required magnetic field strength is 60 G and the total mass must be under 4 kg.

Both solenoid coils as well as a Helmholtz coil pair are evaluated and compared in the following. First a general recap in electrical engineering is given to refresh the reader, before analyzing the specific coils in detail. The formulas mostly used can be seen in Equation 5.1.1 and 5.1.2

$$U = R \cdot I \tag{5.1.1}$$

$$P = U \cdot I \tag{5.1.2}$$

With U being the voltage in [V], R being the resistance in [Ω] and I the current in [A] as well as the Power P in [W].

5.1.1 Solenoid coil

In order to estimate the possibility of a solenoid coil, the required power for the magnetic field as well as the mass of the system are calculated. The used equations are stated in 5.1.3 and 5.1.4. It is important to note, that the amount of windings is corrected by a factor c in order to compare power requirements while generating similar magnetic fields as with the helmholtz coil pair in Section 5.1.2.

$$B_{sol}(z) = \mu_0 \frac{N_{sol} I c}{2 l_{sol}} \cdot \left(\frac{z + l_{sol}/2}{\sqrt{r_{sol}^2 + (z + l_{sol}/2)^2)}} - \frac{z - l_{sol}/2}{\sqrt{r_{sol}^2 + (z - l_{sol}/2)^2}} \right) \vec{e}_z \tag{5.1.3}$$

This is simplified for the center at $z = 0$ to

$$B_{sol}(0) = \mu_0 \frac{N_{sol} I}{\sqrt{(2 r_{sol})^2 + l_{sol}^2}} \vec{e}_z \tag{5.1.4}$$

Now using this formula the resulting magnetic field can be calculated in dependence of both the amount of windings N from 0 to 1000 in steps of 100 as well as the current I from 0 to 1 A in steps of 0.1 for all the possible combinations. The results for the magnetic field and power are plotted in Figure 39. The mass of such a coil assembly is between 1.19 kg and 11.9 kg,

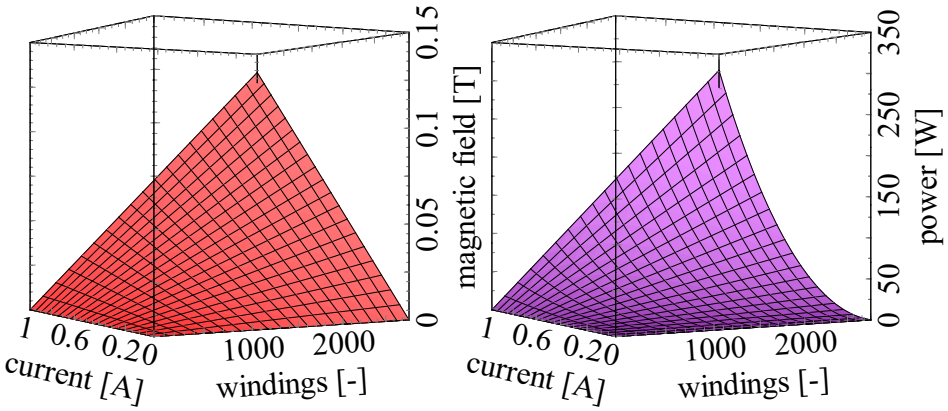

Figure 39: Magnetic field strength and required power of a solenoid coil

depending on the amount of windings using the assumption in Equation 5.1.5

$$m_{sol} = \rho_{wire} \cdot r_{wire}^2 \pi \cdot 2\pi \cdot r_{sol} N_{sol} c \tag{5.1.5}$$

The power consumption can be seen in Figure 39, with the maximum being at 320 W for all windings in series. Selecting now a magnetic field combination of 80 G, the power required is 3.8 W or 56.4 W h needing to be supplied by the battery. From this we know, that at a current of 0.8 A for 12 h REQ 9 we receive a charge of 9.6 A h. This amount of current can for example be provided by two batteries in series at 6 V with 5 A h each. The weight of such a solenoid will be 2.4 kg in addition to about 0.5 kg in battery weight for a "Swaytronic LiPo 2S 7.4 V 5200 mA h 35C/70C T".

5.1.2 Helmholtz-Coil pair

Another possibility to generate a homogeneous magnetic field is the use of Helmholtz-Coil pair. The formula derivation at the center for the z-direction is in 5.1.6 and 5.1.7.

$$B_{helm}(z) = \mu_0 \frac{NIR_{coil}^2}{2} * \left(\frac{1}{(R^2 + (z - d/2)^2)^{3/2})} + \frac{1}{(R^2 + (z + d/2)^2)^{3/2})} \right) \vec{e}_z \tag{5.1.6}$$

This can now be simplified assuming the ideal distance of the coils being their radius $a = R_{coil}$ the formula for the magnetic field in the center simplifies to 5.1.7

$$B_{helm} = \frac{8}{5\sqrt{5}} \cdot \mu_0 \frac{NI}{R_{coil}} \vec{e}_z \tag{5.1.7}$$

Now using this formula we can calculate the resulting magnetic field in dependence of both the amount of windings N as well as the current I as we did with the solenoid coil to receive plots in Figure 40.

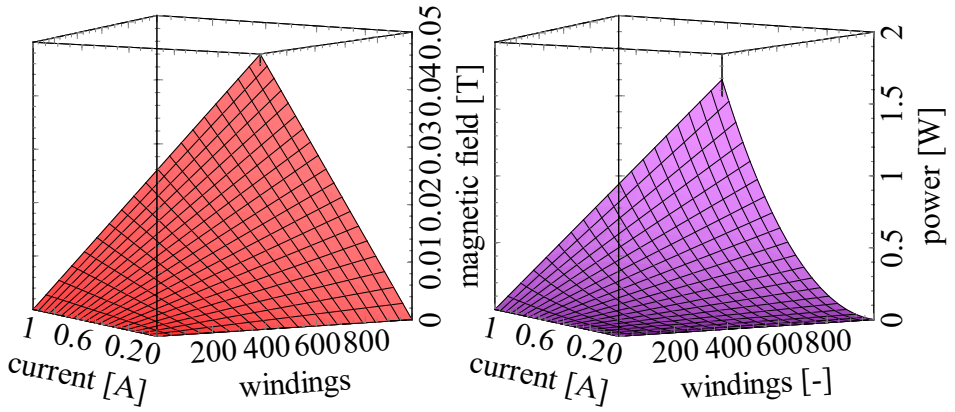

Figure 40: Power requirements for a Helmholtz-coil pair

The mass of the Helmholtz-coil pair is between 0.86 kg and 8.58 kg using the formula given in 5.1.8

$$m_{helm} = 2 \cdot \rho_{wire} \cdot r_{wire}^2 \pi \cdot 2\pi r_{coil} N_{sol} \tag{5.1.8}$$

Again as before, we will estimate the application at a reasonable magnetic field strength in the centre of 80 G. This corresponds to a power of 18.2 W h for 12 h of runtime at a continuous current of 0.8 A per coil. This then

corresponds to a minimum voltage of 2 V. Now selecting the same battery as we did for the solenoid "Swaytronic LiPo 2S 7.4 V 5200 mA h 35C/70C T" we put 4 of them in parallel in order to reach the required 19.2 mA h. The mass of the two coils adds up to 1.7 kg and the 4 batteries to 1.01 kg, resulting in a total of 2.71 kg. This means that the total mass is just 10 % lower than the solenoid coil system.

5.2 Permanent magnet analysis

An alternative to generate the magnetic field is the use of permanent magnets. Their unique ability to create high fields at low mass makes them interesting for this project. The common used type of material are rare earth magnets such as Neodymium with various alloys added to form NdFeB magnets. These are available in multiple grades and suitable for different strength and application temperatures.

5.2.1 Ring magnets

One possibility of permanent magnets is the use of ring magnets. Thereby a couple of limitations have to be considered, such as the assembly procedure and size restrictions. Therefore the inner diameter is limited by the outer diameter of CF components used defined in Table 12. Since there are only discrete sizes available, a couple were selected for a detailed investigation as can be seen in Table 23. The challenge with ring magnets in a coil-like

B_r [T]	$D_{out} \times D_{in} \times H$ [mm]	$T_{\max}$ [°C]	$B_{\mathrm{z,max}}$ [G]	n_{mag}	d_{mag} [mm]	Mass [kg]	L_{trap} [mm]
1.13	$56 \times 43 \times 3.7$	120	296	5	8	0.14	17
1.22	$76 \times 42 \times 5.0$	120	700	5	9	0.59	25
1.17	$55 \times 45 \times 105$	150	530	5	3	0.31	20

Table 23: Selected permanent magnet rings

configuration is, that even though they can be arranged to create an even magnetic field inside. However, the axial field has a zero crossing, resulting in a sign change of the magnetic field. This sign change can be problematic when considering the loading procedures of such a trap. Therefore a compensating field is required for that step. This effect can be seen in Figures 41 and 42. The required field strength in that region further scales with the magnets strength and has to be taken into consideration. The other point taken into consideration is the assembly procedure. Since the magnets may not be easily removable once the experiment is assembled will limit the bake-out temperature of the system due to the temperature dependence of the magnetization.

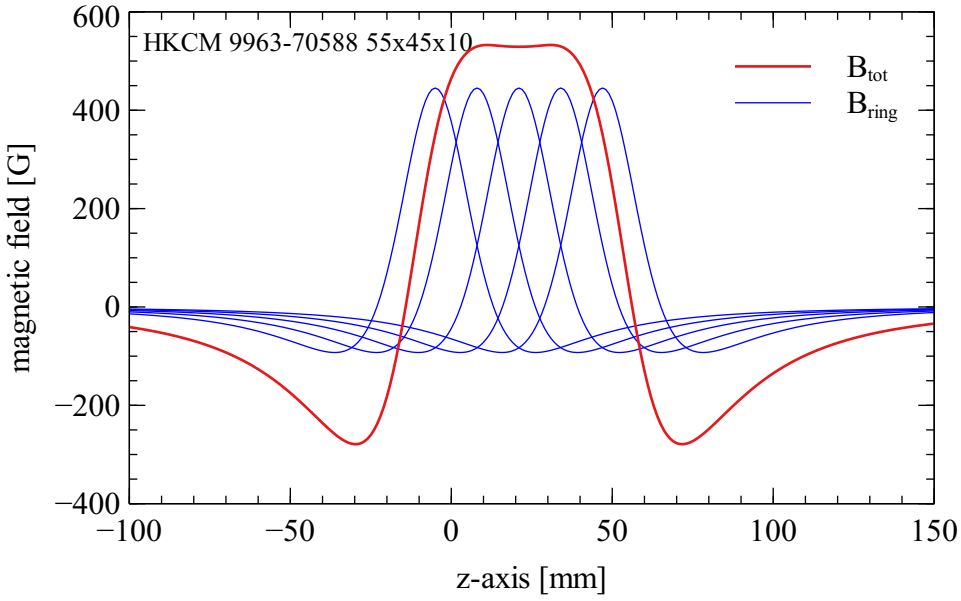

Figure 41: HkCM magnet ring with dimensions $55 \times 45 \times 10$ mm, blue denoting the field lines in the centre for each individual magnet and red being the sum of all magnets combined

5.2.2 Rod magnets

Rod magnets provide the possibility to keep similar magnetic field properties, but allow for easier assembly and disassembly of the system to bake the components at temperatures of 150 to 300 °C. The simulations for the rod magnets are becoming numerically extensive, which is the reason why the finite element software "COMSOL 5.5" is used in order to calculate the field strength and lines. A bunch of different magnets were simulated in order to converge to a applicable solution, with the most promising solution being shown in table 24. The structure housing the permanent magnets is

B_r [T]	$D_{out} \times H$ [mm]	$T_{\max}$ [°C]	$B_{\mathrm{z,max}}$ [G]	n_{mag}	d_{mag} [mm]	Mass [kg]	L_{trap} [mm]
1.17	8×20	120	420	3×8	8	0.18	22

Table 24: Selected permanent rod magnets

3d printed using Fused Depositon Modeling (FDM) with the holes for the magnets drilled to the correct size in a machine shop. This was inspired

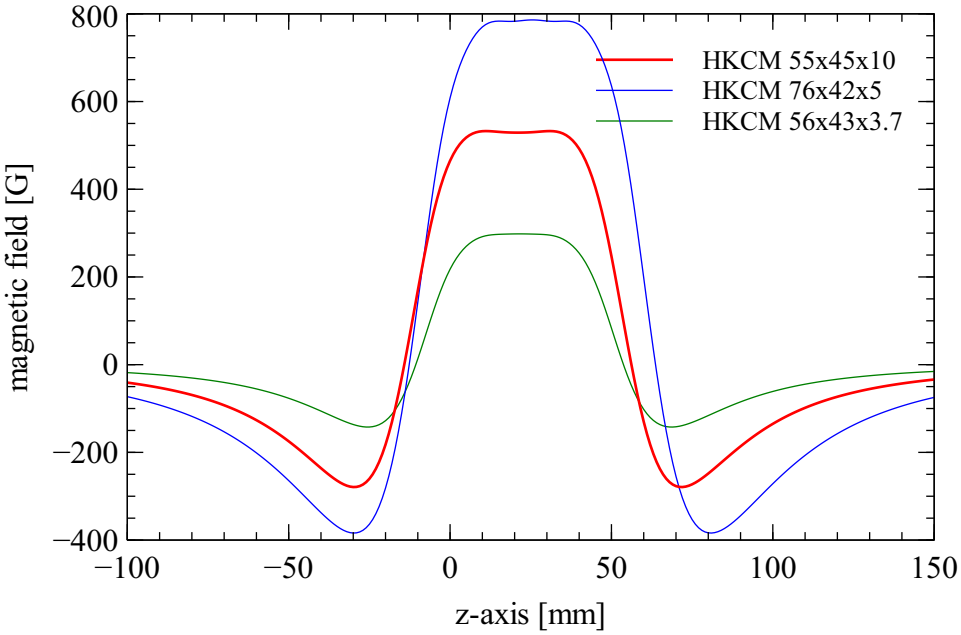

Figure 42: Ring magnet plot comparison

during discussions within the researchers of the group. The magnetic field the permanent rod magnets produce can be found in Figure 43.

5.3 Permanent magnet measurements

In order to validate the simulations performed, the permanent magnet assembly selected was measured. This was done with two different setups and compared in order to confirm initial measurements. The first test setup can be seen in Figure 44a, while a simpler system can be seen in Figure 44b.

The first test setup was able to measure the field in the assumed, homogeneous part, with great precision in translation motion. This data suggested a field misalignment between the sensor axis and the field measurement of 2° with a standard deviation of 0.169°. However, these values need to be considered with great caution due to the fact, that the mounting of the gauss-meter was not very precise, using double sided adhesive tape as well as a plastic holder for the sensor itself. This allows for tilted sensors, leading to measurement inaccuracies.

Due to this, a second measurement was performed using an alternative setup. This setup lacked precision in movement and continuity. However, the alignment was improved in order to minimize the error regard a misaligned sensor. The guiding of the probe was ensured using a 3D printed guiding

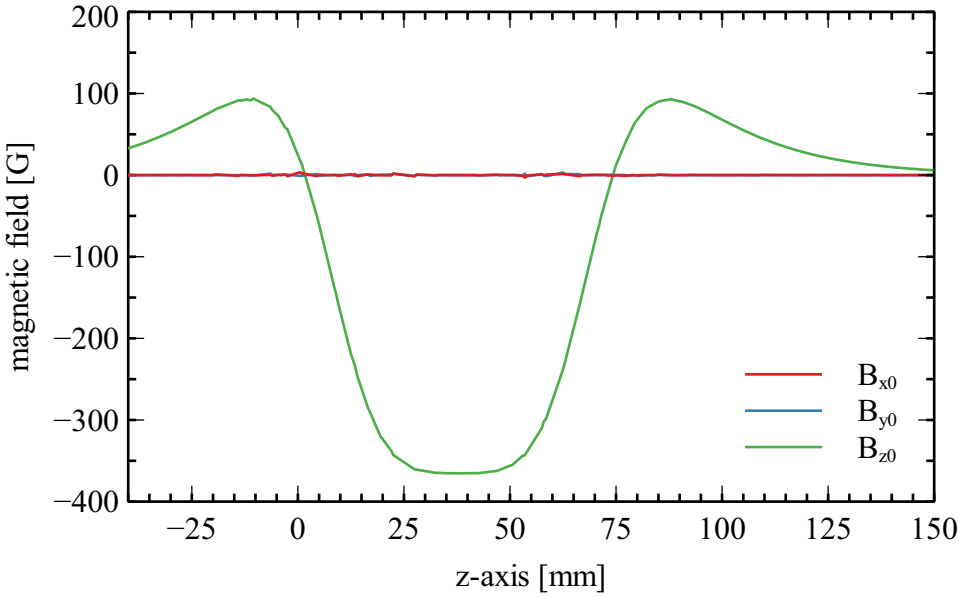

Figure 43: Magnetic field plot of permanent rod magnets at X=Y= 0 mm

jig that is attached to the magnet holder. Through an offset square in the center, the probe can be inserted and half the magnet can be measured with this setup. The field misalignment is greater at the beginning, before it is converging towards the center to an average offset of 4.57° with a standard deviation of 0.44° after half the data points. Before that, the angle is changing drastically due to the field lines converging and not being aligned as they are near the center of the magnet.

The main benefit of the measurements were the ability to tune the simulation. Since the magnetic field created by the permanent magnets in Comsol was grossly overestimated, a correction of the magnetization was implemented to receive the same magnetic field strength for simulations as well as testing. The magnetization can be described by

$$B = \mu_0(M_0 + H) \tag{5.3.1}$$

Together with the datasheet, M_0 assuming $H = 0$ is found to be 955 766 A m^{-1}. With this, the curve can be extrapolated by defining the reduction parameter as

$$M_1 = M_0 \frac{B_{meas}}{B_{sim}} \tag{5.3.2}$$

which in this case is a factor of $M_1 = 752\,967$. This factor yields the magnetic field in z-direction as follows:

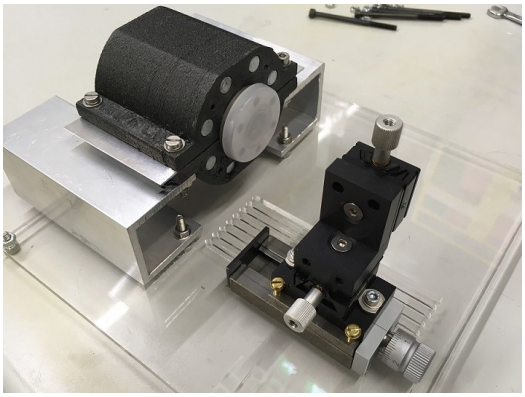

(a)

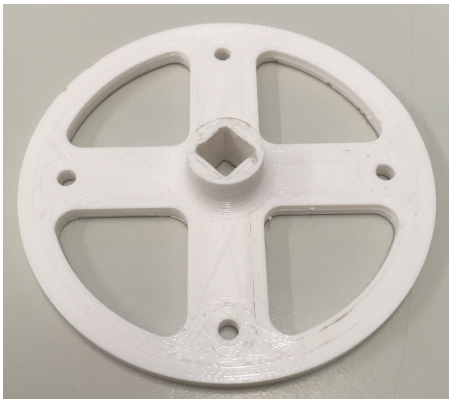

(b)

Figure 44: Magnet measurement setup (a), guiding ring mounted to magnet holder assembly (b))

- Magnet simulation: $B_{z,max} = 365.37\,\mathrm{G}$
- Magnet measurement: $B_{z,max} = 365.91\,\mathrm{G}$

This is a deviation from the simulated value of $0.15\,\%$

5.4 Electrode assembly

The electrodes for axial confinement are a mayor part of the experiment, which is why a multitude of designs were created, evaluated and adapted in order to come up with the best solution. The most critical aspect concerning the electrodes is the size restrictions of a CF16 tube. This yields a building space with 16 mm diameter and a length of 76 mm. The different designs are evaluated in the following section.

5.4.1 Milled ring electrodes

The most common solution for Penning traps is the use of milled electrodes out of metal, often copper or aluminum. These electrodes are usually separated using a isolation material, such as Polyetheretherketon (PEEK) or Macor, a machinable ceramic. Possible designs are shown in Figure 45 and 46.

The mayor design challenge for such an electrode assembly is the size reduction of the experiment chamber due to certain requirements that need to be fulfilled. These include venting holes to avoid entrapped air pockets, electrical access to the electrodes while isolating all the electrodes that shall be connected to ground. Further the assembly needs to be held in place, leaving either the use of the gaskets or threaded rods that need to be insulated again.

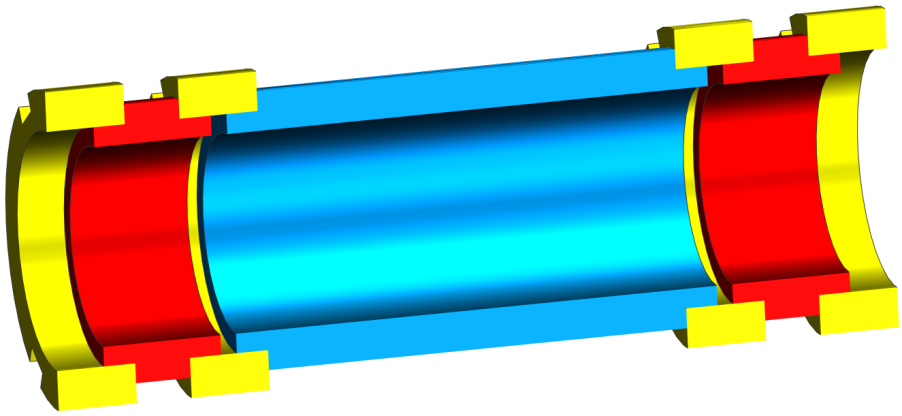

Figure 45: Milled electrode concept, Ground electrodes in blue, switching electrodes in red and insulation in yellow

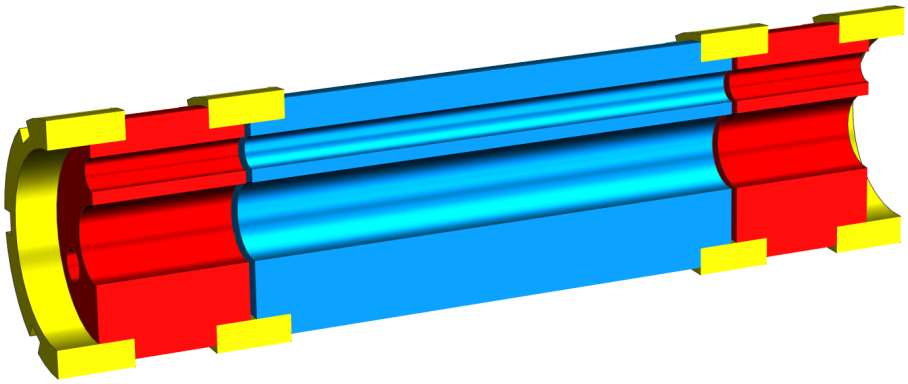

Figure 46: Milled electrode concept alternative, Ground electrodes in blue, switching electrodes in red and insulation in yellow

5.4.2 Metallic substrate on kapton foil

A possibility to generate electrodes is the use of kapton foil with a metallic substrate deposition. This has been previously done at the laboratory as described by Vigo et al. [**Vigo2020**]. After the deposition process, the foil is rolled to form ring electrodes, secured with adhesive described later on. This has a couple of advantages compared to the milled ring electrode design: Firstly, it is of low mass, and therefore generates less force during accelerations in order to retain the system in its desired place. Secondly, the space within the experiment chamber is almost as big as without the electrodes, resulting in the possibility of having a field offset greater 5°.
Before this can be further designed, there needs to be a certain amount of testing performed. This is due to the fact, that the vacuum in the experiments performed by Vigo et al. [**Vigo2020**], the vacuum was kept at a level of 1×10^7 mbar and not tested at UHV or XHV. In order to test if the materials, namely the foil, the substrate and the epoxy to hold everything in place are suitable for the use in UHV, outgassing tests using an Residual Gas Analyzer (RGA) are performed at the laboratory. The RGA is a "Pfeiffer Vacuum Prisma Plus" with the possibility to ionize particles and detecting them in a range from 1 to 100 u. This helps to understand the outgassing behavior of lots of materials. Thereby a minimum of 10 measurement runs are performed which are then used to calculate the mean and standard deviation, since every run brings slightly different values.

In order to compare the data and see the outgassing-changes due to the foils, an initial background measurement is performed, which in this case is the empty chamber with results displayed in Figure 48. To add samples, the turbo-pump has to be shut down, followed by venting the system with N_2

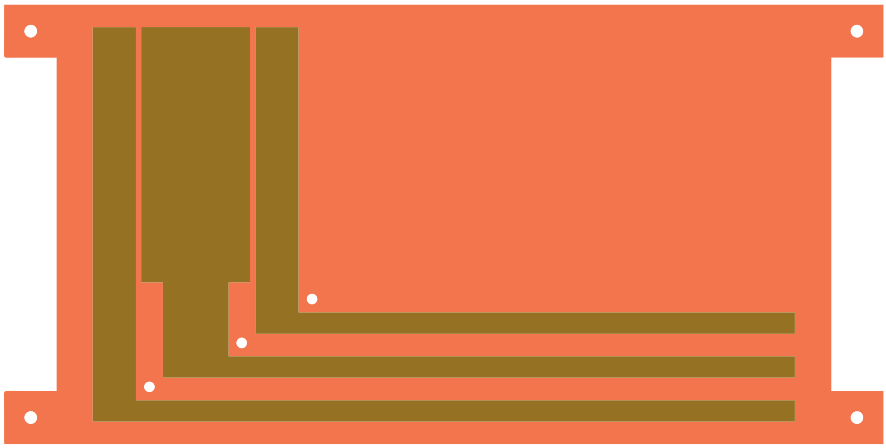

Figure 47: Sketch of metallic deposition (gold) on kapton foil (orange) with the electrode area on the top left and the supply area at the bottom

before opening the CF63 flange in order to exchange samples. The samples are placed inside in the following order:

- Foil with germanium deposition
- Foil with germanium deposition, bonded with "Stycast 1266 Epoxy"

This plot shows the outgassing properties with some of the most common peaks. These are H and H_2 at 1 respectively 2 u, the H_{20} peak at 18 u as well as N_2 at 28 u. The most concern was that the more complex molecules could break up inside, resulting in high detection values between 50 and 100 u. Analyzing both the samples for the foil and the bonded foil it can be seen that there are no mayor molecule structures breaking apart as can be seen in Figure 49. This enables the cropping of data and in subsequent graphs, only the first 50 u are displayed. The high peak of N_2 is due to the flushing of the system with said gas for sample exchange preventing the premature deterioration of the RGA and thereby prolonging maintenance intervals. Initially the nitrogen peak was believed to come from venting for sample exchange. Investigation by another group following these measurements showed a small leak just below the RGA, allowing for ambient air to enter the system, explaining the visible N_2 and O_2 peaks. Another point that was found out is,

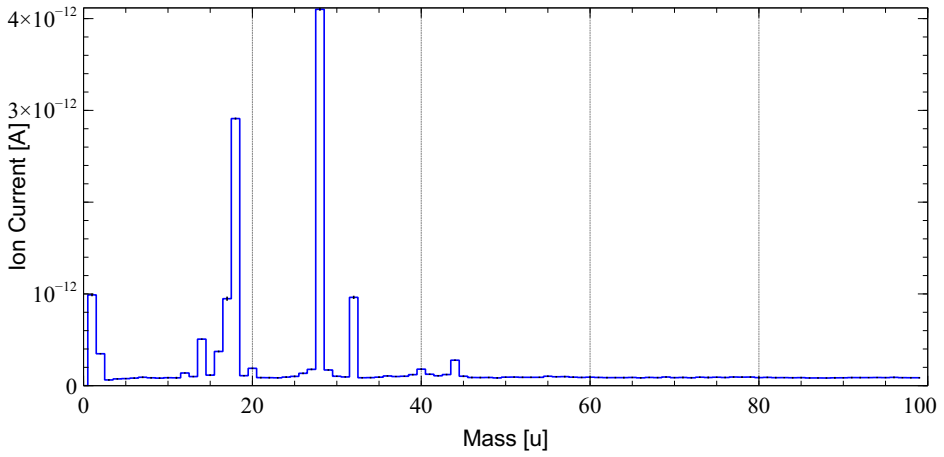

Figure 48: Reference measurement of the empty chamber

that the acetone was outgassing out of the kapton foil once it was inserted. From this point onwards the sample was heated to a certain temperature in order to accelerate the outgassing and measure samples faster. For the deposited foil the temperature selected was 200 °C, the samples including epoxy were limited to 80 °C. Even though this is rated for a temperature of 100 °C this is deemed to be an acceptable margin of safety for discrepancies of the heating system. The effect of the heating process can be seen in figure 50, where the use of heat reduces the outgassing speed of the residual acetone on and inside the sample by a significant amount. [**NIST**] Acetone typically has three outgassing peaks at 15, 43 and 58 u which can clearly be seen in 50. Barely visible at the bottom is the curve after heating the system for 48 h in a brighter shade of red. Heating not only reduces the residuals from acetone greatly, but also helps with the decrease of water as predicted as well.
Now comparing the measurements against each other, we receive the following graphs 51 by subtraction of reference values. If resulting values are below zero, they are set to zero since they are not relevant for the outgassing interpretation of the sample. For the Figures 49 and 51, the reference is the empty chamber, while for the one at the bottom, the foil itself is the reference.
It is important to note, that negative values are set to 0, since the baking is not identical every time, resulting in slightly different values for certain molecules. This reference is mostly the empty chamber, but for comparison reasons also the epoxy was isolated for comparison. It can be seen that the kapton was not heated long enough and lots of gases were still exiting the foil. These outgassing peaks could be removed using thorough heating when analyzing the second graph.

In this case this is either the empty chamber and additionally solely the

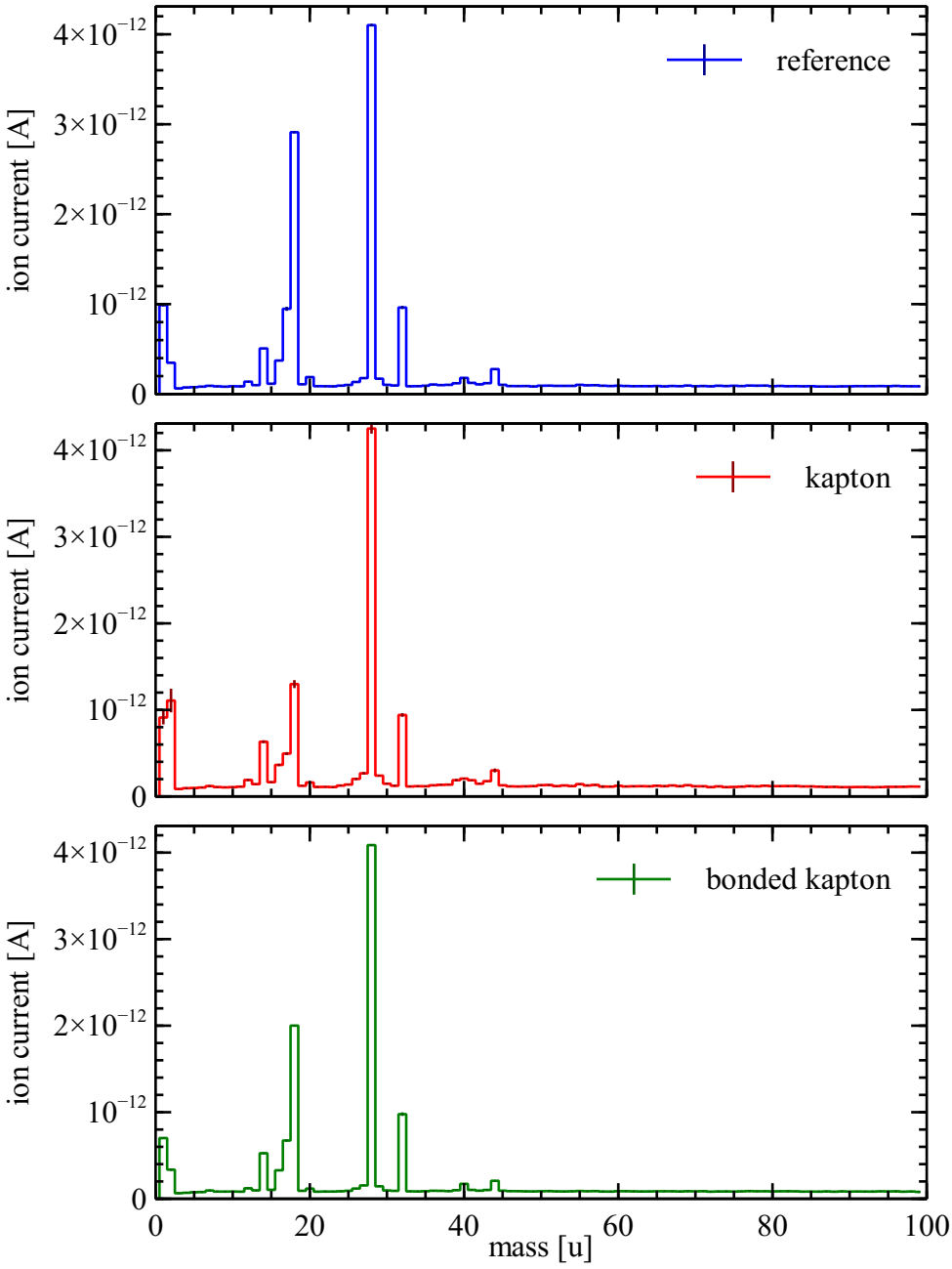

Figure 49: Outgassing measurement for the empty chamber in blue, Kapton foil in red and the bonded foil in green

epoxy in combination with the foil as well as without the foil. It is visible that the foil is outgassing significantly. This due to the fact, that the heating process was concluded prematurely and subsequently the measurement was

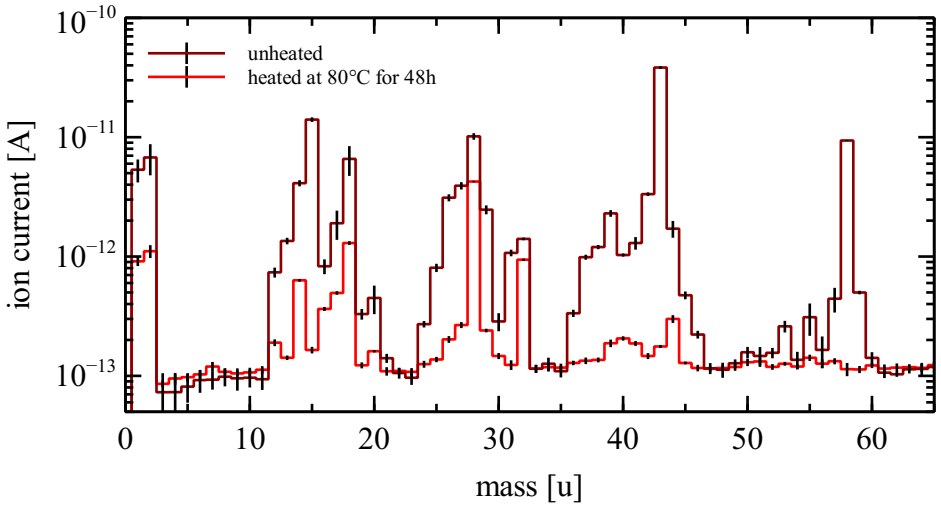

Figure 50: Comparison of the heating influence on the outgassing-properties for bonded kapton foil

taken too early to retrieve converged results. However, if we analyze the other two plots in 51 it is observable, that the molecules are mainly the expected H_2O and O_2.

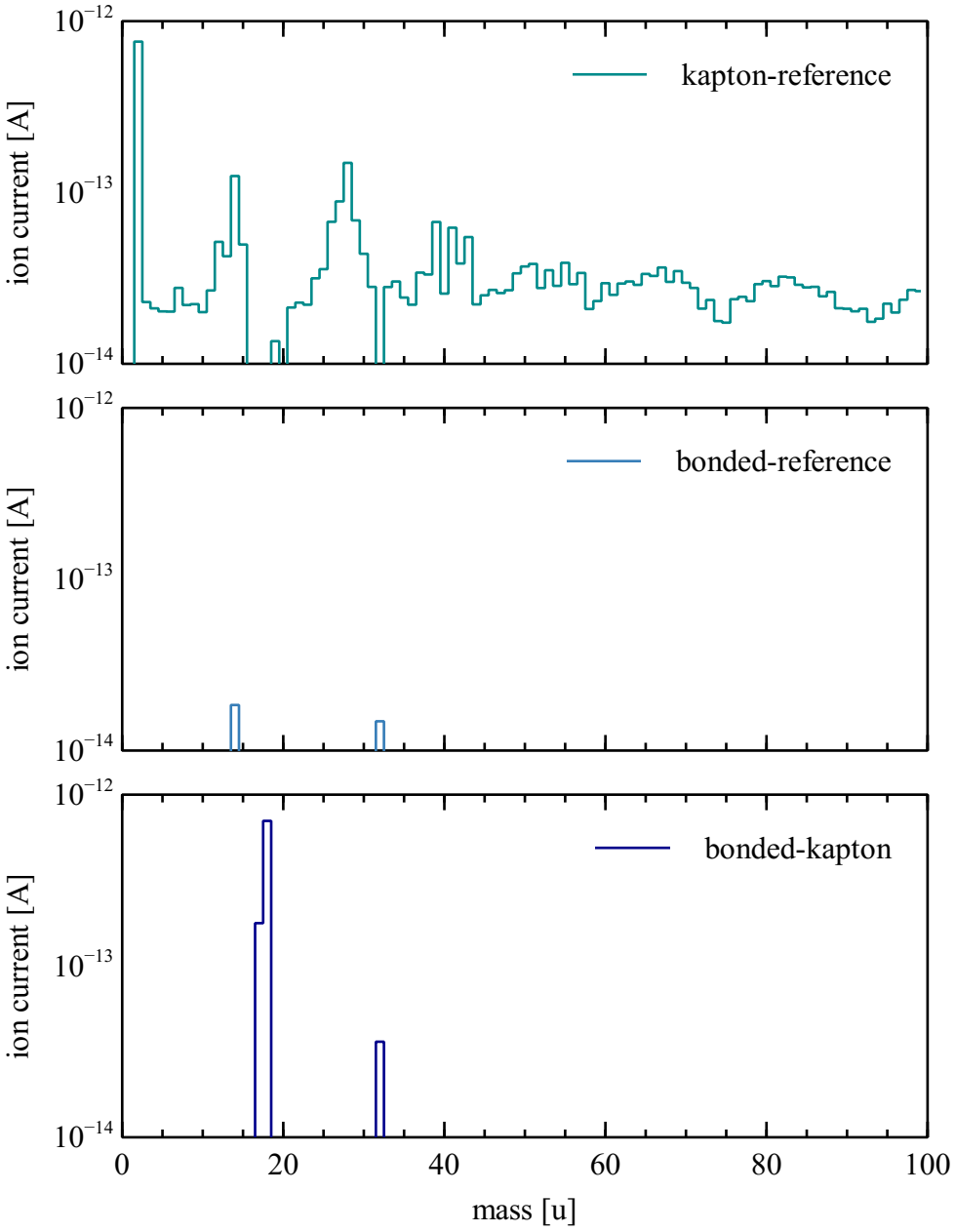

Figure 51: Comparison of outgassing properties

Bonding process

In order to shape the foil as circular as possible, a bonding process is used. Previously, a metallic or plastic cylinder was used to roll the foil on and bond it. For this application, this could potentially result in tolerance issues with the electrode becoming to small or to big. Better would be to bond the foil inside the tube, ensuring the best possible fit. Pressure was applied using a plastic bag and the vacuum chamber. The bag was sealed at atmosphere and placed inside the electrode so it expands when the part is placed in the chamber, removing both air out of the epoxy as well as apply even pressure due to the pressure difference. The material used is "Writgthlon 7400" foil commonly used in composite manufacturing (green-ish), with a heat-weld along the length and sealed off ends using vacuum sealing tape "AT-99" (black) which can be seen in Figure 52.

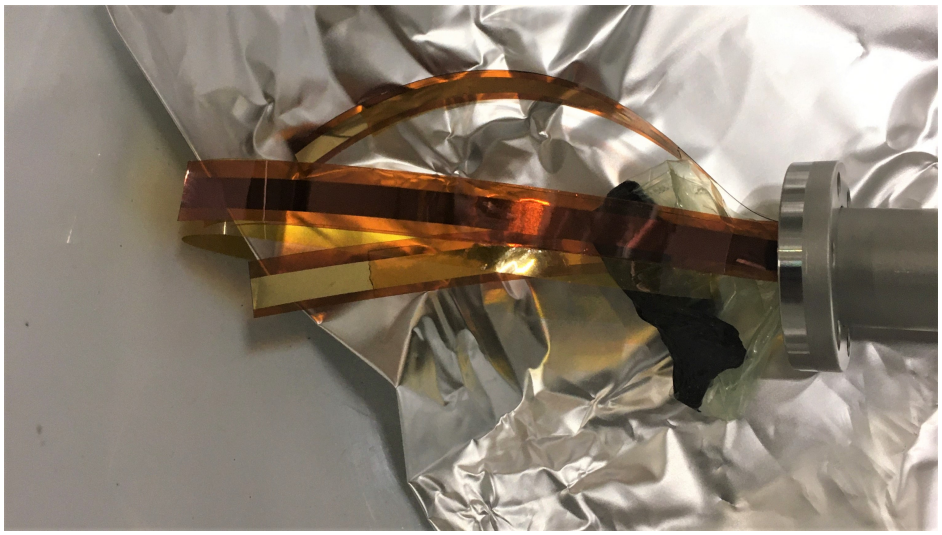

Figure 52: Kapton foil with germanium deposition during bonding with pressure bag (green-ish), foil ends to the three electrodes on the left

The foil is inserted into the tube and a small amount of UHV non-conductive epoxy is applied about 10 mm from the inner edge of the foil. After that, the bag is inserted into the tube and the whole part is placed inside the vacuum chamber for curing for 18 h as suggested by the datasheet.
Once the adhesive is cured, the bag can be extracted as well as the electrode. For flight, the electrode can be bonded to the CF housing using only a tiny droplet of adhesive in order to prevent the part from moving inside the chamber, allowing for the storage of positrons even under flight conditions due to its low mass.

Figure 53: Testing of inflated pressure bag (green-ish) inside an aluminum tube

Connection to feedthrough

In order to supply the electrodes with voltage, a connection between the supply battery and the electrode needs to be ensured. For this an electric feedthrough using a M12 threaded husk was selected. However, the chosen plug proved to be unfavorable for the job, due to it being made out of 8 pieces that needed to be assembled. Together with the ends of the foil being fairly stiff and difficult to handle which can be seen in Figure 52 on the very left. To ensure connection to the outside, a dedicated plug out of PEEK was designed and manufactured to solve these issues.
This plug was then connected to the electrode in multiple steps as suggested during discussions in the lab. First the pins were bonded, before on electrode after the other was attached to the plug on the non-conductive side using a structural epoxy. Once this was done for all electrodes, the electric connection was ensured using a silver paste that after evaporation leaves a silver coating allowing for electrical connection.
This assembly is then attached to the feedthrough and tested using a multimeter and proved to function.

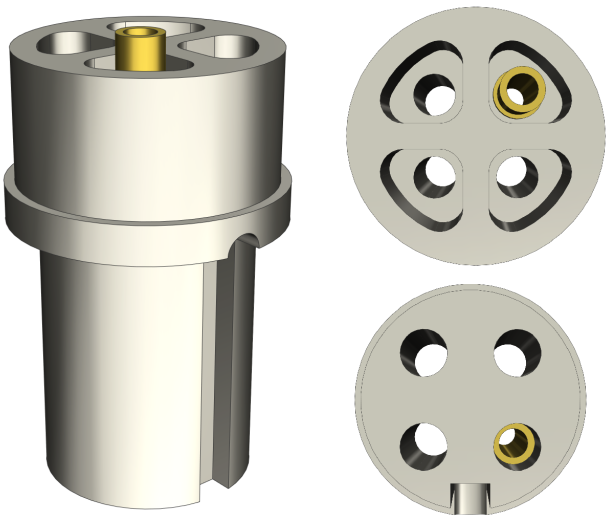

Figure 54: Plug as cad model with pin in gold, left the isometric view, top view from electrode side, bottom view from feedthrough side

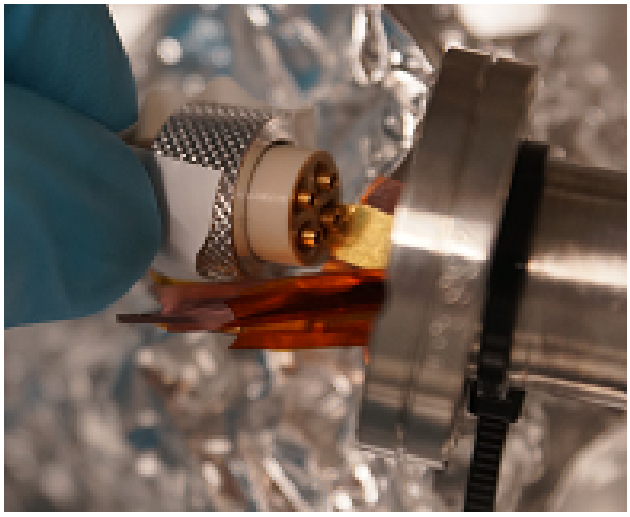

Figure 55: Plug during bonding process of electrode foil ends

5.5 Field misalignment simulation

After analyzing now both the permanent magnets in Section 5.2 as well as the electrodes in Section 5.4, the critically mentioned field misalignment and influence on the particles in Section 2.7.3 is investigated. For this, a simulation was set up using Simion-8.0.8.1. This program is able to simulate particle trajectories over a time, in order to simulate the influence of geometries, parameters and components on particles. The following chapter will introduce the setup of a simulation before displaying the results for misalignment between the magnetic field and the electrodes as described in Section 2.7.3. However, this is still a very idealized situation, not taking any imperfections into account.

5.5.1 Geometry import

The first step is the generation of the simulation file, using an Stereolithographie (STL) file of the geometry to analyze. This geometry is then meshed into small cubes connected at the corners and imported into the software. Important to note is that each part at a specific voltage shall be exported separately, in order to simplify the subsequent setup steps.

5.5.2 Magnetic field creation

The magnetic field is generated using a LUA, a programming language, script to generate a solenoid coil by defining radius, starting and end point as well as the amounts of turns the coils has. This coil was designed in a way to

replicate the field strength the selected permanent magnets create at 365 G as shown in Section 5.2.2.

5.5.3 Simulation setup

In order to see the effect of field misalignment, one single particle needs to be simulated for an extended period of time, allowing to estimate the effects on the particle under idealized conditions. The particle is assumed to have an energy of 6 eV and originate in the trap center. The potential on the electrode is set to 15 V and the magnetic field is created as stated above, with data gathering at the center plane of the ground electrode. In order to receive simulation data for a couple μs, it is run for multiple hours. This limits the possibilities of long term storage simulations of a single positron, both due to run-time issues as well as the amount of data gathered that should then be processed.

5.5.4 Simulation results

The simulations returned the result, that the offset does have an effect on the particle, but does not induce constant drift leading to annihilation. The particle motion stabilizes after about 1.5 ms as can be seen in Figure 56, just below the initial starting energy of the positron.

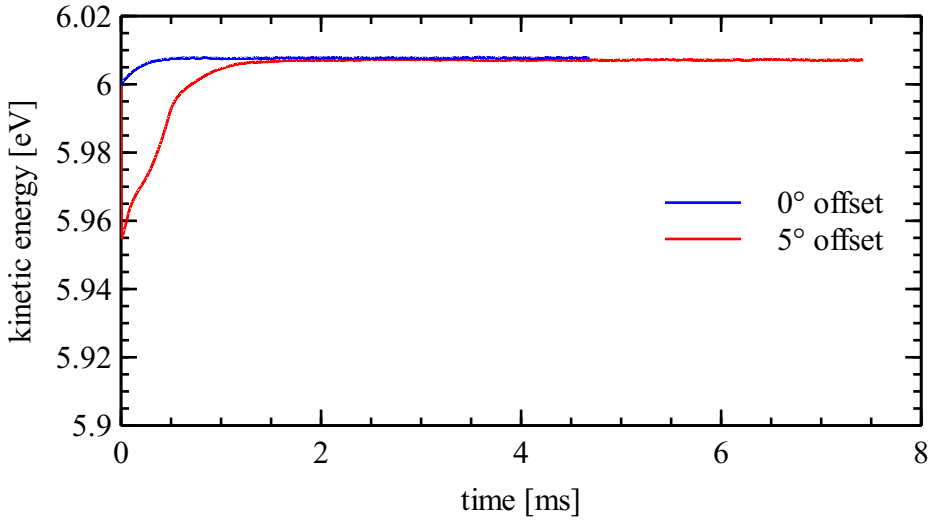

Figure 56: Kinetic energy of a single positron over time

This is due to the change in flight direction, since the particle starts along the main axis and then gets deflected along the magnetic field lines. This

changes the kinetic energy as mentioned, as well as Figure 57. The increased particle oscillation radius around itself is additional prove of this effect.

The difference in oscillation radius is due to the marginally lower kinetic energy. However, long term storage in homogeneous electromagnetic fields does not seem to pose a problem according to these simulations.

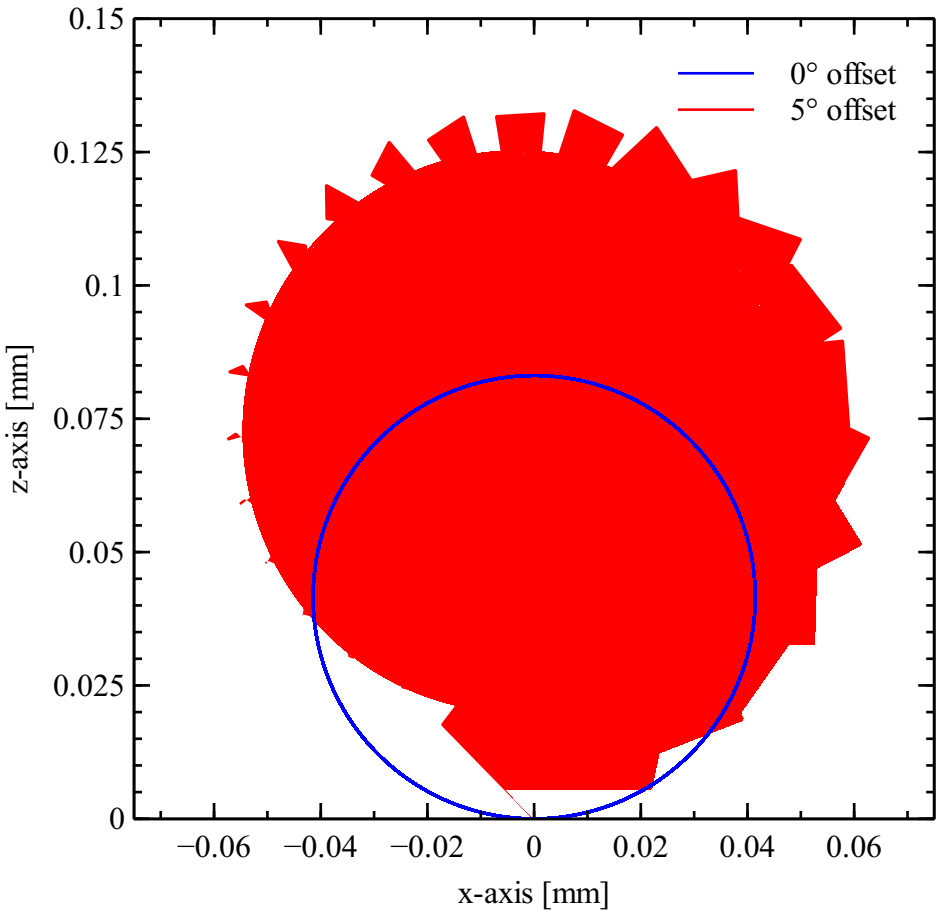

Figure 57: Positron position change in trap center

5.6 Switching electronics

In order to use the electrodes to its full potential, dedicated switching electronics are developed, allowing for optimization in order to reduce the switching times as much as possible, while ensuring the constant voltage supply throughout flight. The design was done with assistance of experts within the laboratory.

5.6.1 Printed Circuit Board

For small sized electronics, a Printed Circuit Board (PCB) has become the most used variation in the recent years. They allow for powerful, small sized components to be designed in a dedicated software and fitted on a small space due to the low footprint of SMD components. For the following tasks described, the software KiCAD was used due to advanced expertise within the laboratory in case troubleshooting is required.

Schematic

The first step is the drawing of a schematic of the electronics, including the components that shall be used. For this, a plugin can be installed, ensuring that downloaded parts are automatically loaded into the part library of KiCAD and can then be placed in the schematic effortless. A couple of design rules help with connecting the different terminals of the components. Exemplary is the use of a dedicated ground and battery numeration in order to reduce length of lines and simplifying the process. Additionally it is important to also add mounting holes.The components are summarized briefly here

Bayonet Neil Concelman (BNC) plugs BNC-Plugs for the input signals are used due to their widespread use in the laboratory, with all signals being transferred via LEMO cables and BNC plugs, simplifying integration in the existing infrastructure.

Dip-Switches To allow for high flexibility, Dip-switches are included in order to allow for every input A or B either supply voltage V_{DD}, Ground (GND) or the signal triggering a process. This enables the possibility of switching up from ground as well as switching down from voltage easily. Attention needs to be payed to first turn off a switch before turning the same one on in order to avoid a short circuit and potential damage to the electronics.

Logic-Input CMOS Quad Driver This component is a four-output CMOS-buffer/MOSFET driver with 1.2A peak drive. Switching times of 100 ns are possible. The selected xx69 variation was chosen due to the fact that one of the inputs for the channels is inverted while the other one is not, allowing for more flexibility during testing. The logic diagram and table can be seen in Table 25, while the whole table is in Appendix A

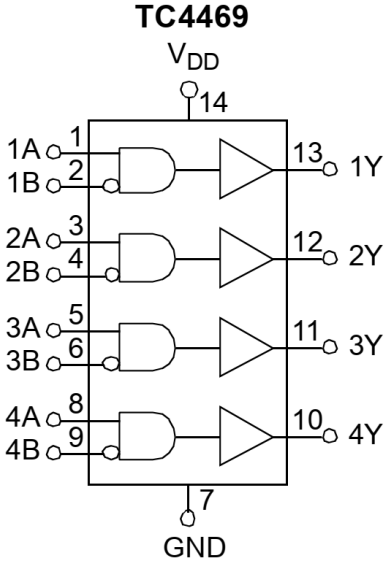

Part No.	TC4469 AND/INV			
Inputs A	H	H	L	L
Inputs B	H	L	H	L
Output	L	H	L	L

Table 25: Logic and truth table of TC4469

Resistance In order to avoid short circuits, a 1 kΩ resistance is integrated just before the switches. This should save the electronics

Capacitors In order to protect the switching electronic, namely the previously described TC4469, capacitors are placed nearby in order to avoid current peaks and destruction of the components.

5.6.2 PCB-Design

The next step then is the location of the part on the physical board. For that, the physical component is imported into a logbok from where they are placed in the defined design space and connected. This is then checked, both by the electric rule checker as well as another person in order to verify a functioning PCB design. From this, the physical PCB can be designed and all the parts put on the board before checking again and ordering with a manufacturer.

5.6.3 Soldering components to PCB

The PCB is cleaned before soldering and the components are aligned in a way to easy grab them with a set of pliers. The soldering starts with the application of a small drop of solder onto a connection. Then the component is placed on the solder drop and heated, in order to fix it in place. Using pliers, the component can be kept in place. Is this done, the other connections are soldered before continuing with the next component. Once the board is finished as seen in Figure 58, it can be checked for proper solder connections using a multi-meter.

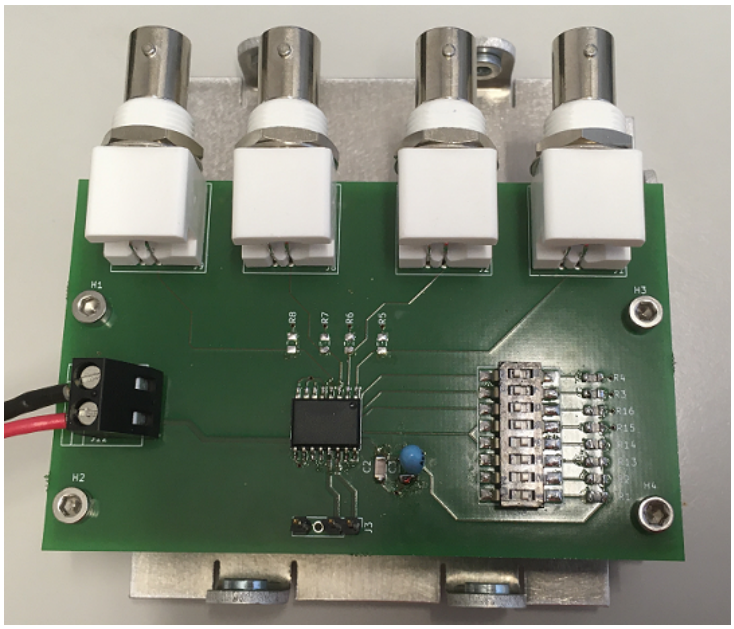

Figure 58: Soldered trigger electronics

5.6.4 Measurements

For the specific board, an oscilloscope can be used in order to verify the switching times that the board is able to deliver as well as the delay that the board itself has in order to correctly time the switching signals.

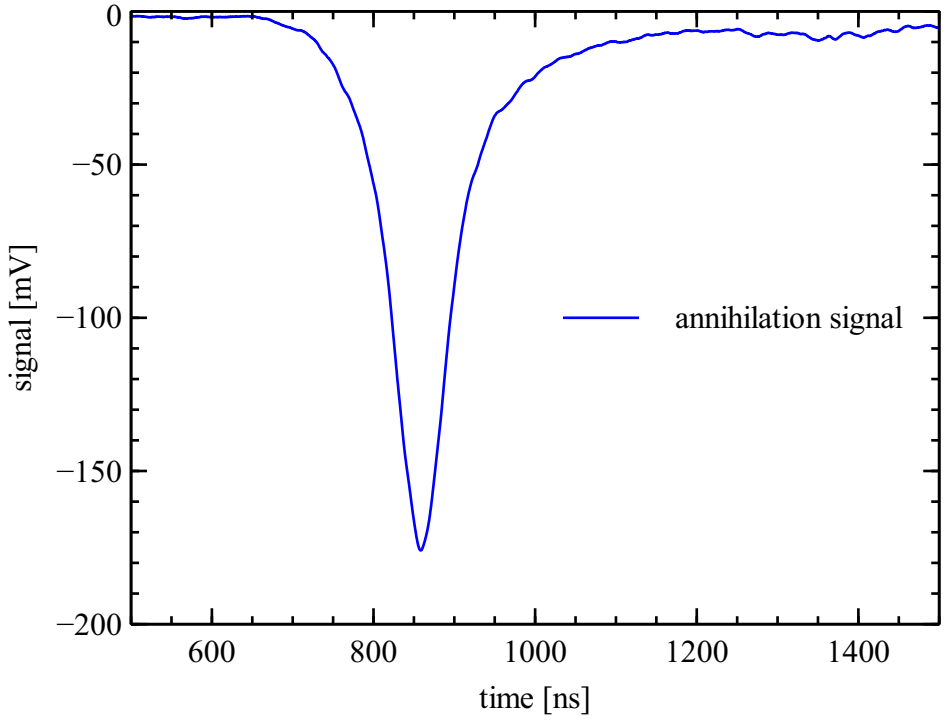

Figure 59: Example of an annihilation signal on an oscilloscope

5.7 Scintillator Counter

In order to register particles inside the trap, a scintillator counter was chosen to be the suitable detector. The principles were discussed in Section 2.11.2. Here the practical realization of the functions as well as the developed design is described.

Having working electronics, PMT as well as part of the surrounding structure already, left the task of designing a part holding the crystal on the PMT glass surface while being light-tight. The simplest and fastest method to hold the fairly big crystal of 230 mm × 25 mm × 25 mm in place was using 3D printing. The design was able to support the conical shape of the crystal, as well as center the PMT inside the housing for improved signal. At the end of the design process there were 3 different parts.

- PMT-centering ring
- Scintillator crystal holder
- Scintillator crystal cap

The parts were then printed on a FDM printer and assembled. A few critical steps had to be ensured, in order to have a successfully functioning detector. The first thing is that the crystal is wrapped in three layers of PTFE foil in order to guide the light towards the photocathode of the PMT. Secondly, a light transmitting optical grease needs to be applied to the glass of the PMT and the crystal. This allows for a reduction in light reflection at the connecting surfaces and improve the efficiency of the detector. Attention needs to be paid to using just a very small amount as well as stop the PTFE wrapping about 3 mm above the bottom, in order to avoid capillary effects between foil and the crystal, potentially sucking the grease up and reduce signal efficiency. Once the holder and crystal is placed on top, the 3D printed structure is wrapped in isolation tape in order to block light from getting into the structure and obstruct the detected signal. Simple test using a blanket while measuring signals was performed and yielded no signal change, proving that the light is sufficiently shielded from the crystal.

(a)

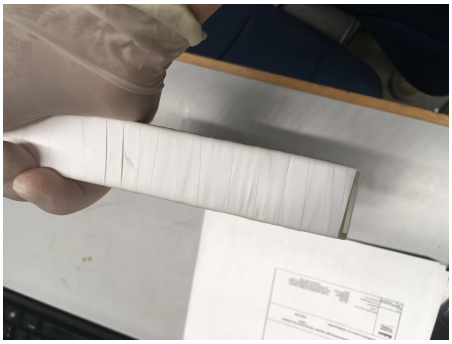

(b)

Figure 60: Magnet measurement setup (a), Crystal wrapped in PTFE tape (b))

Figure 61: Detector about to be finished

6 Results

This chapter will summarize the projects findings. Firstly the setup will be described in detail, before moving on to measurements and tests of subcomponents and subsystems to finally characterise the developed penning trap in detail.

6.1 Experimental setup

The experiment setup consist of four connected sections. The first one is the Buffer gas trap 2.8.1, accumulating and releasing the positrons for measurement. Attached to this is the switchyard, consisting of two coils at 30° angle to each other. This enables two experiments being attached to the same trap and alternate beam time. Following this, a supply coil is attached to continue guiding the positrons towards the next section, separated by a gate valve. To the other side of the gate valve, the experiment is attached. This can be considered the second part, being the supply section where the vacuum is pumped as well as a vacuum monitoring system is attached in order to perform experiments in the developed trap further back. This experiment is connected to the supply section aiming at trapping positrons in a miniaturized trap. The fourth and last part is the electronics ramping the electrodes to the required potential, consisting in part out of the previously described PCB as well as available analog electronics within the laboratory storage. The whole setup can be seen in Figure 62.

6.1.1 Buffergas trap and Switchyard

The positrons are considered as given within this thesis and no in depth look into the existing trap setup is given besides the one shown in Section 2.8.1. The switchyard was initially installed in order to run two experiments in parallel on the same buffergas trap. This is enabled by a coil turned at an angle in order to deflect the incoming positrons by 30°. The deflection was only simulated but not yet tested. This fact makes it an extremely critical component of the experiment and the first focus.

Simulations are performed for different currents as well as locations of the available coils at a positron energy of 7 eV. They showed a high sensitivity to the coil angle, leading to losses of positron transmission if the angle is changed by 2°. In order to compensate for this change, the coil needs to be moved 15 mm in the axial direction. The positron path of the simulated switchyard can be seen in Figure 63 with the starting point of positrons at the bottom right.

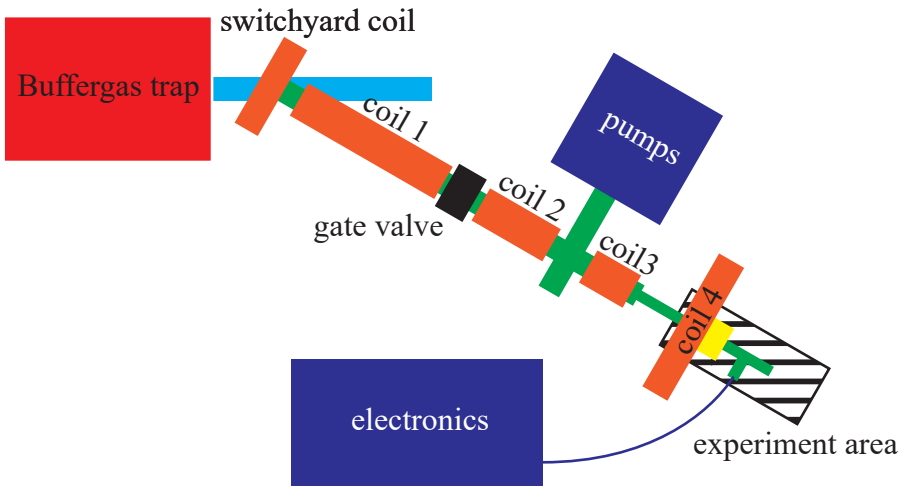

Figure 62: Schematic of the experiment setup

The coil was therefore secured using a angled 3D printed part, preventing rotation while allowing movement in all axes via translation. The simulated data was taken as a first placement, both for angle and distance from the switchyard component, allowing for subsequent tuning.

Once the structural setup to support the supply section and experiment was installed, the scintillator detector was placed centered behind the gate valve as can be seen in Figure 64. The measurements were monitored on the oscilloscope while adjusting location and current of the two coils in order to maximise the signal. Thereby it was noticed, that another small coil shall be used, since positrons were deflected before turning. This coil improves the signal by avoiding the annihilation peak at the beginning of the 30° turn.

6.1.2 Supply Section

Once it was confirmed, that the positrons impact on the valve, the supply section was attached. It consists of a CF40 extension tube and a CF40 cross. To the cross the vacuum gauge and connection to the turbo pump are attached while to the last port a CF40 to CF16 reducer is added as well as an inline valve for venting. Over the extension tube, a coil was attached to

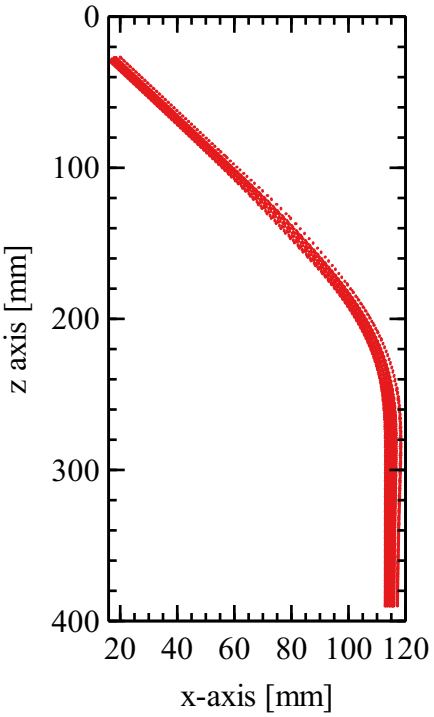

Figure 63: Plot of positron path form above of the switchyard simulation

guide the positrons further into the cross. Once the gate valve was opened, the positron signal was maximized using two pairs of steering coils, offsetting the positrons to the center in order to fit them into the reducer.
Each pair is attached to the supply coil opposite of each other, with the magnetic field direction aligned. This allows for an offset of the positrons along the axis, and with the two coil pairs an offset in all directions by current direction and strength. To tune the direction and field of the steering coils, the scintillator was placed just at the reducer and the parameters for the steering coils were adjusted to remove as much signal as possible. Once this was achieved, the scintillator was moved further away to find the new annihilation point.

6.2 Experiment setup

¨ The experiment setup can be seen in Figure 66. It can be separated into 4 connected systems that will be described in the following.

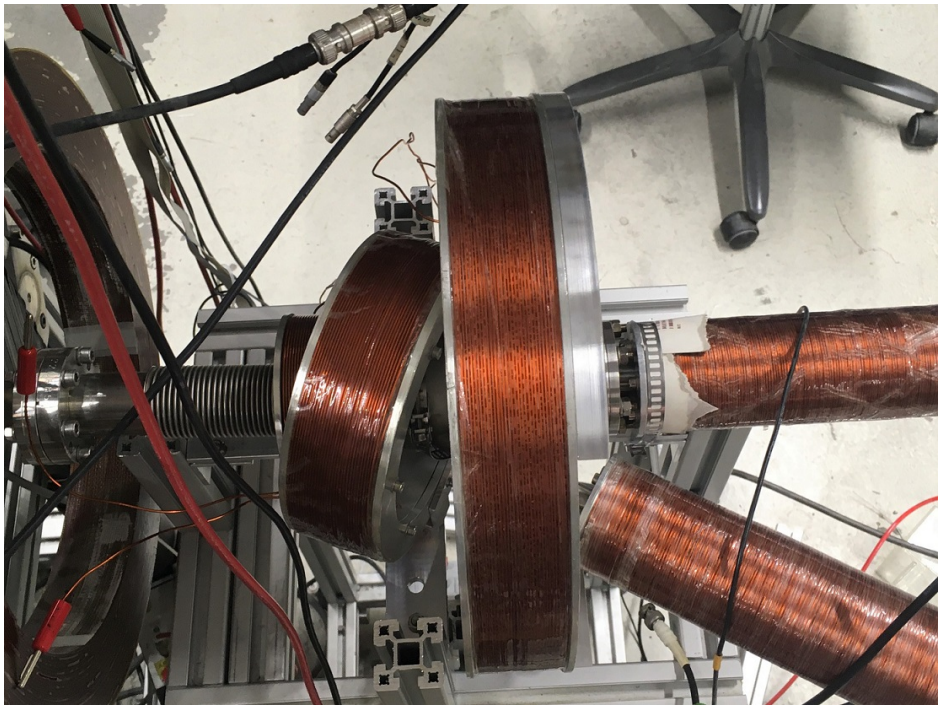

Figure 64: Switchyard coil setup, positrons entering from the left

Support structure The support structure is the skeleton of the AntiCube experiment, connecting every subsystem to a whole. At the bottom it is fixed to the bulkhead using 4 M5 screws attached to the rods. Attached to the rods are the bridges mentioned in Section 4.2.2, which in turn hold the split plates evaluated in Section 4.3.4. They are directly connected to the flange at the T-piece with the bridges attaching to the rods on the outside. A second plate is used in order to guide the assembly and restrict the possibilities of movement in only one direction at the NEG housing with a similar plate. On the outside, the structure will be covered from dust and particles using 8 carbon fiber plates that are screwed to the rods. Additionally, they provide more stiffness, improving strength, and therefore the safety margin of the setup.

Vacuum system The vacuum system is the heart of the experiment. It houses the area where the positrons are trapped and stored. It consist of a CF16 tube (dark blue) to which a copper crimp-off (yellow) is attached, enabling the removal of the trap from the beam line.
On the other side a CF16 T-piece is attached, enabling the connection to the electrodes inside the experimental chamber as well as a connection to the

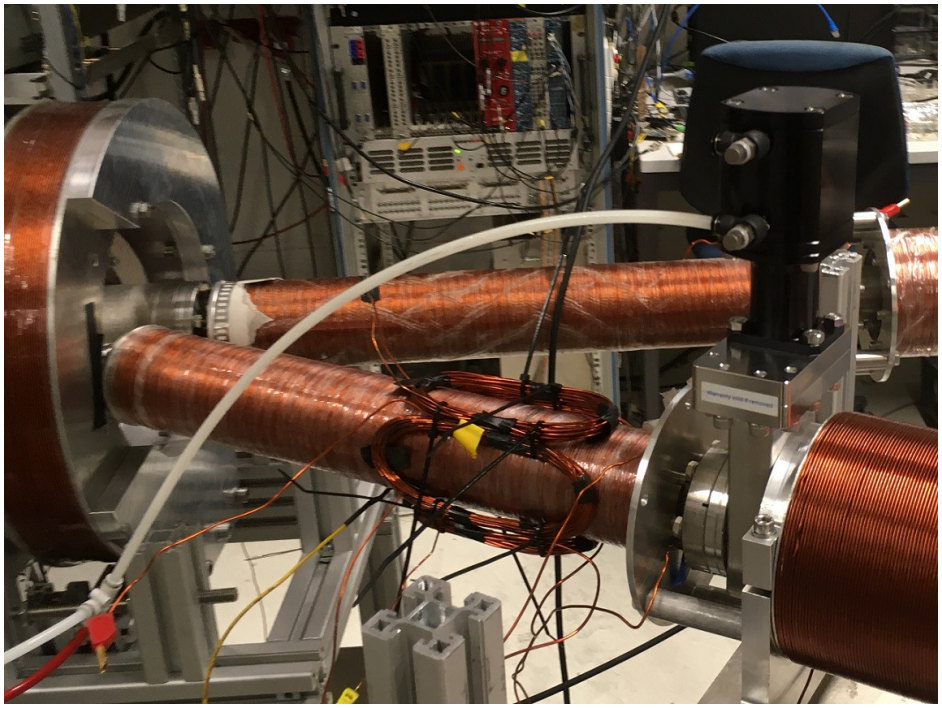

Figure 65: Steering coils just before the gate valve

pumping area. The pumping area consist of a NEG pump (orange) inside a housing and an adapter flange, connecting the CF40 pumping components to the CF16 while accounting for the offset of the parts.

Magnetic structure As the previous analysis showed, rod magnets seem to be the best components for the creation of the magnetic field, due to no required power in comparison to coils as well as simple assembly and disassembly even if the system is fully assembled, allowing for more flexibility. A 3D Fused Depositon Modeling (FDM) printed case was designed and manufactured to house the magnet. It consist of 2 halves separated by 1 mm aluminum plates to ensure a homogeneous field inside the trap. It is further connected to the split plates using M3 screws to be kept in place, while the magnets are retained using half-discs.

Electrodes and electronics The electronics are powered by four 18650 Lithium-Ion batteries. Lithium-Ion was chosen due to their reduces fire hazard in comparison to Lithium-Polymer batteries as well as the general recommendation by NASA "Guidelines on Lithium-ion Battery Use in Space Applications" [**NASABatteries**] to use these types of batteries. They power

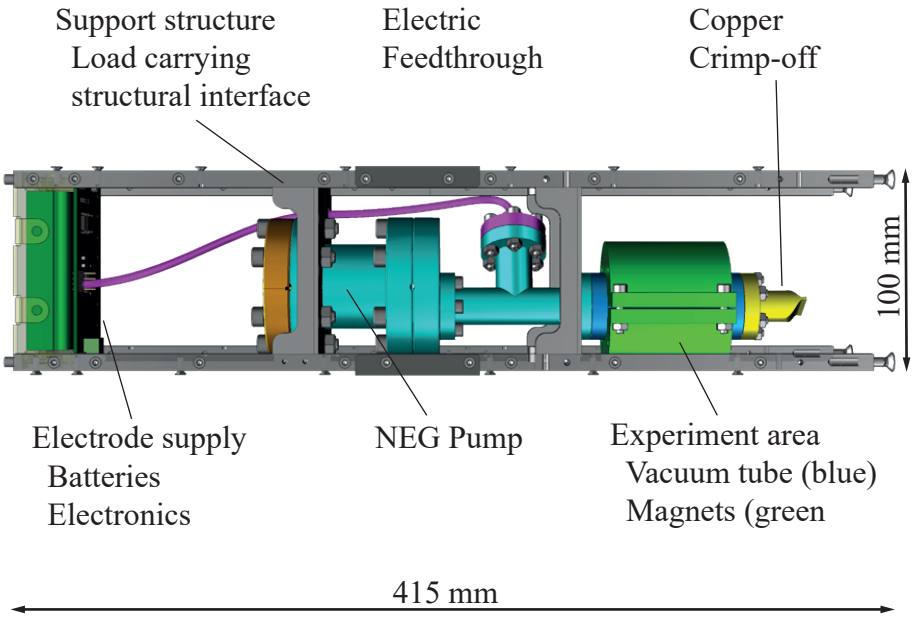

Figure 66: Description of the experiment setup

both the electronics on the PCB needed for switching during the loading procedures, as well as during flight supply the electrodes with the voltage of 14.4 V.

6.2.1 Test setup

The global pandemic in spring of 2020 lead to necessary changes and adaption of the experiment. This was done in order to accelerate testing once working in the laboratory could be continued. Therefore the setup was chosen to be simplified, meaning not to attach the NEG-pump and replacing it with a venting valve. This allowed for troubleshooting in case the experiments encounter issues. The setup can be seen in Figure 68.

6.3 Magnetic field and loading simulations

Using Comsol, a simulation of the overall setup was performed, calculating the magnetic field and subsequently trying to simulate the loading process.

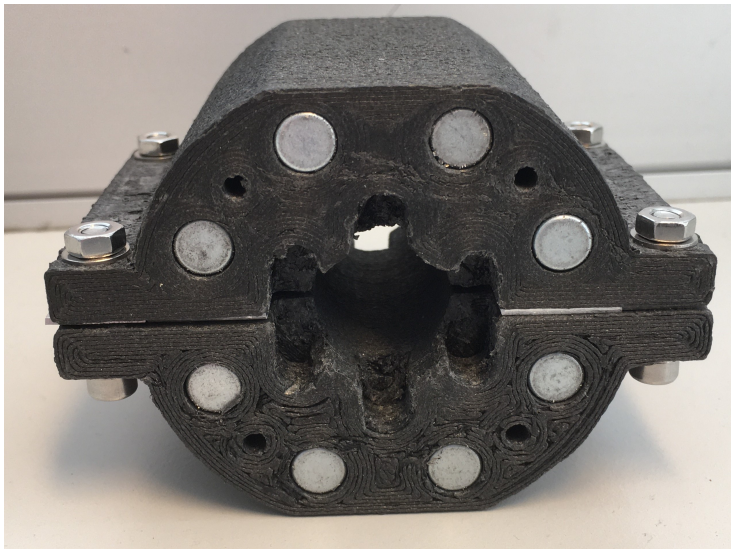

Figure 67: Assembled 3d printed magnet holder

6.3.1 Magnetic field simulation

The magnetic field was calculated using the parameters in Table26.

Number	d_{coil}	l_{coil}	N_{coil}
1	38 mm	415 mm	550
2	120 mm	148 mm	230
3	120 mm	67 mm	150
4	248 mm	58 mm	1070

Table 26: Frame design - Component maximum stress

These coils were centered with respect to the vacuum system using 3D printed segmented rings. These were fixed to the flange before the coils were mounted, aligning the magnetic field lines with the vacuum components. A picture of these rings can be seen in Figure 69.

All these inputs, together with the measured distances between the coils, the magnetic field could be simulated being with the result being displayed in Figure 70. The x and y components are left away in this plot because they are 0 G with only minor discrepancy below 10 G.

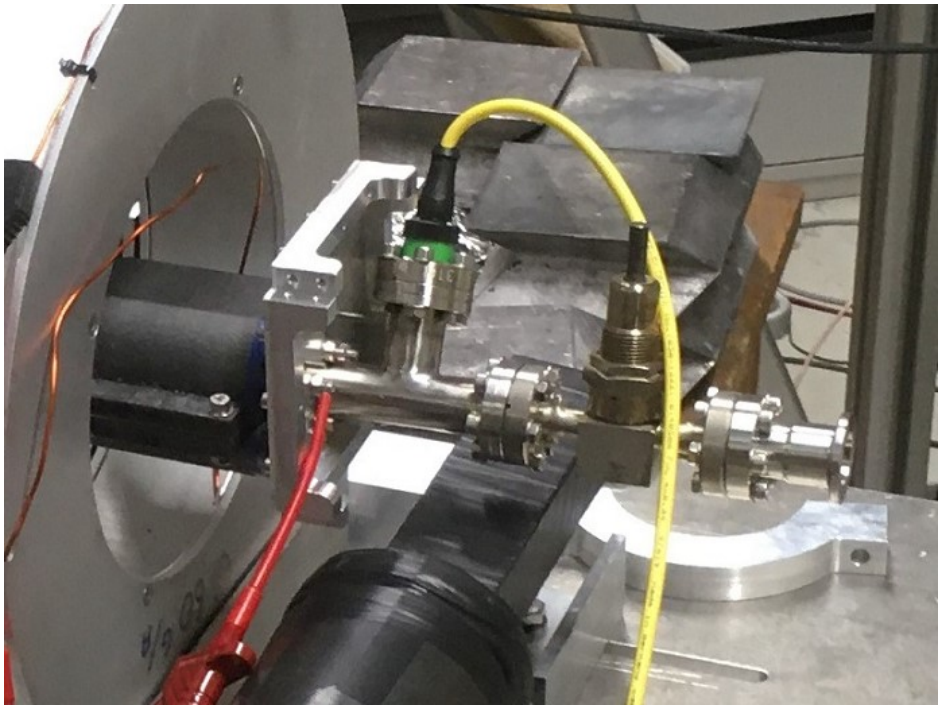

Figure 68: Test-setup attached to the supply section, trap under the black magnet holder, electrode supply cable in yellow

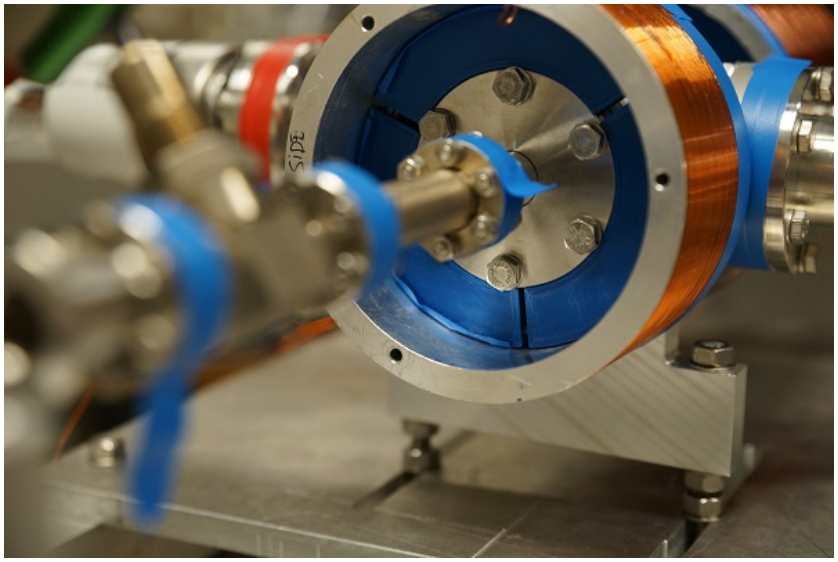

Figure 69: Coil alignment using 3D printed segmented rings (blue around flange) for the coils

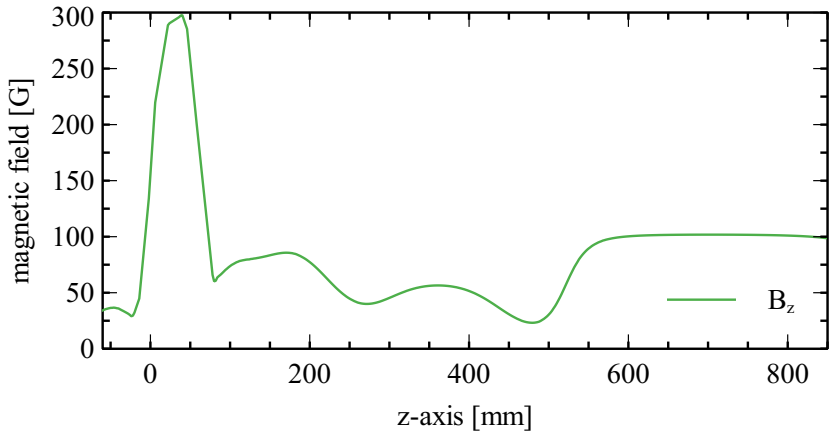

Figure 70: Simulated magnetic field for positron loading procedure

6.4 Leak detection

An important part of vacuum technology is checking the assembled parts for leaks. This allows to find scientists and engineers faulty connections between components and determine the exact leak location. [**HandbookVacuumtech16**]

To perform a quick leak check, a drop of cleaning alcohol can be used while monitoring the pressure measurement. If there is a leak, the alcohol will evaporate in the vacuum chamber, leading to an increase in pressure which can be seen. Often times however, the leak is very small and can not be found with this method.

In that case, a leak detector is needed. That is attached to the outlet of a pump and contains a mass spectrometer for a certain, rare atmospheric gas such as He. If this gas is now brought close to a flange, an increase in particles is detected by the spectrometer if there is a leak. The connections can be checked one by one using electrical tape that seals it off in order to only check one connection after another.

This method showed that one extension piece as well as one of the chosen venting valves were faulty and had to be replaced by functioning ones.

6.5 Signal management

In order to time the switching, a signal needs to be sent to the electronics and trigger a change in voltage. This digital trigger signal is provided by the electronic an time-wise proportional to the signal releasing the accumulated positrons. The Transistor–Transistor Logic (TTL) trigger signal has to be timed correctly in order to switch the electrodes when required. This timing is done by delays. Practically it is realized adding or removing wires of different length in order to shift the signal ns regime. The rough adjustment is done by adding long wires, while fine tuning is done by dedicated boxes that at a press of a button ad 32, 16, 8, 4, 2, 1, 0.25 or 0.125 ns of delay.

For the electronics setup, the first step is to find the time delay between the trigger signal and the positron ensemble. This is done by increasing the delay until all the positrons are rejected at the first electrode. This is recognizable by the disappearing signal on the oscilloscope. To confirm, the scintillator can be moved to find the new annihilation point on the setup.

The first setup is done by tuning the delay, until the measurement on the scope disappears. With this the timing of the pulse can be estimated for the following adjustments. Rewiring the trigger signals using D-Triggers, adding delay to the first electrode as well as allowing for signal width adjustment, the experiments could be advanced in order to improve characterization of the trap.

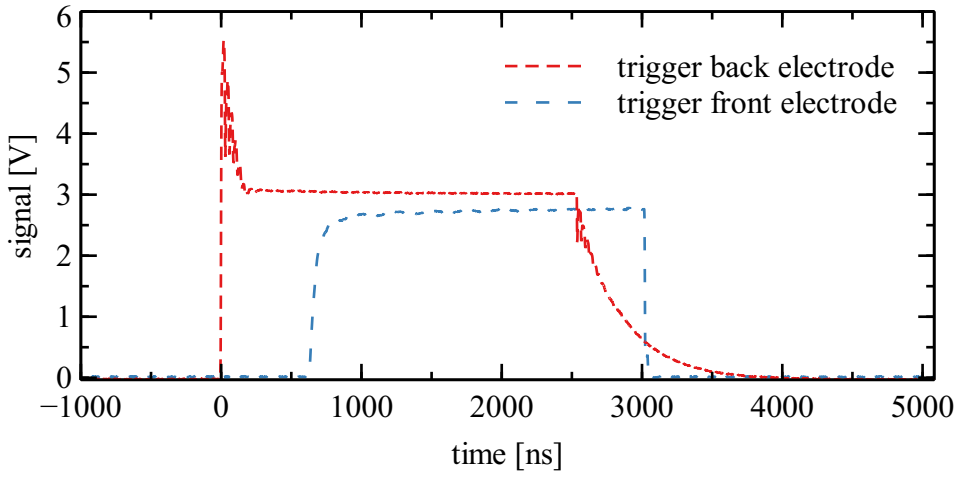

Figure 71: Example of trigger signals for a measurement

6.6 Energy spread

Energy spread with sequential ramping of first electrode. Resulting is a mean energy of the positrons of 10.44 eV with a spread of ±1.22 eV. The plotted data can be seen in Figure 72. These values are slightly above the estimated 7 eV, however they are still within a reasonable range. The difference is most likely due to energy change during transport due to the switchyard as well as the changing magnetic fields.

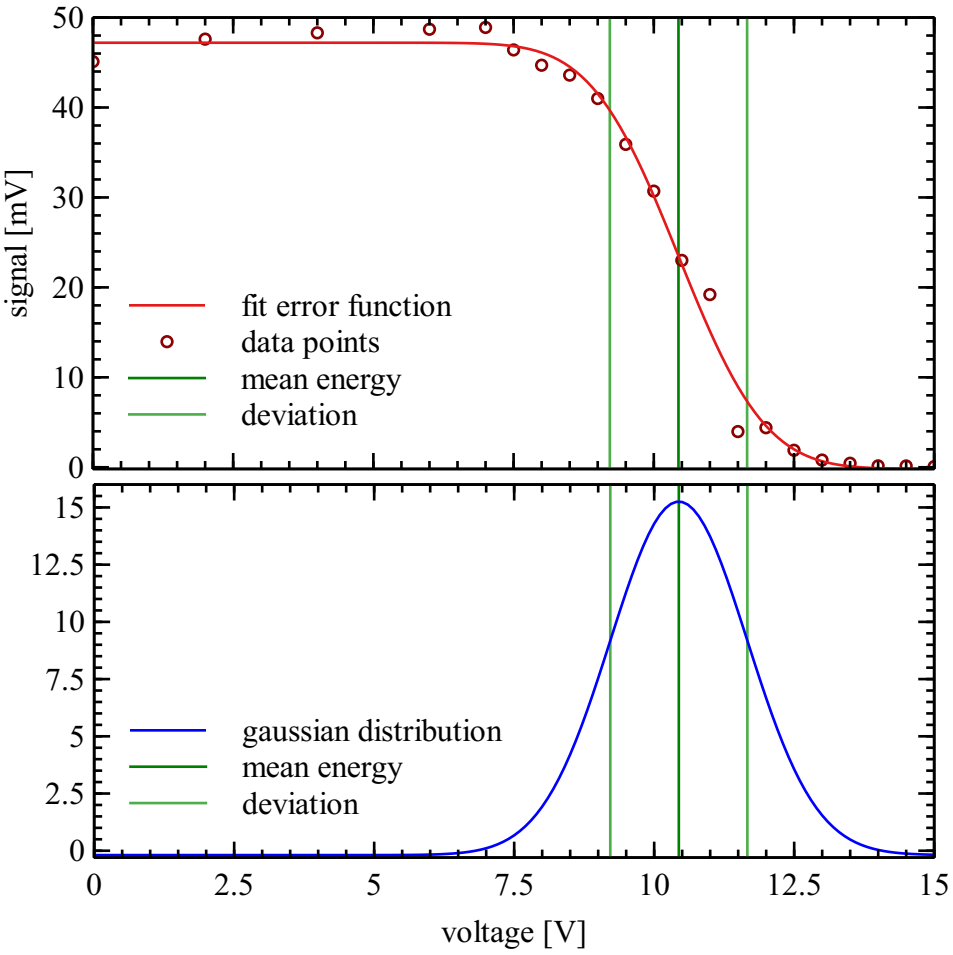

Figure 72: Energy spread of positrons at the experiment area

6.7 Trapping measurements

The actual trapping measurements were performed using the setup described in this chapter. The fact that the annihilation stems from positron annihilation and not another source was shown by measuring the system with a shut gate valve. This measurement therefore serves as the background measurement.
The next step is the measurement of a signal with all electrodes set to ground. This measurement is the brown curve can be seen as the brown curve in Figure 74.

Taking this as a starting point, the wiring was adjusted in order to fix the trigger delay between the first and third electrode, while adjusting the width of the trigger signal. With this approach, it could be shown, that positrons are stored up to 3 µs as visible in Figure 74.

The measurements were preformed at three different time steps from 1 to 3 µs in steps of 1 µs. The signal strength seemed to be in the same region as shown. However, this can not be quantified due to issues during the measurement process. The signal saturated the oscilloscope display limits, which lead to a loss of data. This can be seen in Figure 75

The trapping of positrons is clearly demonstrated, but the amount can not be quantified with the recorded data. An attempt was made to evaluate the trapping efficiency by analyzing only the good data. This meant, to crop to a range between -15 and -45 mV. This approach yields the result in Figure 76. However, great uncertainty is attached in this comparison, due to the fact, that the data is unreliable. Additionally, longer trapping in the ms regime could not be performed due to the proof-of-concept equipment used.

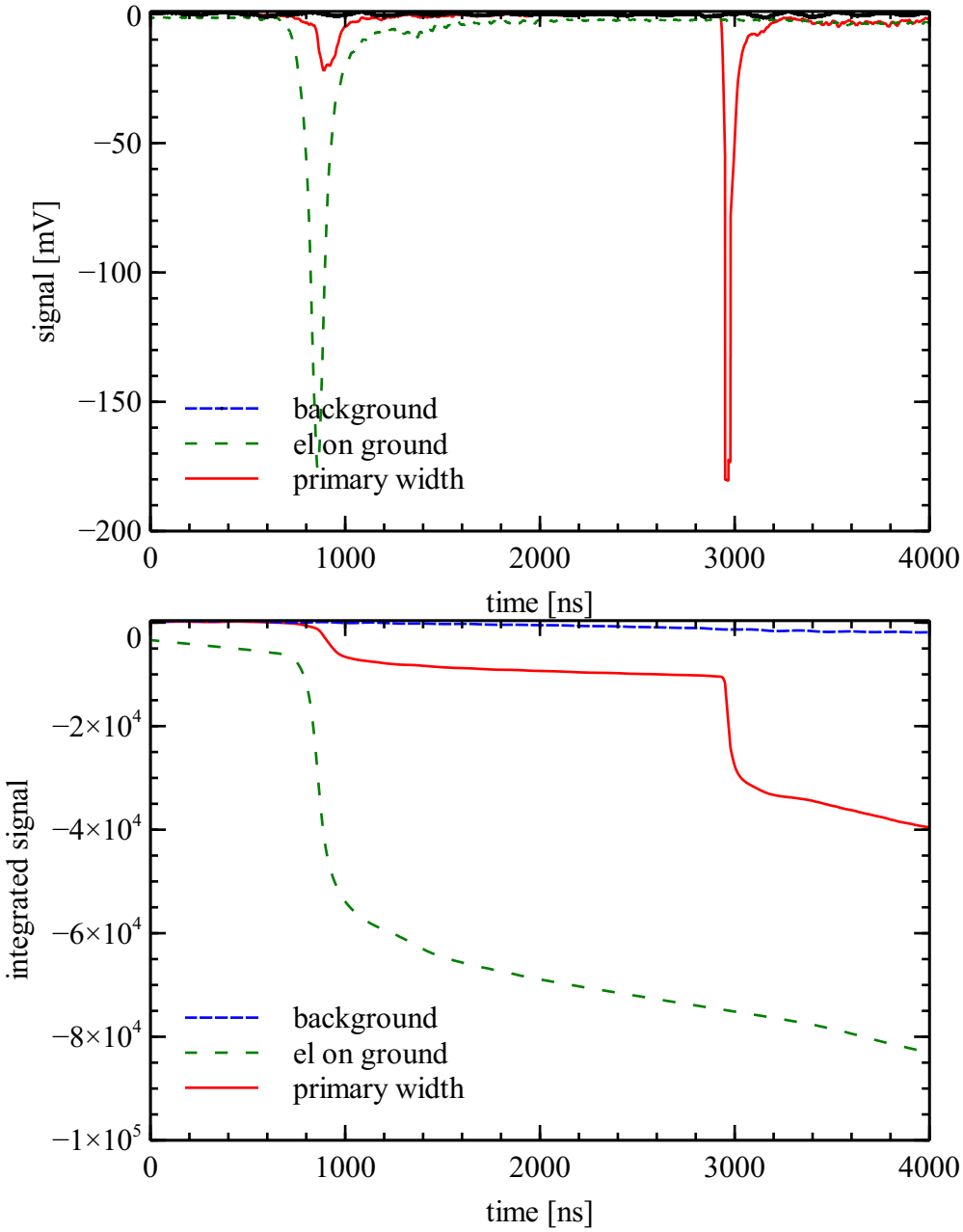

Figure 73: Reference annihilation signals at the trap, background barely visible at the top (thick line)

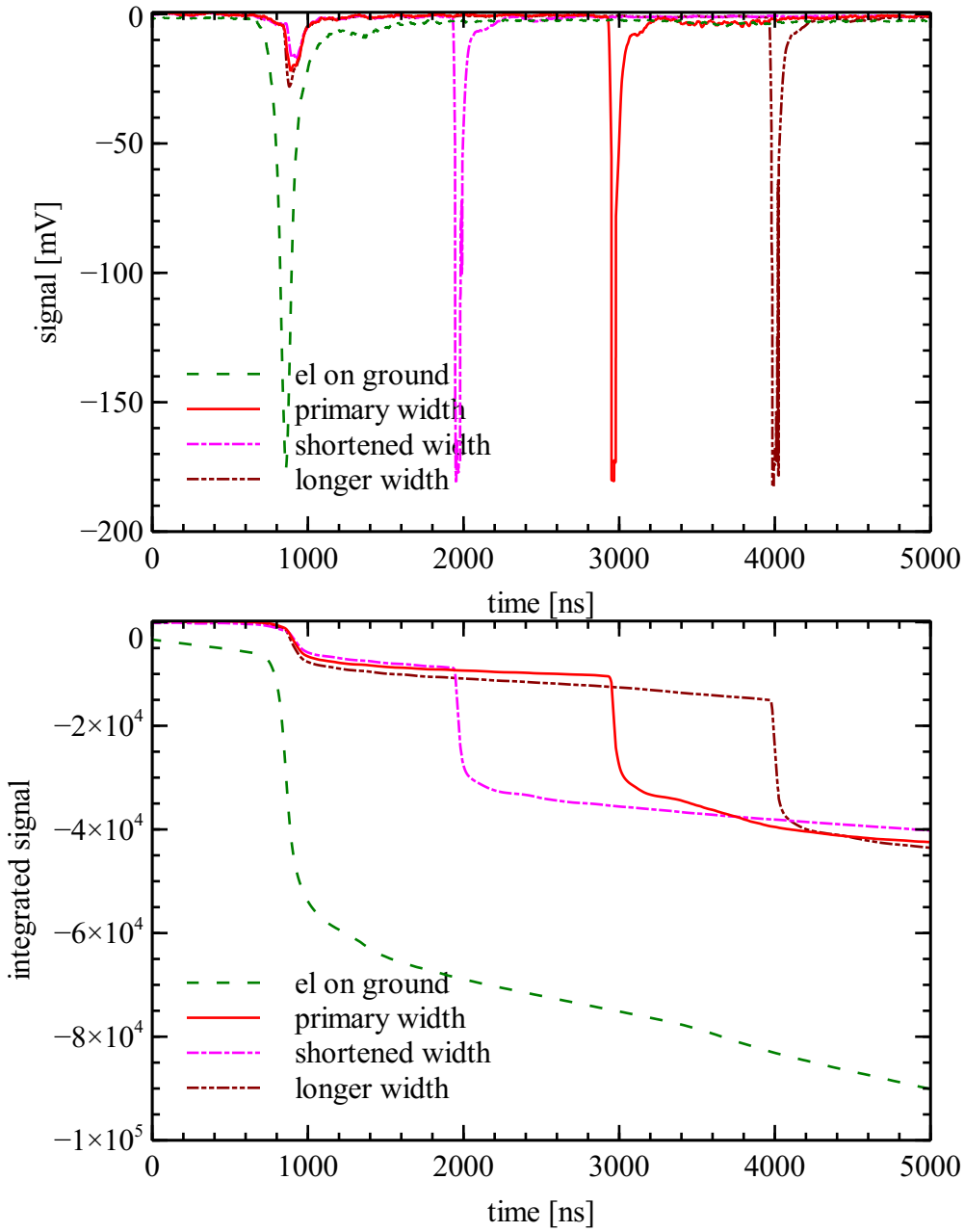

Figure 74: Annihilation signal for different trapping duration

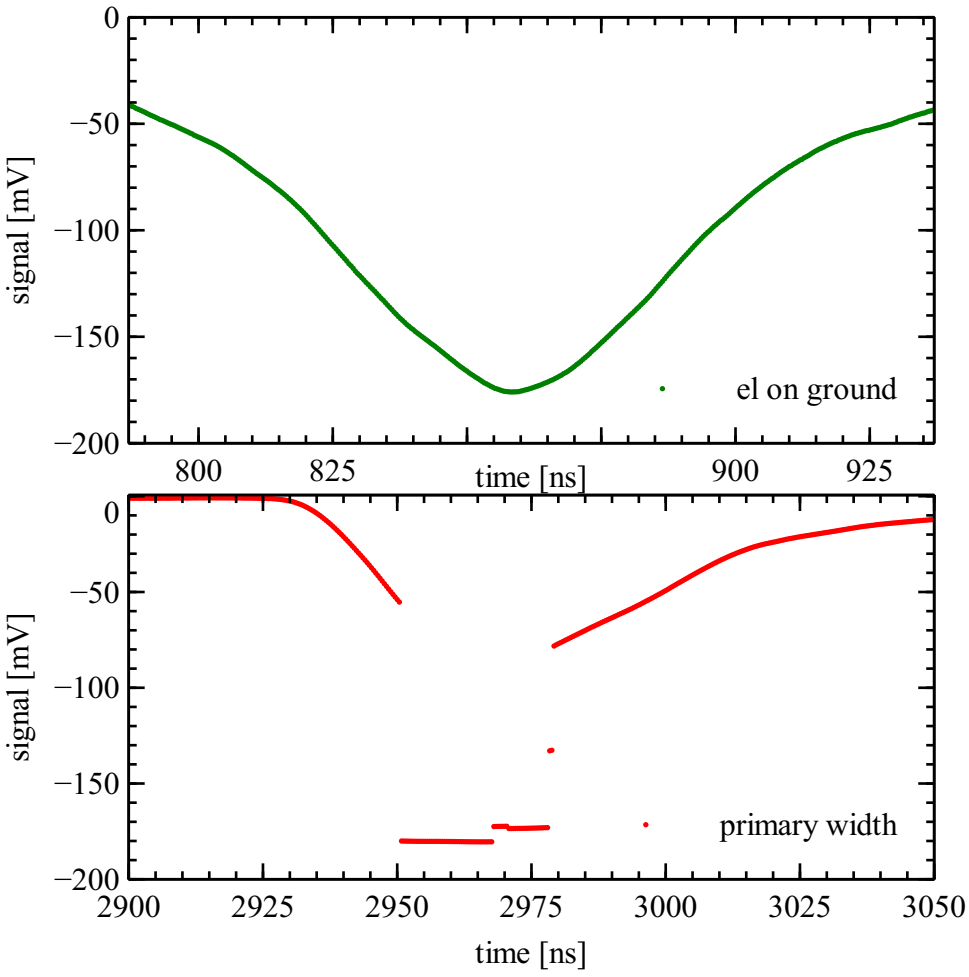

Figure 75: Corrupted data due to wrong oscilloscope settings

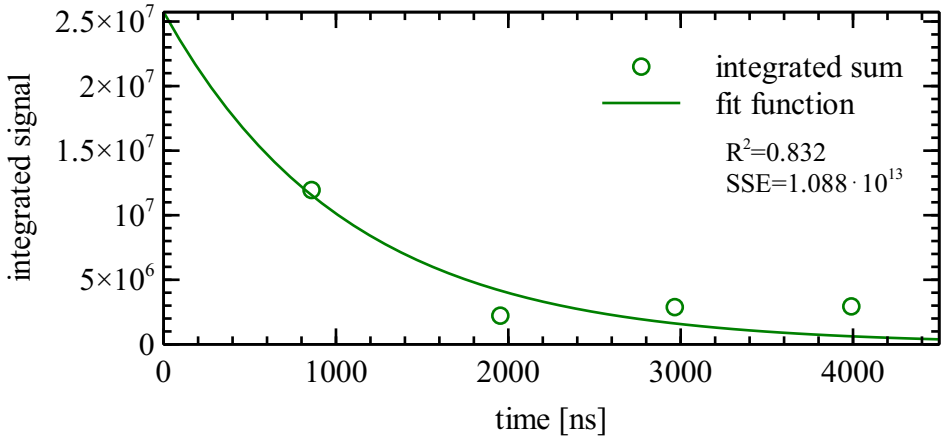

Figure 76: Corrupted data due to wrong oscilloscope settings

7 Conclusion & Outlook

Concluding it can be said a miniaturized positron trap was successfully designed, manufactured, and tested, being able to store positrons for 3 µs using proof-of-concept equipment. These results showed no degradation, however, longer trapping measurements could not be conducted due to technical limitations of the hardware.

This is a great success and is enabling further research into extending storage times in future projects. Trapping positrons using permanent magnets have not been performed in the past. Adding to that, the developed technology of foil electrodes proved to be a viable option for future projects.

The transportable aspect of the trap could not be successfully tested and proven. This was due to multiple reasons, for one the weight restrictions of 4 kg as well as the 4U CubeSat form factor. Other than that, the cost of developing a valve that would comply with these was not within the given budget.

Further due to the pandemic, there could not be enough time spent in the workshop to fabricate tools to build a crimping tool able to seal off the system. Therefore the focus was set on the trap itself and analyze the mobile trap and vacuum sealing in a follow-up experiment at a later time.

Looking ahead, the project has great potential for continuation. Firstly, a first prototype will be flying with EULER at the European Rocket Competition (EuRoC) in Portugal in October 2020.
Shifting the focus from flight to the laboratory there are a couple of well-defined steps that can be taken in the next time. First, an in-depth characterization of the trap should be performed with additional measurement runs. These would enable the calculation of trapping efficiency as well as the trapping losses over an extended period of time.
To determine the trapping efficiency, no additional infrastructure or components would be needed. If the positrons then shall be stored for a longer period of time, dedicated electronics and a monitoring system would need to be designed and manufactured.
In parallel investigations into the crimping as well as alternative valves, options could be evaluated, in order to remove the trap from the experiment and maintain the vacuum over an extended period of time.
Further, it would be interesting if possibilities for real-time monitoring in a mobile trap could be developed in order to precisely register annihilation during handling of a mobile trap.

Acknowledgements

I want to thank first my parents, Maritta and Wolfgang, my brother Pius and my girlfriend Patricia for their support all these years to never give up and always follow my dreams.

I want to thank the Group Rubbia at IPA for enabling this thesis.

I want to highlight here my supervisors, Paolo Crivelli, for continuously asking critical questions and giving feedback and suggestions to improve the work. The other person I want to highlight is Lars Gerchow, who always had an ear for my concerns, discussing possible solutions and motivated me to continue solving problems.

Further, I want to thank Michael Heiss, Gianluca Janka, and Johannes Wütrich for their patience while explaining me paths around dead ends, especially with electronics and laboratory equipment.

Further, I thank Carlos Vigo for his advice during the thesis, always shifting my perspective on challenges to overcome them.

I also want to thank Adamo Gendotti, Damian Sonderegger, Bruno Zehr, and Patrick Gomez for their support and feedback on all aspects of the design and manufacturing of components for the experiment.

I also thank Emilio, Henry, Lucas, Nikola, Jesse, and Philipp for all the times we spent, discussing problems and sudoku-solving during breaks.

I also want to thank ARIS for all the opportunities they provided me in the past years. Especially I want to express my gratitude to Oliver Kirchhoff, who acted on his need to establish a platform for students to apply their knowledge and as well as Manuel Gerold, Felix Dannert and David Häusermann, whom have and will continue shaping me as a person as well as my work on all levels.

Also, I thank Sven Kiefer for setting the foundation of this thesis by establishing contact with the group as well as Richard Boell and Michael Kerschbaum for their support and feedback on my design. I also want to thank Simone Gervasoni for helping me with magnetic measurements and all his feedback on my design and processes and Shelly Arreguin for her help setting up the thesis.

A Appendix A

220-M12 feedthroughs

M12 connectors are frequently used for industrial automation and sensor applications. The type is standardized by DIN EN 61076-101

Allectra offers UHV-compatible M12 feedthroughs and connectors. For less demanding applications, HV and standard connectors can be used on both sides.

Complete Set: UHV connector, feedthrough on CF16 flange and air side connector

Specifications

Feedthrough	**Value**
Number of Pins	4
Voltage rating	250V
Test Voltage	500V DC (Pin to Ground)
Max current	3A
Vacuum	UHV (10^{-10} mbar and below)
Temp.	-200° … +230°C
UHV connector	**Value**
Materials	SS, PEEK, Alu, Gold plated CuBe Pins
Cable connection	Crimp, max. ø 1.0mm (solder possible)
Temp.	-200° … +230°C
Dimensions	15.5mm ø, 16mm long
HV connector	**Value**
Materials	Ni plated Zinc diecast, PA
Cable connection	Screw, max. 0.75mm²
Temp.	-25° … +85°C
Vacuum range	~10^{-6} mbar
Dimensions	20mm ø, 58mm long

M12 feedthrough, seen from the vacuum side, with connectors. The UHV connector has a reduced OD, so it fits through a DN16 flange

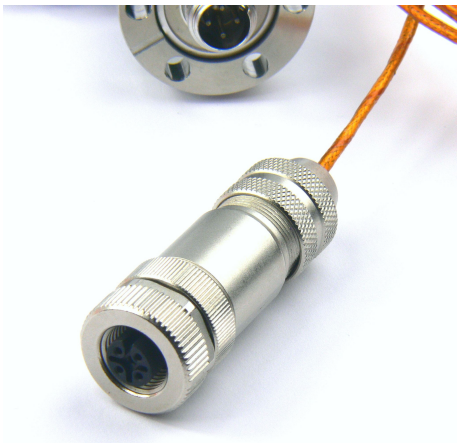

Connector for High Vacuum use, down to 10^{-6} mbar

Additional notes:

For air side use, Allectra offers Quick Disconnect cables, which need only a 90° turn of the nut to be secured.

Allectra recommends the shielded double twisted pair wire 311-KAPM-060-PAIR2 to be used with this feedthrough. Types up to 1mm ø can also be used.

File: 220-M12-E-ukv Last revised 2017-06-29
All data given in this sheet is carefully checked but subject to change at any time.

allectra GmbH, Traubeneichenstr. 62-66, D-16567 Schönfliess, Tel: +49-(0)33056-41598-0 Fax -5, e-mail: info@allectra.com
allectra Ltd, Bluebell Business Estate, Sheffield Park, TN22 3HQ UK T:+44-1825 721 900, F: +44-1825 721 909 uk@allectra.com
allectra Ltd France, 32 rue Principale, F-56500 La Chapelle Neuve, T: +33-297-272307, F: +33-297-72307, fr@allectra.com
allectra Ltd Italy, Via delle Grotte, 482, IT-00067 Morlupo (Roma) T: +39 339 7080563, F: +39 06 9070873, It@allectra.com

TC4467/TC4468/TC4469

Logic-Input CMOS Quad Drivers

Features

- High Peak Output Current: 1.2 A
- Wide Operating Range:
  - 4.5 V to 18 V
- Symmetrical Rise/Fall Times: 25 nsec
- Short, Equal Delay Times: 75 nsec
- Latch-proof. Will Withstand 500 mA Inductive Kickback
- 3 Input Logic Choices:
  - AND / NAND / AND + Inv
- ESD Protection on All Pins: 2 kV

Applications

- General Purpose CMOS Logic Buffer
- Driving All Four MOSFETs in an H-Bridge
- Direct Small Motor Driver
- Relay or Peripheral Drivers
- CCD Driver
- Pin-Switching Network Driver

Package Types

14-Pin PDIP/CERDIP

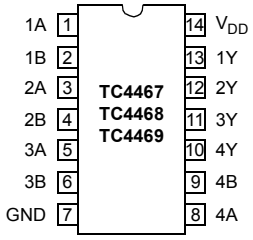

16-Pin SOIC (Wide)

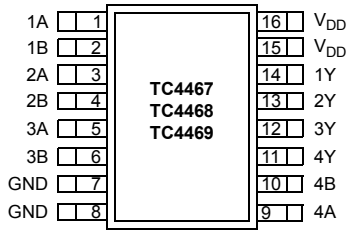

General Description

The TC4467/TC4468/TC4469 devices are a family of four-output CMOS buffers/MOSFET drivers with 1.2 A peak drive capability. Unlike other MOSFET drivers, these devices have two inputs for each output. The inputs are configured as logic gates: NAND (TC4467), AND (TC4468) and AND/INV (TC4469).

The TC4467/TC4468/TC4469 drivers can continuously source up to 250 mA into ground referenced loads. These devices are ideal for direct driving low current motors or driving MOSFETs in a H-bridge configuration for higher current motor drive (see Section 5.0 for details). Having the logic gates onboard the driver can help to reduce component count in many designs.

The TC4467/TC4468/TC4469 devices are very robust and highly latch-up resistant. They can tolerate up to 5 V of noise spiking on the ground line and can handle up to 0.5 A of reverse current on the driver outputs.

The TC4467/4468/4469 devices are available in commercial, industrial and military temperature ranges.

© 2002 Microchip Technology Inc.

Please refer in correspondence: HKCM-Drawing number 9963-56965

QR-CODE

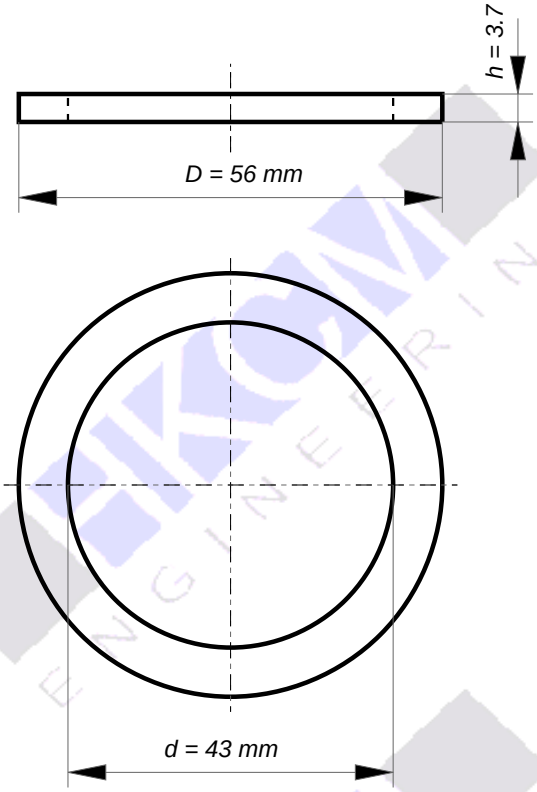

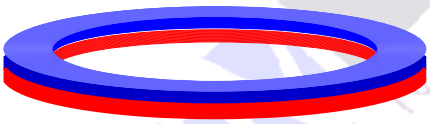

Magnet-Ring R56x43x03.7Zn-33H

Tolerances : DIN ISO 2768-1m (Website Download Center)
ROHs (2011/65/EU) & REACh (2007/EU)
Outer diameter(D) = 56 mm
Inner diameter(d) = 43 mm
Height(H) = 3.7 mm
Material/grade: NdFeB / 33H / 263kJ/m3
Coating: Zinc
Poles: ax
max.operation temperature = 120°C
Flux density inside the magnet = 1.13 Tesla
Temperature coefficient and flux = 0.11% per 1°K
Dead weight: 27.906 g
Holding force on iron 93.78 Newton
Weight, which the magnet can lift: 9.56 kg

HKCM Engineering e.K.
Ottestr.20
D-24340 Eckernfoerde
p: +49 (0) 4351 726 461
f: +49 (0) 4351 726 463
e: sales@hkcm.de
w: https://www.hkcm.de
VAT-Id No.: DE 814 756 521

HKCM® Registered Trade Mark of HKCM Engineering e.K.

Copyright by HKCM Engineering e.K., Instant Update - Copy 11 December 2019 10:50:56

All calculations, diagrams and drawings are computed automatically and should not be used as the sole source of design data. The factors of your application may change these values considerably. All details are subject to alterations at any time.

Please refer in correspondence: HKCM-Drawing number 9963-5924

QR-CODE

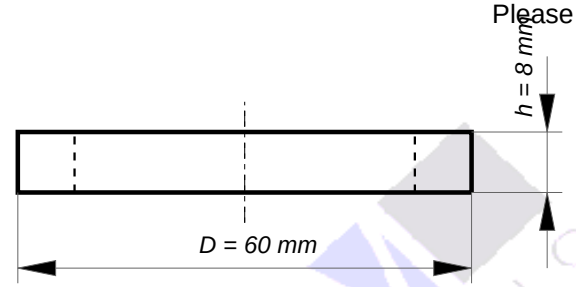

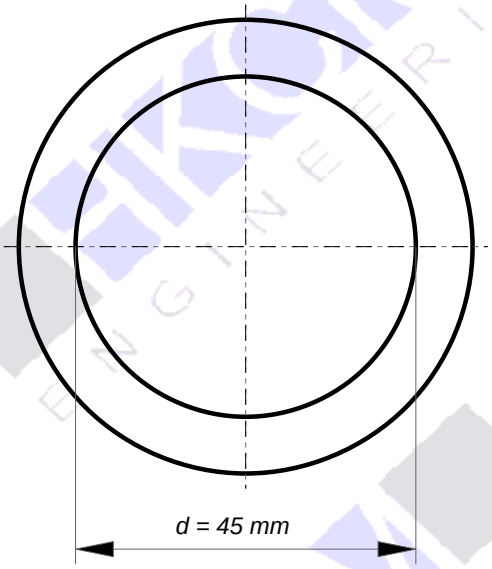

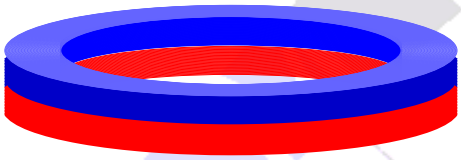

Magnet-Ring R60x45x08Zn-N35

Tolerances : DIN ISO 2768-1m (Website Download Center)
ROHs (2011/65/EU) & REACh (2007/EU)
Outer diameter(D) = 60 mm
Inner diameter(d) = 45 mm
Height(H) = 8 mm
Material/grade: NdFeB / N35
Coating: Zinc
Poles: ax
max.operation temperature = 80°C
Flux density inside the magnet = 1.17 Tesla
Temperature coefficient and flux = 0.11% per 1°K
Dead weight: 73.839 g
Holding force on iron 265.85 Newton
Weight, which the magnet can lift: 27.1 kg

HKCM Engineering e.K.
Ottestr.20
D-24340 Eckernfoerde
p: +49 (0) 4351 726 461
f: +49 (0) 4351 726 463
e: sales@hkcm.de
w: https://www.hkcm.de
VAT-Id No.: DE 814 756 521

HKCM® Registered Trade Mark of HKCM Engineering e.K.

Copyright by HKCM Engineering e.K., Instant Update - Copy 11 December 2019 10:48:08

All calculations, diagrams and drawings are computed automatically and should not be used as the sole source of design data. The factors of your application may change these values considerably. All details are subject to alterations at any time.

Please refer in correspondence: HKCM-Drawing number 9963-62759

QR-CODE

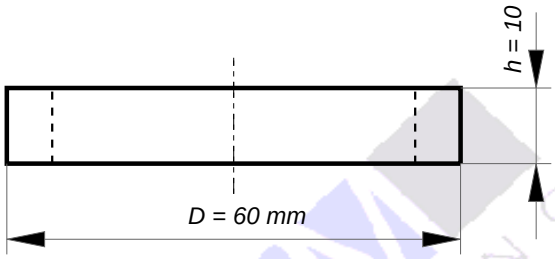

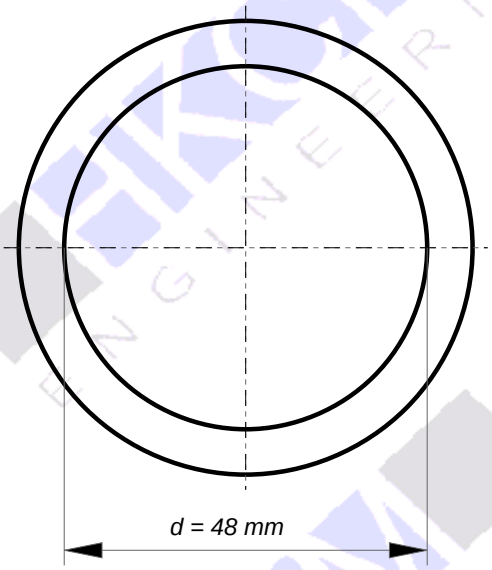

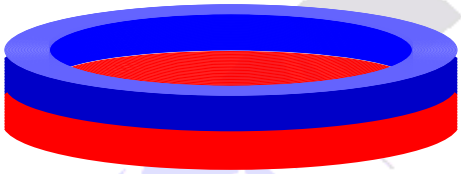

Magnet-Ring R60x48x10Ni-48H ax

Tolerances : DIN ISO 2768-1m (Website Download Center)
ROHs (2011/65/EU) & REACh (2007/EU)
Outer diameter(D) = 60 mm
Inner diameter(d) = 48 mm
Height(H) = 10 mm
Material/grade: NdFeB / 48H / 382kJ/m3
Coating: Nickel
Poles: ax
max.operation temperature = 120°C
Flux density inside the magnet = 1.37 Tesla
Temperature coefficient and flux = 0.11% per 1°K
Dead weight: 75.949 g
Holding force on iron 239.46 Newton
Weight, which the magnet can lift: 24.41 kg

HKCM Engineering e.K.
Ottestr.20
D-24340 Eckernfoerde
p: +49 (0) 4351 726 461
f: +49 (0) 4351 726 463
e: sales@hkcm.de
w: https://www.hkcm.de
VAT-Id No.: DE 814 756 521

HKCM® Registered Trade Mark of HKCM Engineering e.K.

Copyright by HKCM Engineering e.K., Instant Update - Copy 11 December 2019 09:18:51

All calculations, diagrams and drawings are computed automatically and should not be used as the sole source of design data. The factors of your application may change these values considerably. All details are subject to alterations at any time.

Please refer in correspondence: HKCM-Drawing number 9963-5927

QR-CODE

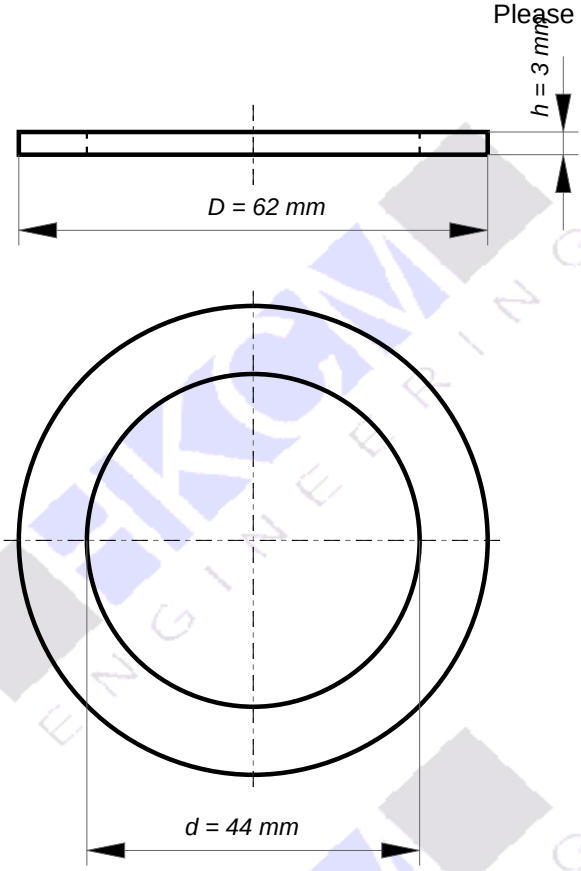

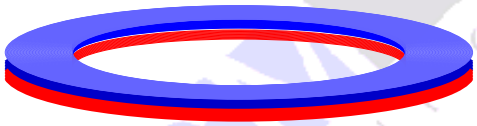

Magnet-Ring R62x44x03Ni-N35

Tolerances : DIN ISO 2768-1m (Website Download Center)
ROHs (2011/65/EU) & REACh (2007/EU)
Outer diameter(D) = 62 mm
Inner diameter(d) = 44 mm
Height(H) = 3 mm
Material/grade: NdFeB / N35
Coating: Nickel
Poles: ax
max.operation temperature = 80°C
Flux density inside the magnet = 1.17 Tesla
Temperature coefficient and flux = 0.11% per 1°K
Dead weight: 33.544 g
Holding force on iron 90.25 Newton
Weight, which the magnet can lift: 9.2 kg

HKCM Engineering e.K.
Ottestr.20
D-24340 Eckernfoerde
p: +49 (0) 4351 726 461
f: +49 (0) 4351 726 463
e: sales@hkcm.de
w: https://www.hkcm.de
VAT-Id No.: DE 814 756 521

HKCM® Registered Trade Mark of HKCM Engineering e.K.

Copyright by HKCM Engineering e.K., Instant Update - Copy 11 December 2019 10:49:06

All calculations, diagrams and drawings are computed automatically and should not be used as the sole source of design data. The factors of your application may change these values considerably. All details are subject to alterations at any time.

M4:1

Bitte bei Korrespondenz angeben: HKCM-Zeichnungsnummer 9962-54040

QR-CODE

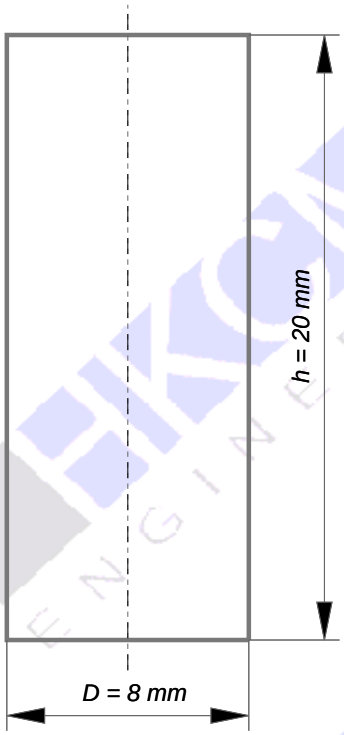

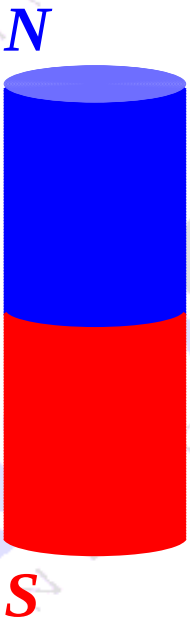

Magnet-Zylinder Z08x20Zn-35H

Toleranzen : DIN ISO 2768-1m (Website Download Center)
ROHs (2011/65/EU) & REACh (2007/EU)
Außendurchmesser(D) = 8 mm
Höhe(H) = 20 mm
Material, Güte: NdFeB / 35H / 279kJ/m3
Beschichtung: verzinkt
Pole: ax
max.Einsatztemperatur = 120°C
Flussdichte im Magneten = 1.17 Tesla
Temperatur Koeffizient der Flussdichte = 0.11% per 1°K
Eigengewicht: 7.501 g
Haltekraft auf Eisen 37.28 Newton
Gewicht, welches der Magnet anheben kann: 3.8 kg

HKCM Engineering e.K.
Ottestr.20
D-24340 Eckernfoerde
p: +49 (0) 4351 726 461
f: +49 (0) 4351 726 463
e: sales@hkcm.de
w: https://www.hkcm.de
VAT-Id No.: DE 814 756 521

HKCM® Registered Trade Mark of HKCM Engineering e.K.

Copyright by HKCM Engineering e.K., Instant Update - Copy 07 January 2020 14:03:09

All calculations, diagrams and drawings are computed automatically and should not be used as the sole source of design data. The factors of your application may change these values considerably. All details are subject to alterations at any time.

STYCAST® 1266 A/B

Two Component, Low Viscosity, Epoxy Encapsulant

Key Feature:	Benefit:
• Optical clarity	• Facilitates visual inspection of protected components
• Low viscosity	• Excellent wicking and flow around parts in tight clearance applications
• High impact strength	• Enhance long term durability of assembly

Product Description:

STYCAST 1266 A/B is a clear, low viscosity, room temperature curable, epoxy encapsulant and impregnant. It has good moisture resistance, good electrical properties, and good impact strength. STYCAST 1266 A/B adheres well to metals, glass, and plastics.

Applications:

STYCAST 1266 A./B is designed to readily impregnate windings, to bond lenses and sheets of glass for good visibility, or for display embedments.

Instructions For Use:

Thoroughly read the information concerning health and safety contained in this bulletin before using. Observe all precautionary statements that appear on the product label and/or contained in individual Material Safety Data Sheets (MSDS).

To ensure the long term performance of the potted or encapsulated electrical / electronic assembly, complete cleaning of components and substrates should be performed to remove contamination such as dust, moisture, salt, and oils which can cause electrical failure, poor adhesion or corrosion in an embedded part.

Accurately weigh resin and hardener into a clean container in the recommended ratio. Weighing apparatus having an accuracy in proportion to the amounts being weighed should be used.

Blend components by hand, using a kneading motion, for 2-3 minutes. Scrape the bottom and sides of the mixing container frequently to produce a uniform mixture. If possible, power mix for an additional 2-3 minutes. Avoid high mixing speeds which could entrap excessive amounts of air or cause overheating of the mixture resulting in reduced working life.

To ensure a void-free embedment, vacuum deairing should be used to remove any entrapped air introduced during the mixing operation. Vacuum deair mixture at 1-5 mm mercury. The foam will rise several times the liquid height and then subside. Continue vacuum deairing until most of the bubbling has ceased. This usually requires 3-10 minutes.

Pour mixture into cavity or mold. Gentle warming of the mold or assembly reduces the viscosity. This improves the flow of the material into the unit having intricate shapes or tightly packed coils or components. Further vacuum deairing in the mold may be required for critical applications.

Properties of Material As Supplied:

Property	Test Method	Unit	Value - Part A	Value - Part B
Chemical Type			Epoxy	Amine
Appearance	Visual		Clear, amber liquid	Clear, yellow liquid
Density	ASTM-D-792	g/cm^3	1.16	1.00
Brookfield Viscosity	ASTM-D-2393	Pa.s cP	8.5 8,500	0.035 35

Properties of Material As Mixed:

Property	Test Method	Unit	Value
Mix Ratio - Amount of Part B per 100 parts of Part A		By Weight By Volume	28 33
Working Life (100 g @ 25°C)	ERF 13-70	minutes	30
Density	ASTM-D-792	g/cm^3	1.12
Brookfield Viscosity	ASTM-D-2393	Pa.s cP	0.65 650

"Our service engineers are available to help purchasers obtain best results from our products, and recommendations are based on tests and information believed to be reliable. However, we have no control over the conditions under which our products are transported to, stored, handled, or used by purchasers and, in any event, all recommendations and sales are made on condition that we will not be held liable for any damages resulting from their use. No representative of ours has any authority to waive or change this provision. We also expect purchasers to use our products in accordance with the guiding principles of the Chemical Manufacturers Association's Responsible Care® program."

PROPERTIES AND TECHNICAL NOTES

SPI Supplies
206 Garfield Avenue,
West Chester, PA 19380, USA

SPI Supplies NO-VOC Silver Conductive Paint

SPI Supplies NO-VOC Silver Paint is a highly conductive, 100% water-based silver paint is designed for making high-performance electrical contacts. This material is VOC free. NO-VOC Silver Paint is optimized for brushing/dipping applications. Primary applications for this material include SEM ground coatings, printed circuit board repair, electroforming, and EMI shielding. Excellent for use on plastic, wood, and ceramic substrates. Because it contains no VOCs, it does not have to be shipped as a hazardous paint.

NO-VOC Silver Paint should perform much like our standard Silver Conductive Paint. It is specially formulated to resist settling of the silver solids. However, it is still suggested that the product is stirred, jar rolled, or shaken well prior to use. If the paint begins to thicken, deionized water may be added to replace water loss or to make slight adjustments for ease of application. Ultrasonic agitation is suggested to ensure that the paint is thoroughly mixed after adding deionized water.

COMPOSITION PROPERTIES:

Silver Content:	40.0% +/- 2
Volume Resistivity:	0.00012 ohms-cm
Sheet Resistivity:	0.05 ohms/sq/mil
Viscosity:	8-15 Kcps (Brookfield RVT, Spin #7, 20 rpm, 25 °C)
Density (typical):	1.29 g/cc
Silver Particle Size:	<20 microns
Cure Schedule:	1-2 hours @ 25 °C or 5-10 minutes @ 60-90 °C
Operating Range:	-55 °C to 140 °C
VOC:	0.0gm/l
Thinner:	Deionized Water
Application Temp:	65 °F (18 °C) to 78 °F (26°C)
Shelf Life:	Indefinite in a sealed container (See Note)

NOTE: Water may evaporate from the product while on the shelf and may be reconstituted using DI water.

Paint Film Removal:
Dimethyl Acetamide is suggested as a solvent for removing NO-VOC films.

11/19 eer

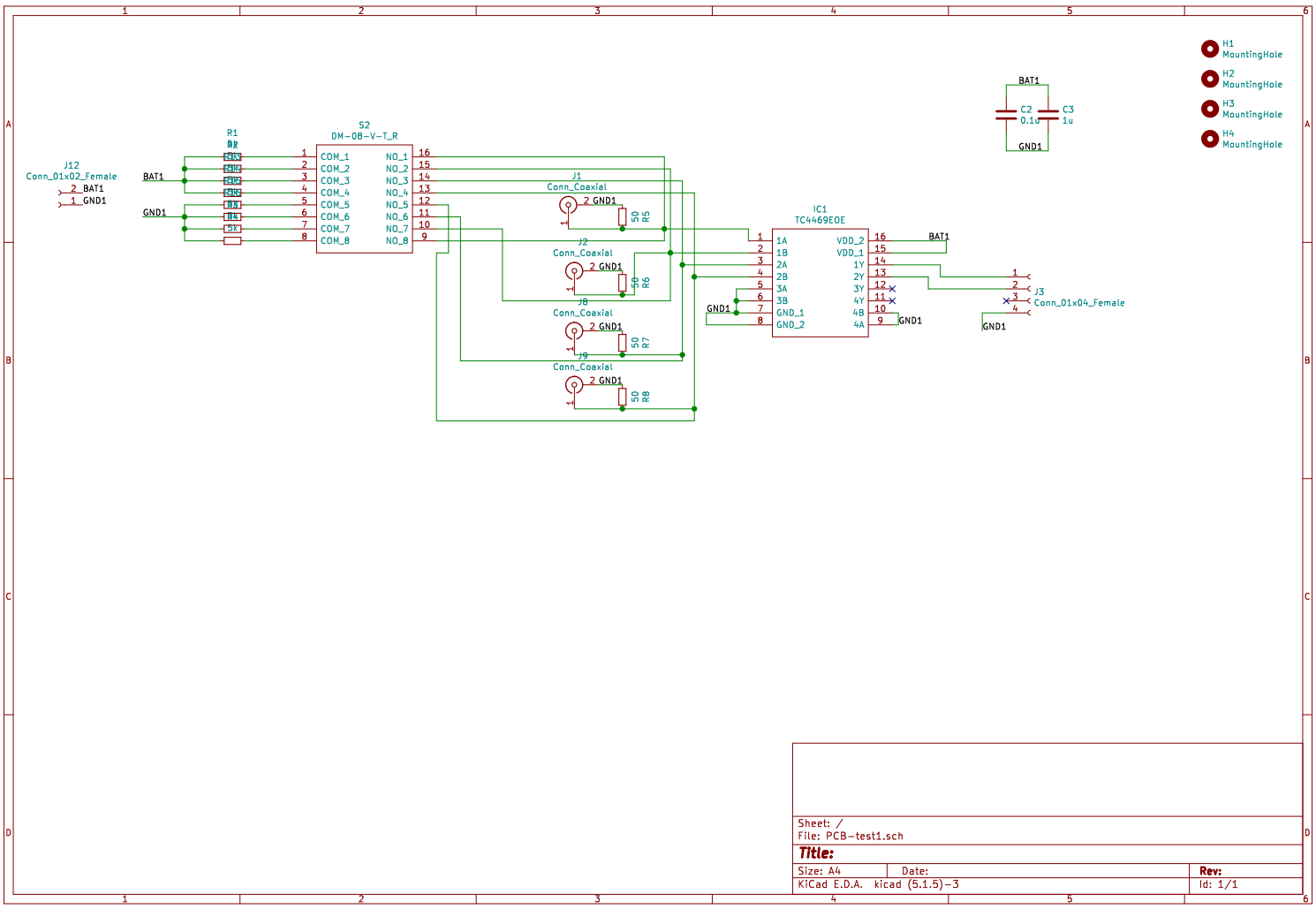

Sheet: / File: PCB-test1.sch		
Title:		
Size: A4	Date:	**Rev:**
KiCad E.D.A. kicad (5.1.5)-3		Id: 1/1

ETH

Eidgenössische Technische Hochschule Zürich
Swiss Federal Institute of Technology Zurich

Declaration of originality

The signed declaration of originality is a component of every semester paper, Bachelor's thesis, Master's thesis and any other degree paper undertaken during the course of studies, including the respective electronic versions.

Lecturers may also require a declaration of originality for other written papers compiled for their courses.

I hereby confirm that I am the sole author of the written work here enclosed and that I have compiled it in my own words. Parts excepted are corrections of form and content by the supervisor.

Title of work (in block letters):

Development of a mobile positron trap for future space applications

Authored by (in block letters):

For papers written by groups the names of all authors are required.

Name(s):	**First name(s):**
Prantl	Paul

With my signature I confirm that

- I have committed none of the forms of plagiarism described in the 'Citation etiquette' information sheet.
- I have documented all methods, data and processes truthfully.
- I have not manipulated any data.
- I have mentioned all persons who were significant facilitators of the work.

I am aware that the work may be screened electronically for plagiarism.

Place, date	**Signature(s)**
Zürich, 20.08.2020	

For papers written by groups the names of all authors are required. Their signatures collectively guarantee the entire content of the written paper.